Numerical Modeling of the Performance of a Paraffin Hybrid Rocket Motor
(Versão corrigida após defesa)

Tiago Ascenção Costa Morão

Dissertação para obtenção do Grau de Mestre em
Engenharia Aeronáutica
(Mestrado Integrado)

Orientador: Prof. Doutor Francisco Miguel Ribeiro Proença Brójo

novembro de 2021

Dedicated to my family

Acknowledgement

First and foremost, my appreciation is addressed to my supervisor, Professor Francisco Brójo for his valuable scientific advice, discussions and suggestions that made this work possible. Providing me everything that was needed to perform this study, starting with lending your personal computer and cluster, in which most of the simulations were performed. I am forever grateful for the kind patience and encouragement which you always demonstrated, being key factors to making this small project.

My special gratitude to my mother Noémia Morão, my father Alberto Morão, my sister Inês Morão, grandmother Licínia Molina and grandfather António Molina for their encouragement and support. Without them, nothing of this would be possible.

And last but not least, I wish to thank all of my friends, especially Mariana Lousada and Miguel Moreira a.k.a Baleia whom are truly a huge part of my life. I am very grateful for their friendship, support, unforgettable and unique moments.

Resumo

Neste trabalho foram realizadas várias simulações em CFD de um foguete híbrido com combustível de parafina e para o oxidante óxido nitroso. Foi realizado um estudo da taxa de regressão do combustivel sólido durante a combustão, com o intuito de compreender a influência no desempenho do motor. A malha é criada utilizando o ANSYS ICEM Meshing e o software comercial ANSYS Fluent 20.2 é utilizado para realizar o estudo numérico. Para realizar este trabalho, um modelo numérico *unsteady* é escolhido com uma malha dinâmica para simular o processo de regressão da superfície do combustível sólido. O modelo viscoso utilizado é o Reynolds Stress model (RSM). Todas as entradas de ar são definidos como entradas de caudal mássico, e a saída é definida como uma saída de pressão. Nesta tese não será feita uma simulação com várias fases, todos os elementos químicos são considerados como estando em estado gasoso. Em primeiro lugar, será realizada uma análise com a injecção com *swirl* onde os pontos de desempenho serão comparados com os resultados experimentais. Depois, é estudada uma nova configuração de injecção (injecção axial) para analisar a melhoria do desempenho que pode trazer ao motor do foguete híbrido. Os resultados finais mostram uma concordância razoável com os valores experimentais, sendo uma das maiores realizações a visualização do fluxo dentro da câmara o que permite compreender o escoamento dentro do motor e que por sua vez leva a compreender os pontos onde se pode melhorar a nível do design do mesmo. Globalmente, pode concluir-se que esta simulação CFD pode ajudar o projectista durante o desenvolvimento de um novo motor de foguetão híbrido.

Palavras-chave

Foguete Híbrido, Propulsão por Foguete, Simulação Numérica, Malha Dinâmica, Taxa de regressão, Transiente, Parafina, Óxido Nitroso, Fluent, ICEM Meshing, Desempenho, Emissões

Abstract

In this work were performed several CFD simulations of a hybrid rocket with paraffin fuel and nitrous oxide was oxidizer. A study of the regression rate of solid grain during combustion is performed to understand the influence on the performance of the motor. The numerical mesh is created using ANSYS ICEM Meshing and the commercial software ANSYS Fluent 20.2 is used to perform the numerical study. For making this, an unsteady numerical model is established with a dynamic mesh to simulate the regression process of the solid fuel surface. The viscous model used is the Reynolds Reynolds Stress model (RSM). All of the air-inlets are defined as mass-flow inlets, and the exit is defined as a pressure-outlet. In this thesis no multi-phase flow simulation will be done, all the chemical elements are considered to be in a gaseous state. First, it will be performed analyse with the swirl injection where the performance points will be compared with the experimental results. Then, a new injection configuration (axial injection) is studied to analyse the performance improvement that can bring to the hybrid rocket engine. The final results show reasonable agreement with the experimental values, with one of the biggest achievements was to visualize the flow inside the chamber and understand what is happening and where the design can be improved. Overall, it can be concluded that this CFD simulation can help the designer during the development of a new hybrid rocket motor.

Keywords

Hybrid Rocket, Rocket Propulsion, Numerical Simulation, Dynamic mesh, Transient, Regression Rate, Paraffin wax, Nitrous Oxide, Fluent, ICEM Meshing, Performance, Emissions

x

Contents

List of Figures

List of Tables

List of Acronyms

AMROC	American Rocket Company
ASCII	American Standard Code for Information Interchange
CAD	Computer Aided Design
CATIA	Computer-Aided Three dimensional Interactive Application
CEA	Chemical Equilibrium with Applications
CFD	Computational Fluid Dynamics
CPU	Central Processing Unit
DARE	Delft Aerospace Rocket Engineering
DES	Detached Eddy Simulation
DNS	Direct Numerical Simulation
DV	Delivered Velocity
ESA	European Space Agency
EVM	Eddy Viscosity/diffusivity
FSM	Fractional Step Method
FSRFL	Fuel Stream Rich Flammability limit
GIRD	Group for the Study of Reaction Propulsion
GOX	Gaseous Oxygen
GUI	Graphical User Interface
HDPE	High Density-polyethelene
HHV	Higher Heating Value
HPRE	Hybrid Propellant Rocket Engine
HRP	Hybrid Rocket Propulsion
HTPB	Hydroxy-Terminated Polybutadiene
LES	Large eddy simulation
LHV	Lower Heating Value
LOX	Liquid Oxygen
LPRE	Liquid Propellant Rocket Engine
LRE	Liquid Rocket Engines
MEOP	Maximum Expected Operating Pressure
MV	Main Valve
ONERA	Office National d'Etudes et de Recherches Aérospatiales
PISO	Pressure Implicit with Splitting of Operators
Presto!	PREssure STaggering Option
RAM	Random Access Memory
RANS	Reynolds-averaged Navier–Stokes
RNG	Renormalization-group
RSM	Reynolds stress models
SIMPLE	Semi-Implicit Method for Pressure Linked Equations

List of Symbols

v	Velocity	$[m/s]$	A_t	throat area of nozzle at combustion chamber	$[m^2]$
c_p	Specific heat at constant pressure	$[J/kg.K]$	c_v	Specific heat at constant volume	$[J/kg.K]$
D	Diameter	$[m]$	F	Thrust force	$[N]$
g_0	Gravitational acceleration	$[m/s^2]$	h	Specific enthalpy	$[J/kg]$
$\overline{h}$	Convection heat transfer coefficient	$[W/m2.K]$	I_{sp}	Specific impulse	$[s]$
k	Thermal conductivity	$[W/m.K]$	L	Length	$[m]$
M	Molar mass	$[Kg/mol]$	Ma	Mach number	$[-]$
$\dot{m}$	Mass flow rate	$[kg/s]$	OF	Oxidizer-to-fuel ratio	$[-]$
Pr	Prandtl number	$[-]$	P	Pressure	$[Pa]$
R	Universal gas constant	$[J/kmol.K]$	$\dot{r}$	Regression rate	$[Pa]$
T	Temperature	$[K]$	U	Velocity	$[m/s]$
u	Specific internal energy	$[J/kg]$	V	Volume	$[m^3]$
C_μ	$k-\varepsilon$ model constant	$[-]$	u	Velocity	$[m/s]$
C^*	Characteristic velocity	$[m/s]$	L_g	length of fuel grain	$[m]$
d_p	Port diameter	$[m]$	$d_p(i)$	Port diameter at the ith time step	$[m]$
C_F	Thrust coefficient	$[-]$			

Greek letters

γ_p	specific heat ratio of burnt product	$[-]$	ε	Eddy viscosity	$[m^2/s]$
μ	Absolute viscosity	$[Pa.s]$	μ_T	Turbulent viscosity	$[Pa.s]$
ρ	Density	$[kg/m^3]$	ϕ	Equivalence ratio	$[-]$
Δt	time step	$[s]$			

Chapter 1

Introduction

1.1   Motivation

Hybrid rocket propulsion, although not a new concept, has been gathering more attention in recent years. A hybrid rocket is an intermediate between a solid motor and a liquid engine. This arrangement has an intermediate set of benefits and drawbacks, compared to solid and liquid propulsion. Compared to solid motors the main advantages of hybrids are the likelihood of throttling and re-start and enhanced safety and reliability. Compared to liquid motors, the main advantages are the overall lower cost, potentially better density specific impulse and engine mass fraction. The HPRE has a great development potential, which may turn it even more appellative for future space missions and other applications. Hybrid rocket motors store the oxidizer as a liquid and the fuel as a solid, a configuration that is mechanically simple and reduces the opportunity for a chemical explosion, both in flight and during ground operations. That makes hybrids safer than solid-fueled rockets. Hybrids are also more flexible because the flow of the oxidizer can be controlled, meaning that the thrust can be adjusted or even shut down and restarted during flight.

1.2   Main Goals

The main goal of this dissertation is to study the performance of a hybrid rocket engine. For this purpose, an unsteady numerical model with the regression rate of the solid grain is established. Dynamic mesh is employed to simulate the regression process of the solid fuel surface. Based on this model, numerical simulations on a N_2O/Paraffin hybrid motor have been performed. First, it will be performed an analyse with the swirl injection where the performance points will be compared with the experimental results. Then, a new injection configuration (axial injection) is studied to analyse the performance improvement that can bring to the hybrid rocket engine.

1.3   Thesis Structure

This thesis is divided into six chapters.

In the current chapter, the author expresses his motivation behind the development of this thesis. The objectives proposed for this thesis are also presented. An Historical review is presented in order to understand the problems and concerns that appeared throughout the

time. Finally, a bibliographic review is presented, focusing on other works related to the subject and pointing out their importance in this area. This chapter was written with the intent that any person with minimal scientific knowledge could understand what is proposed for this work.

In the second chapter introduces the principals behind a HRE. A close-up on the main requirements, types and configurations are then presented along with some combustion fundamentals.

In the third chapter it will be introduced the experimental-related activities that are been used for performing the numerical analyses in this thesis.

In the fourth chapter presents the CFD simulation process, which is composed of several processes. Before starting the process of numerical simulation is necessary a whole set of steps: geometry, generation of the mesh and the numerical simulation. In this chapter the combustion model used is described.

In the fifth chapter are presented the results and discussion, as well as explained what is expected and what is new.

The sixth chapter is the last chapter and presents the main conclusions of this thesis research and some thoughts for future work, respectively.

1.4   Historical Review

The hybrid rocket concept has been around for more than eighty years. The first liquid propellant rocket launched by the Soviet Union was actually a hybrid that used liquid oxygen and gelled gasoline. The first flight of the 2.5 m long rocket occurred in 1933. The motor produced about 500 N of thrust for 15 s, reaching an altitude of about 1500 m. As far as we know this was the first flight of a hybrid rocket. The rocket was designed by Tikhonravov (figure 1.1), with one of his designs, and built by a team from the Group for the Study of Reaction Motors (GIRD) that was headed by the legendary Korolev, who later would design the first Sputnik launchers. [1]

Figure 1.1: GIRD-09 rocket (on the left). [2]

Early hybrid rocket development and flight test programs were initiated both in Europe and the U.S. in the 1960's. The European programs in France and Sweden involved small sounding rockets, whereas the American flight programs were target drones (Sandpiper, HAST, and Firebolt) which required supersonic flight in the upper atmosphere for up to 5 minutes. These latter applications were suitable for the conventional hybrid because its very low burning rate was ideal for a long duration sustained operation. [3]

The reason why regression rates are paramount is that they're a direct measure of the total mass flow and thus thrust. A low regression rate implies that a much larger burn surface would be required to attain the same mass flow, thus reducing the potential benefits of using hybrid rocket technology. [4]

Despite the very low regression rate of the fuel, in the late 1960's Chemical Systems Division of United Technologies (CSD/UTC) investigated motor designs of larger diameters that could produce high thrust suitable for space launch vehicles. They experimented with a 38-inch diameter motor delivering 40,000 lbs of thrust. In order to achieve a high mass flow rate, a motor with 12 ports in the fuel grain was required. Although the motor was successfully fired several times, it was recognized that the poor volumetric fuel loading efficiency would result in a deficit in vehicle performance. [3]

Interest in the hybrid was revived again in the late 1970's when concern was expressed for the storage and handling of the large solid propellant segments of the Shuttle booster. The storage of potentially explosive grains is costly in terms of requirements for reinforced structures and interline distance separation. The same safety concern arose again after the Space Shuttle Challenger disaster, where it was recognized that a thrust termination option might have avoided the failure. [3]

This concern was heightened when, a few months later, there was a Titan failure, caused by an explosion of one of the solid boosters. Several hybrid propulsion programs were initiated in the late 80's and early 90's. The Joint Government/Industry Research and Development (JIRAD) program involved the testing of 11 and 24-inch diameter hybrid motors at the Marshall Space Flight Center. Another hybrid program initiated during the early 90s was DARPA's Hybrid Technology Options Project (HyTOP). The goal of this program was to develop the HyFlyer launch vehicle and demonstrate the feasibility of hybrid boosters for space applications. The members of the HyTOP team were AMROC, Martin Marietta and CSD/UTC. [3]

In the 1990s, two significant hybrid efforts occurred. One was the formation of the American Rocket Company (AMROC), an entrepreneurial industrial company devoted entirely to the development of large hybrid boosters. The second, with encouragement from NASA, was the formation of the Hybrid Propulsion Industry Action Group (HPIAG) composed of both system and propulsion companies devoted to exploring the possible use of hybrids for the Shuttle booster and other launch booster applications. Both efforts ran into technical stumbling

blocks, basically caused by the low regression rate fuels, which resulted in large diameter motors with many ports to satisfy thrust requirements. The resulting configuration not only compromised potential retrofit for the Shuttle and Titan boosters but also raised questions about the internal ballistic performance of a thin web multi-port motor, especially toward the end of burning when the web approaches structural failure. Although AMROC had many successful tests in 51-inch diameter motors, they ran into difficulties when the motor was scaled to 6-foot diameter and $250,000$ pounds of thrust. [3]

The low regression rate of the fuel dictated a 15 port grain design and problems of poor grain integrity were the results. In 1995 AMROC filed for bankruptcy. The Hybrid Propulsion Demonstration Program (HPDP) began in March 1995. The goal of the HPDP was to enhance and demonstrate several critical technologies that are essential for the full-scale development of hybrid rocket boosters for space launch applications. The government and industry participants in the program were NASA, DARPA, Lockheed Martin, CSD/UTC, Thiokol, Rocketdyne, Allied Signal and Environmental Aeroscience Corporation. Even though the tasks of the HPDP program included systems studies and sub-scale testing, the main objective of the program was the design and fabrication of a $250,000$-pound thrust test-bed. The design of the motor was guided by the sub-scale motor tests performed under the JIRAD program. The wagon wheel $7+1$ multi-port fuel grain was made of conventional hydroxyl-terminated-polybutadiene (HTPB)/ Escorez fuel.

The motor was fired for short times in July 1999. The motor exhibited large pressure oscillations and unequal burning rates in the various ports. Later the motor was stabilized by substantially increasing the heat input at the fore-end of the motor. Problems related to the low regression rate inherent in conventional hybrids fuels were not solved. [3]

The most successful flight of a hybrid rocket occurred on Oct. 4, 2004, when Space Ship One (see figure 1.2) reached an altitude of 100 km for the second time in a 1-week period to win the $10 million Ansari X-prize. The spacecraft used a four-port HTPB fueled motor and nitrous oxide oxidizer. Although the flight of Space Ship One was a great success, it was not exactly a walk in the park for the pilot. The description in figure 1.2 reveals a pretty sobering picture of the flight. The conclusion from this history is that if a significantly higher burning rate fuel can be developed for the hybrid motor, the multi-port difficulties just described can be alleviated and a smaller, safer more efficient motor can be designed. Although this deficiency of conventional hybrid fuels was recognized more than forty years ago, attempts to increase the burning rate by more than $50-100\%$, without compromising the safety and low-cost features of the hybrid design, have been largely unsuccessful until recently. [3]

Figure 1.2: Space Ship One hybrid motor operation as described in Aviation Week.

The figure text reads:

Neither SpaceDev or eAc met Scaled's wishes. The SpaceDev design, which has four longitudinal ports in the rubber fuel for enough burning area for high thrust, comes on with a bang, producing maximum thrust at the start—not the smooth ramp-up envisioned to turn the corner. The peak thrust is only about 85% of the desired plateau, and declines steadily from there, according to the Sept. 18 SETP presentation. Despite the early start, this still means that to get enough total impulse to loft SpaceShipOne above 100 km., the motor has to run longer than desired, in the very thin atmosphere where control is tenuous.

The webs of rubber between the four SpaceDev ports thin out and come apart toward the end of the run. The chunks extrude through the nozzle, causing frightening shaking and explosion noises in the cockpit. It happened at least three times on one flight and Melvill thought the tail had blown off. After minutes by himself in zero-g and entry, he was relieved when chase aircraft said the spaceship appeared alright.

The eAc motor didn't ignite until five sec. after the switch was thrown, and then also came on with a bang, but the initial combustion instabilities were less. It has a single port and compensates for the lower burning area with fuel additives to increase burning rate. But not enough, because it only made about 65% of the desired thrust. That required the burn time to be even longer for sufficient total impulse, extending the engine run farther out of the atmosphere.

Longer burn time of the eAc motor was considered the more serious problem, and the contract went to SpaceDev.

Mike Dornheim - Aviation Week
October 18, 2004 page 36

Other developments were made by Lockheed in 2000s and finally Scaled Composites and SpaceDev developed the N_2O/HTPB hybrid rocket for the sub-orbital vehicle SpaceShipOne whose successor is today operating for Virgin Galactic as part of its suborbital flight program [5, 6]. Table 1.1 contains a summary of some existing Hybrid Rockets with their respective properties. In the table, one can find general reference data for some real-life rocket engines. This helps us get a much better grasp on the orders of magnitude involved for each of the values. Particularly the values for the inert mass fraction of the engines. The inert mass fraction is one of the main concerns when looking at the disadvantages of hybrid rocket solutions. It is accepted that in general there will be a higher inert mass fraction, when compared to solid rockets, due to the presence of feed system components and all the accompanying parts. Whereas solid rocket engines have inert mass fractions on the order of less than 0.1 (see the database in [7]), meaning a propellant mass fraction higher than 0.9. In table 1.1, this is represented in the row "Mass Fraction" corresponding to the propellant mass fraction. There we see only one value greater than 0.9 which is the ESA 3 kN engine. This optimistic value is because this case is purely a theoretical design. The other cases for which data is available to have, on average, 0.82 as their propellant mass fractions. [4]

1.5 Bibliographic Review

In the last decade, we have observed an increase in hybrid rocket propulsion engines (HRPE) projects. This is due to HRPE having a safe and reliable combustion process. Also, it has small costs of development and comparatively cleaner environmental characteristics. Moreover, designers see in the small specific impulse (related with low regression rate) and the combustion efficiency, two points to develop even more.

5

Table 1.1: Examples of developed Hybrid Rockets with their respective properties. Data from [8–10]. The value accompanied by "?" indicates that the source data might be unreliable and that the value may correspond to the vacuum specific impulse and not the sea-level one.

Motor designation	H-30	H-500	H-1500	H-1800	3kN	HY-157	0.1 kN	Chiron	0.5 kN
Company	AM-ROC	AMROC	AMROC	AMROC	ESA	DLR	TU-Delft/TNO	USAFA	UoS
Average vacuum thrust [kN]	14.1	400.3 / 315 (sl)	758.4	1143.1	3	5224 (sl)	0.088 (sl)	4.5	0.5
Total vacuum impulse [kNs]				82292.1					
Effective vacuum specific impulse[s]	287.3		295.2	278	295	298.2 (sl) ??	184.6 (sl)		310
Total mass [kg]	641		31200	36970	6994	188000		15 kg	
Propellant mass[kg]	497		24890	31980	6710	157200	0.794		
Mass fraction [-]	0.78		0.8	0.87	0.96	0.84			
Burn time [s]	100	70	95	72	7000		16.4	15	18.5
Diameter [m]	0.61	1.29	1.83	1.85	1	5.2		0.21	0.1
Stage length		15.55		19.5				3.62	
Combustor length[m]	0.71		8.79		2.6	23.5			0.36
Length of casing(w/o nozzle) [m]				9.80					
Stage length to diameter ratio [-]		12.05		10.52				17.24	
Propellant	HTPB-N20	HTPB-LOX	HTPB-LOX	HTPB-LOX	PE-NTO	PE-LOX	PE-GOX	HTPB-LOX	PE-HTP
Mass mixture ratio [-]				1.7	3.6		4.83		
Grain configuration		11-spoke	15-spoke (triangular port shape)	15-port + cylindrical port	Single port (cylindrical)	12 port (cylindrical)	Single port (cylindrical)	3 port (pie-shaped)	Single port (cylindrical)
Liquid feeding	Vapor pressure	He pressure	Pump	He Pressurant	Pressurant	Pump	Pessurant	He pressurant	N2 pressurant
Tank material		Steel / carbon fibre	Aluminum		Titanium	Aluminum	Steel	0.003 mm aluminium	
Casing material	Graphite-epoxy	Graphite-epoxy	Graphite-epoxy	Kevlar	Steel		302 steel	316 steel	
Thermal insulation			Kevlar		EPDM				
Nozzle materia	Carbon-phenolic	Silicon-phenolic / glass-phenolic	Silicon-phenolic / glass-phenolic	Silicon-phenolic	Carbon-carbon			Graphite / silicon-carbide	
MEOP [bar]					31.5				
Average pressure[bar]	31		34.5	24.9	10	48	9.1	18	18.1
Expansion ratio	75.1	40	17.7	9	215.8			3.34	3.34

Chang et al. [11] highlight exactly that HPRE recover their attention not only because of the safety issues in the combustion process and the small development costs but also because of its low specific impulse, which represents areas of opportunities for research and development.

Santos et al. [12] conducted experimental investigations in hybrid rockets based on paraffin fuel and GOx and N_2O oxidizer, with 200 N thrust. The results showed better behaviour of the paraffin against polyethylene.

Almeida and Santos [13] designed, built and launched two-hybrid rockets prototypes based on paraffin and nitrous oxide. It is believed to be the first paraffin hybrid rockets launches in Latin America.

A hybrid rocket slab motor visualisation test stand was developed by Theba R. et al. [14] to investigate the behaviour of regression rates on pure and 40% aluminised paraffin wax fuel grains. The results determined suggest that Sasolwax 0907 is a high regression fuel that burns about three times faster than traditional fuel compositions.

Pal Y. et. al [15] performed mechanical tests that showed significant improvement in compression strength and elastic modulus with the addition of PE and Al to pure paraffin wax. The heat of combustion of paraffin-based fuel samples increased as the Al loading content was increased from 5 wt % to 25 wt %. The theological investigation indicated that the addition of PE to paraffin had increased the melt layer viscosity, whereas the effect of Al powder on viscosity was small.

Gomes S. et. al [16] conducted an Experimental Study of Polyurethane-Based Fuels with the Addition of Paraffin and Aluminum for Hybrid Rocket Motors and concluded that the embedding of paraffin increased the overall ballistic parameters of the motor. The use of the binder is essential to structure and strengthen the paraffin to endure flight condition loads. Mixing ratios of 30% w/w of paraffin wax in the binder structure yielded good results, particularly when swirl injectors are used.

A numerical approachable to compute the internal ballistics of paraffin-based hybrid rocket engines has been developed and validated by Migliorino M. et. al [17]. Results show the dominating role of thermal radiation (up to 62% of the total heat flux) as the product of average port radius and average chamber pressure increases. For smaller port radius, for which radiation is less important, the model is still capable of fairly predicting the correct amount of paraffin melted and injected in the combustion chamber, hence giving confidence to the obtained fluid-dynamic solution. The numerical approach provides the capability of internal ballistics prediction and paves the way to novel design-oriented investigations for paraffin-based hybrid rockets.

Karabeyoglu et al. [18, 19] developed a melt layer hybrid combustion theory to predict re-

gression rates in fuels that exhibit fuel entrainment and were able to successfully predict the regression rates of the cryogenic hybrid fuels and paraffin wax. Karabeyoglu et al. [20] later refined the theory to include supercritical operation and predict the regression rates of the entire series of homologous normal alkanes (C_nH_{2n+2}) with a reasonable degree of success. The expanded theory indicated that paraffin waxes are the best candidates for solid fuels in hybrid rocket engines among the series of n-alkanes.

Karabeyoglu and Akron [21] claim the benefits of paraffin fuels, in comparison to traditional polymeric fuels, include: 1) low cost and high availability; 2) high performance including specific impulse, regression rate, and fuel utilization; 3) non-toxicity; 4) virtually infinite shelf-life; and 5) hydrophobic nature which allows for sensitive, high energy additive incorporation. The commonly cited drawbacks of utilizing paraffin-based fuel include 1) potentially lower combustion efficiencies due to ejection of entrained but unburned fuel droplets and 2) poor mechanical properties that make scale-up difficult. Numerous mechanical property enhancement strategies have been employed, and one common method is the inclusion of polymer additives. [22, 23]

The preceding section served to review and compare all relevant literature pertaining to paraffin fuel for hybrid rocket applications. In general, the inclusion of paraffin in an HTPB fuel leads to increased mass loss during the early stages of decomposition, which is more prevalent with further paraffin loading. Several research teams have evaluated the combustion of HTPB/paraffin fuel blends on lab-scale hybrid rockets and under various operating parameters. While some researchers report significant enhancement, others have reported little to no enhancement associated with paraffin inclusion. Discrepancies between both thermal degradation and hybrid rocket combustion studies indicate that a paraffin inclusion limit for noticeable enhancement may exist, highlight the importance of paraffin inclusion methodology (molten liquid versus solid particle).

Chapter 2

Hybrid Rocket Propulsion

The hybrid rocket (figure 2.1) is essentially safer than other rocket designs. The idea is to store the oxidizer as a liquid and the fuel as a solid, producing a design that's less prone to chemical explosion than conventional solid and bi-propellant liquid designs. The fuel is contained within the rocket combustion chamber in the form of a cylinder with a circular channel called a port hollowed out along its axis. Upon ignition, a diffusion flame forms over the fuel surface along the length of the port. The combustion is sustained by heat transfer from the flame to the solid fuel causing continuous fuel vaporization until the oxidizer flow is turned off. In the event of a structural failure, oxidizer and fuel cannot mix intimately resulting in a catastrophic explosion that may endanger personnel or destroy a launchpad. [3]
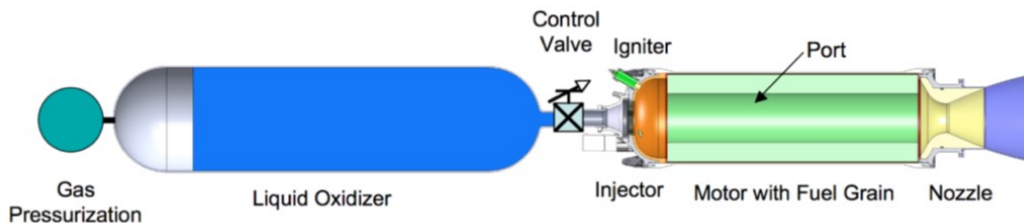
Figure 2.1: Schematic of a hybrid rocket motor. [3]

The hybrid rocket is also classified into various types, as shown in figure 2.2. The standard hybrid motor arrangement consists of a pure fuel grain cast and cured in the combustion chamber (as a solid rocket motor) and of a liquid oxidizer stored in a separate tank and injected under pressure in the combustion chamber. The solid-state can also be obtained either by freezing a fuel grain such as ethylene and n-pentane that has been tested at a laboratory scale or by gelling a liquid fuel sustained by an internal matrix. The inverse-hybrid motor concept uses liquid fuel and an oxidizer grain; it works in the same way as the "standard" one. [24]
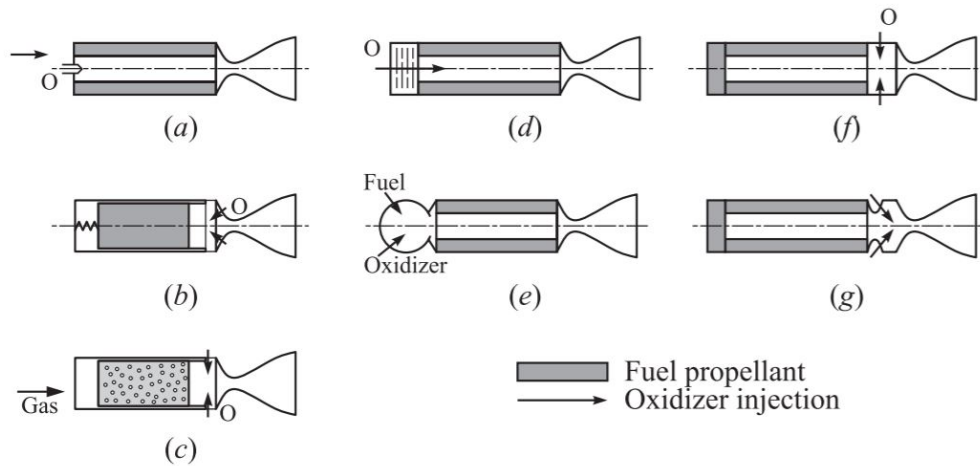
Figure 2.2: Typical hybrid motor concepts [25]: (a) liquid solid reaction: head injection; (b) solid feed; (c) gel feed; (d) gas solid reaction: motopropellant gas generator; (e) bi-propellant gas generator; (f) liquid gas reaction: aft oxidizer injection; and (g) aft Venturi injection

Among all the design concepts mentioned before, the standard hybrid rocket (scheme of figure 2.2 a) is the one that has received the most attention. The inverse-hybrid motor, even being a topic of some studies isn't a solution: industrial manufacturing of an oxidizer solid grain isn't feasible with current technologies.

The main motivation of the hybrid rocket is the non-explosive character of the fuel, which led to safety in both operation and manufacture. The fuel could be fabricated at any conventional commercial site and even at the launch complex with no danger of explosion. Thus, a large cost saving could be realized both in manufacture and launch operation.

The hybrid rocket requires one rather than two liquid containment and delivery systems. The complexity is further reduced by the omission of a regenerative cooling system for both the chamber and nozzle. Throttling control in a hybrid is simpler because it alleviates the necessity to match the momentum of the dual propellant streams during the mixing process. Throttle ratios up to 10 have been common in hybrid motors. The fact that the fuel is in the solid phase makes it very easy to feature performance-enhancing materials to the fuel like aluminium powder. In principle, this might enable the hybrid to gain an I_{sp} advantage over a comparable hydrocarbon fueled liquid system. [3]

Boundary layer combustion is the primary mechanism of hot gas generation in hybrid rockets. The idealized sketch in figure 2.3 illustrates the flow configuration. The hybrid normally uses a liquid oxidizer that burns with a solid fuel although reverse hybrids such as liquid hydrogen-burning with solid oxygen have been studied. The flame thickness and location in the boundary layer are shown roughly to scale. The flame zone is relatively deep in the boundary layer and the flame tends to be fuel-rich based on the observed flame position and relatively low flame temperatures measured in the boundary layer. The hybrid enjoys many safety and environmental advantages over conventional systems; however, large hy-
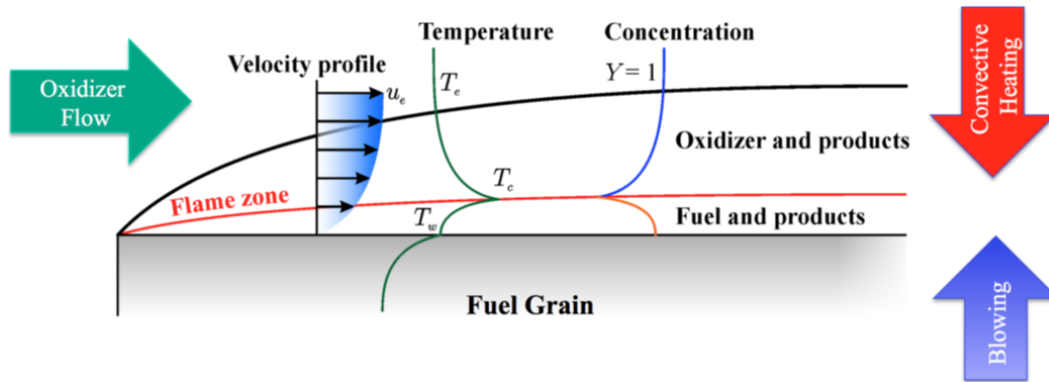
Figure 2.3: Boundary layer combustion. [3]

brids have not been commercially successful. The reason is that traditional systems use polymeric fuels that evaporate too slowly making it difficult to produce the high thrust needed for most applications. [3]

2.1 Comparison to Solid Rockets

While the hybrid rocket concept has been known for over 75 years, it was not given serious attention until the 1960s. The first reason for interest in the hybrid was the nonexplosive nature of the design, which led to safety in both operation and manufacture. The fuel could be fabricated at any conventional commercial site and even at the launch complex with no danger of explosion. Thus, a large cost saving could be realized both in manufacture and launch operation. [1]

Further advantages of the hybrid over the solid rocket are greatly reduced sensitivity to cracks and de-bonds in the propellant, higher specific impulse, throttle-ability to optimize the trajectory during atmospheric launch and orbit injection, and the capacity to thrust terminate/restart on demand. The products of combustion are environmentally harmless compared with conventional solids that generally use perchlorate-based oxidizers. Solid rocket combustion products contain acid-forming gases such as hydrogen chloride. [1]

In addition, there are concerns about the effects of low levels of environmental perchlorate, most of which comes from the propellant and explosive manufacture.

2.2 Comparison to Liquid Bi-propellant Rockets

The main advantages of the hybrid over a liquid bi-propellant system are as follows [1]:

1. The hybrid rocket presents a reduced explosion hazard compared to a liquid because an intimate mixture of oxidizer and fuel is not possible.

2. The hybrid rocket requires one rather than two liquid containment and delivery sys-

tems. The complexity is further reduced by the omission of a regenerative cooling system for both the chamber and nozzle.

3. Throttling control is simpler because it alleviates the requirement to match the momenta of the dual propellant streams during the throttling operation. Throttle ratios up to 10 have been achieved with relative ease in hybrid rocket motors.

4. The theoretical specific impulse of a hybrid rocket is more appropriately compared to a bi-propellant liquid than a solid. This is because the oxidizers are the same and the solid fuels are hydrocarbons with energy content similar to kerosene. However, hybrid solid fuel densities are typical 1520% greater than the density of liquid kerosene. Figure 2.4 depicts the specific impulse of LO_x burning with paraffin and HTPB.

5. The fact that the fuel is in the solid phase makes it very easy to add performance modifying materials such as aluminium powder. The heat of the reaction of aluminium is substantial enough to outweigh the increase in molecular weight of the exhaust products, enabling the hybrid to gain a small increase in I_{sp} depending on the oxidizer. The main benefit of the aluminium addition is a substantial increase in fuel density over a comparable hydrocarbon fueled liquid system. There is also a somewhat subtle effect that occurs with storable oxidizers such as N_2O_4, wherein aluminium addition to the fuel tends to both increase the theoretical I_{sp}, and shift the peak I_{sp} to lower values of the oxidizer to fuel (O/F) ratio. For the same propellant total mass, there is a larger proportion of the more dense solid propellant. This leads to a reduced liquid feed system and tank size, producing better performance.

6. The ability to add energetic materials to the fuel is one of the key advantages of hybrids over bi-propellant liquids. Calabro [26] suggested the addition of aluminium trihydride (AlH_3, called alane) to HTPB in a LO_x hybrid design as a possible replacement for the Ariane 5 boosters. Calculations by Calabro suggest a possible increase in the ideal specific impulse by as much as 25 s compared to a LO_x/HTPB hybrid. Approximately the same level of performance increase would occur with the addition of alane to paraffin fuel. DeLuca et al. [27] provide an excellent discussion of the preparation and handling of the energetic but hazardous alane along with a characterization of its physical properties. They note that the α form of AlH_3 is quite stable at room temperature and therefore may be useful as a propellant additive for both solid and hybrid rockets. They show a significant increase in the regression rate of both HTPB and paraffin at low oxidizer flux probably associated with the ejection of fuel into the port due to hydrogen out gassing. Alane (1.48 g/cm3) also increases fuel density, although not as much as pure aluminium (2.70 g/cm3). There are additional benefits from metal hydrides; Calabro et al. [28] show that adding magnesium hydride to the fuel substantially reduces the concentration of oxidizing species in the nozzle flow, an effect that would reduce nozzle erosion and further improve performance.

2.3 Advantages and Disadvantages of HRP

Hybrid propulsion is not a mature technology for large boosters. This technology requires the cooperation of two different engineering technologies - solid and liquid propulsion that is not used to work together. Due to its characteristics (i.e., separately stored fuel and oxidizer), hybrid propulsion systems may offer important advantages over their liquid and solid competitors.

They are increasingly popular due to the advantages they provide over solid and liquid rockets such as [29]:

1. Safety – propellants are separated by phase and distance, hindering the risk of explosion.

2. Environmental friendliness – the by-products are generally carbon dioxide and water.

3. Throttling – oxidiser flow rate is easily adjustable.

4. Grain robustness – due to the limited reactivity of hybrids they are not dangerous and are not prone to fuel grain cracking.

5. Fuel versatility – various propellant combinations are readily available.

6. Low cost – the overall cost of a hybrid rocket is relatively low as it is less complex compared to liquid rockets and therefore requires less hardware. Fuel grain manufacturing is also cheaper than solid grains due to the safety aspect with regards to its handling, storage and transportation.

According to Sutton [30], Humble et al. [31] and to Jansen and Kletzkine [32], the main disadvantages of a Hybrid Rocket Engine are:

- The mixture ratio and the specific impulse varies during the steady-state operation and throttling;

- Small regression rate, for combustion chambers higher than 30 cm diameter, the fuel grain needs multiple combustion ports, which can be an advantage for long term applications, such as mobile targets and gas generators;

- Efficiency in nominal steady-state combustion is in the range of 93 to 97%, which is slightly lower than liquid and solid systems;

- System density impulse is small, this means that needs more volume than solid propellant systems;

- The mass fraction of the engine is slightly reduced due to some fuel sliver that usually is retained in the combustion chamber at end-of-burn;

- Oxidizer-to-fuel ratio varies with the increase of combustion grain port diameter during burning, which can reduce the HPRE performance, but these losses can be minimized in a good design;

- Heat transfer problems during long operation periods of time;

- Design presents some difficulties due to the lack of experimental data for some propellants combinations.

These features make it a suitable alternative to the conventional systems for various space applications such as sounding rockets, first-stage boosters, upper-stage launch vehicles, orbital injection systems, and suborbital and orbital human space flight involving space tourism. [33]

Nevertheless, there are certain limitations associated with a hybrid propulsion system such as low fuel regression rate and varying mixture ratio (O/F) during combustion. The low regression of polymeric fuels and the subsequent poor combustion efficiency is largely attributed to the diffusion-flame-limited combustion model of a hybrid propulsion system. [34]

Over the years, several improvements were proposed to enhance the hybrid fuel regression rate. These changes included non-conventional grain designs having multi-port geometries [35, 36] and embedded diaphragms [37, 38], and altered oxidiser flow streams using swirl and radial injection techniques [39, 40]. However, these regression enhancement measures led to complexity in design and manufacturing.

Karabeyoglu et al. used long-chained hydrocarbons like paraffin wax, which remain solid at room temperature. The adoption of paraffin wax replaces these fuel grains with simple, single port geometries thus simplifying the rocket motor design.A 34 times enhancement in regression rate was obtained. [41] This high regression rate can be attributed to entrainment contribution to the mass flow rate, reduced effect of blocking due to two-phase flow and enhanced heat transfer due to increased surface roughness. [42] The proposed theory was validated by scale-up tests conducted on larger engines. [43] The mass flow rate due to entrainment is quantified in literature as

$$\dot{m}_{ent} \propto \frac{P_{dyn}^{\alpha} h^{\beta}}{\mu_l^{\gamma} \rho^{\pi}} \quad (2.1)$$

The entrainment exponential terms (α, β, γ and π) in the above correlation play an important

role in mass flow rate. The correlation (2.1) suggests that mass entrainment is dependent on dynamic pressure (P_{dyn}), melt layer thickness (h), viscosity (μ), as well as surface tension (ρ) of the fuel grain and hence, affects the fuel regression rate. However, combustion efficiency and mechanical integrity are decisive attributes of solid hybrid grains for their applicability in the space industry. Pure paraffin wax ($C_{24}H_{50}$, PW) has poor structural integrity and cannot possibly sustain flight inertial loads, thermal load and/or shocks, thrust and radial combustion pressure. Several attempts had been made towards improving the mechanical properties of paraffin-based hybrid fuels using additives. [44–47]

A novel approach towards regression enhancement could be doping solid fuels with energetic micro or nano-sized additives such as metals and light metal hydrides. [48] These additives improve fuel regression behaviour by raising the theoretical flame temperature, besides reducing gasification heat and mitigating the blocking phenomenon. Increased radiative heat transfer to the grain surface results in a reduction in viscosity of melted fuel thereby enhancing entrainment. [49]

2.4 Applying conditions of the HRP

When safety and reliability are of concern, hybrid propulsion systems can be applied. Practically, it possesses all merits of modern Liquid Rocket Engines (LRE or LPRE) and Solid Rocket Motors (SRM or SPRE). Other important aspects are the simplicity and the cost of those systems. Environmental questions are becoming more and more important nowadays. HRP can be a good solution since hybrid engines are using non-toxic propellants.

Other conditions for applying the HRP are:

- The fuel and the oxidizer needs to be in different physical states, i.e., oxidizer vapour/liquid – fuel solid or oxidizer solid – fuel vapour/liquid;

- When requires Start-Stop-Restart capabilities;

- When it is needed throttleable capability.

2.5 The fuel regression rate law

Theory shows that the fuel mass transfer rate is proportional to the mass flux averaged across the port. The mass flow rate increases with axial distance along the port leading to the coupling between the local fuel regression rate and the local mass flux. For proper design, accurate expressions are needed for both the time-dependent oxidizer-to-fuel ratio at the end of the port and the time at which all the fuel is consumed. As the fuel is depleted the flame approaches the motor case at which point the burn must be terminated. The coupling between the local regression rate and the local mass flow rate means that both variables depend on

time and space. This complicates the analysis of the thrust time behaviour of the hybrid compared to a solid rocket. The problem is governed by two coupled first-order partial differential equations, the regression rate equation [3]

$$\frac{\partial r(x,t)}{\partial t} = \frac{a}{x^m} \left(\frac{\dot{m}_{port}}{\pi r^2} \right)^n \quad (2.2)$$

and the mass flow growth equation

$$\frac{\partial \dot{m}_{port}(x,t)}{\partial x} = \rho_f(2\pi r)\frac{a}{x^m} \left(\frac{\dot{m}_{port}}{\pi r^2} \right)^n \quad (2.3)$$

The local mass flux in the port is generally denoted G where

$$G = \frac{\dot{m}_{port}}{\pi r^2} = \frac{\dot{m}_{ox} + \dot{m}_f}{\pi r^2} \quad (2.4)$$

The local port mass flow rate, $\dot{m}_{port}$, is the sum of the oxidizer mass flow rate, $\dot{m}_{ox}$, injected at the entrance to the port and the accumulated fuel mass flow rate, $\dot{m}_f$, transferred from the fuel grain upstream of a location x. The coefficient a is an empirical constant determined by the choice of fuel and oxidizer. The units of the regression rate constant are

$$[a] = \frac{Length^{2n+m+1}}{Mass^n Time^{1-n}} \quad (2.5)$$

The dependence of regression rate on mass flux G and stream-wise coordinate x arises from the dependence of the skin friction and heat transfer rate on Reynolds number based on distance along with the port. Values of the exponents suggested by theory are $m = 0.2$ and $n = 0.8$. Measured values of n tend to be in the range 0.3 to 0.8 depending on the choice of fuel and oxidizer. Values of n greater than 0.8 or less than about 0.3 are generally not observed. The length exponent turns out to be very difficult to measure since it is relatively small and would require a large number of motor tests at a wide range of scales to be determined accurately. As nearly as one can tell at this point m is considerably smaller than the prediction of classical theory.

A widely used approximation to (2.2) and (2.3) is the single equation

$$\frac{dr}{dt} = a_0 G_{0x}^m \quad (2.6)$$

where the port length effect is neglected and the fuel regression rate is assumed to only depend on the oxidizer mass flux, which is constant along with the port. In general, equation (2.6) underestimates the fuel mass generation rate. However, (2.6) can be a reasonably accurate approximation in situations where the design O/F ratio is relatively large, more than 5 or so.

A greater problem is that the vast majority of values of the regression rate constant reported in the literature correspond to a_o based on data measured against (2.6). The problem with this is that every change in the value of O/F for a given test motor requires the determination of a new value of a_o. In point of fact, the O/F generally varies during the course of a burn and so the reported value of a_o also depends on how the mean O/F is determined. Consider

$$\frac{\partial r(x,t)}{\partial t} = \frac{a}{x^m}\left(\frac{\dot{m}_{port}}{\pi r^2}\right)^n =$$
$$\frac{a}{x^m}\left(\frac{\dot{m}_{ox}(1+1/(\dot{m}_{ox}/\dot{m}_f(x,t)))}{\pi r^2}\right)^n = \frac{a(1+1/(OF(x,t)))^n}{x^m}\left(\frac{\dot{m}_{ox}}{\pi r^2}\right)^n \quad (2.7)$$

If the basic regression rate equations (2.3) and (2.4) are to be believed then

$$a_0 = a(1+1/(OF(x,t)))^n \quad (2.8)$$

In principle a_o is a function of space and time. It can only be treated as a constant if some scheme of space-time averaging of the O/F ratio is used for a given run and, even then, a_o will have a new value every time the O/F is changed. Unfortunately, when a_o is reported in the literature, the corresponding O/F is often not reported. A consequence is that today we often do not have good, solid empirical values of the regression rate constants for many propellant combinations.

In marked contrast to solid rockets, the regression rate of a hybrid is insensitive to the chamber pressure except at very low fluxes where radiation effects become important and at very high fluxes where chemical kinetics effects are important. This important characteristic enables the chamber pressure to be a free variable in the motor design enabling the designer to optimize the chamber pressure for a given mission. Although the hybrid seems to lie somewhere between a liquid and a solid system it has advantages that are unique and not enjoyed by liquids or solids.

2.6 Specific impulse

The theoretical specific impulse of a hybrid rocket is more appropriately compared to a bi-propellant liquid than a solid. The oxidizer can be any of the oxidizers used with liquid bi-propellant engines. Typically, the solid fuel is a polymeric hydrocarbon such as hydroxyl-terminated-poly-butadiene (HTPB), a common solid propellant binder with an energy density comparable to kerosene. But, hybrid solid fuel mass densities are typical $15-20\%$ greater than the density of liquid kerosene. Figure 2.4 (left) depicts the theoretical specific impulse versus oxidizer to fuel the O/F ratio of liquid oxygen (LO_x) burning with paraffin and HTPB. A plot of LO_x burning with liquid kerosene would look very similar. [3]
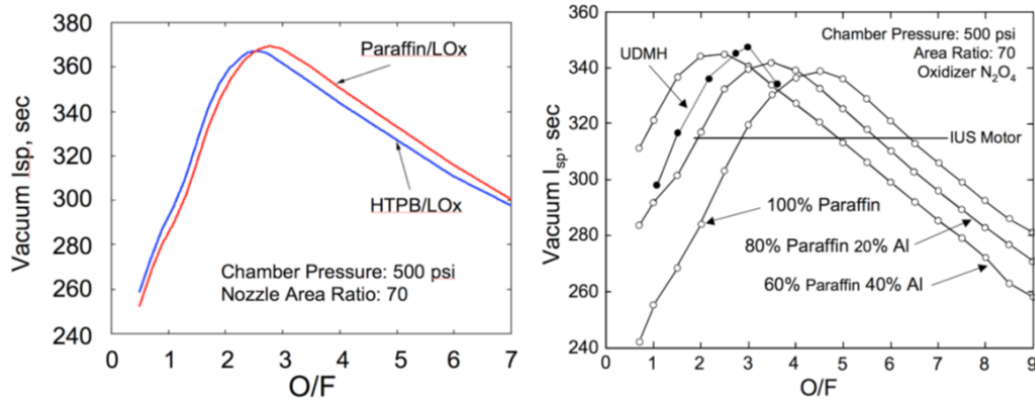
Figure 2.4: Left figure, the ideal specific impulse for paraffin and HTPB burning with LO_x. Right figure paraffin-aluminium mixtures burning with nitrogen tetroxide. The IUS (Inertial Upper Stage) motor was a solid rocket built by the Chemical Systems Division of United Technologies and used as an upper stage in Boeing satellite launches for many years. [3]

The plot on the right of figure 2.4 shows the specific impulse of paraffin burning with N_2O_4 with varying percentages of aluminium added to the fuel by mass. Aluminium addition tends to increase the specific impulse slightly while reducing the optimal O/F allowing the designer to use smaller liquid storage and feed system. These figures give a pretty good illustration of the range of O/F ratios used in typical systems. Generally, the oxidizer mass flow rate tends to be two or more times the fuel mass flow rate at the end of the port. [3]

2.7   Combustion efficiency

Hybrid propellants burn differently from both liquid and solid propellants. For the classical HTPB hybrid propellant, mixing and combustion occur in a diffusion flame zone that is in the same range of length as the inner bore. Several measures could be undertaken (separately or combined) to have a reasonable or even good efficiency level: special grain design; special oxidizer injection techniques; and improved fuel grain formulation. The special grain design aiming at creating and organizing turbulent zones (all along the inner bore) will play a dual role: (i) increasing combustion efficiency; and (ii) lowering the risk of combustion instabilities (medium frequency = acoustic coupling). [24]

A widely proposed solution is to create a premixing chamber and a post-combustion chamber, including or not a secondary injection of oxidizer. Another way could be to have distributed slots [26] or a central cavity. Another solution is to include turbulence generators like metal or plastic screens in the fuel grain so that after regression the obstacles are created all along the inner channel [50] (localized turbulence), or to include crystalline loads increasing surface roughness in the course of gasification (ejected distributed turbulence).

18

2.8 Injection systems

In the early developed hybrid motors in France (Sounding Rocket LEX, SPAL30 for the C30.C Target Drone), ONERA paid particular attention to the injection system to avoid losing room with large premixing and post-combustion chambers. The injection design resulted from extensive experimental work and led to specific impulse efficiencies greater than 0.95 [51]. If taking into account the C_F effects, this means very high efficiency with C^* values in the range of those for liquid propellant (0.99 for the acceleration regime). The basis of this design was to eliminate laminar combustion and have premixed turbulent combustion from the very beginning.

The combustion chamber was divided into two parts, the first one ended with an elastomeric diaphragm. The first chamber injector consisted of 6 tubes/30 vortex injectors (injector A). The diaphragm injector consisted of 108 elementary vortex injectors (injectors B and C). The main grain was a 6-branch star with a MON 40 / NMTD combination (figure 2.5). The measured specific impulse efficiency was 0.95 taking into account C_F losses. This means that it is possible to have C^* combustion efficiencies at the level of liquid propellants. [24]
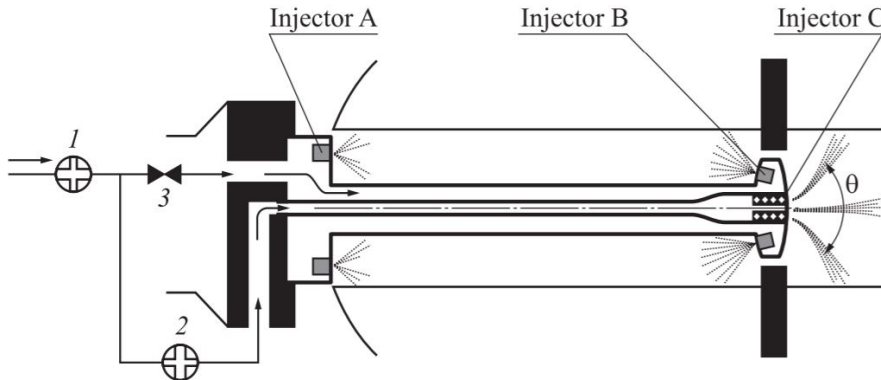
Figure 2.5: SPAL motor injection device: 1 - main valve; 2 - calibrated orifice; and 3 - by-pass valve. [24]

A more classical injector head was used by AMROC with LO_x/HTPB combustion. Also, a classical shower head with or without diverging jets should be mentioned (figure 2.6). The configuration of figure 2.6 a led to stable combustion due to strong re-circulation whereas the configuration of figure 2.6 b was not that stable. This kind of injector is associated with a premixing chamber [30, 48]; nevertheless, it was probably not so simple. Here, the $C^* - efficiency$ could reach 0.98 without combustion instabilities. In conclusion to this point, it is possible playing on several parameters to reach a good efficiency without combustion instabilities, the counterpart being either a more cumbersome motor or a more sophisticated design. [24]
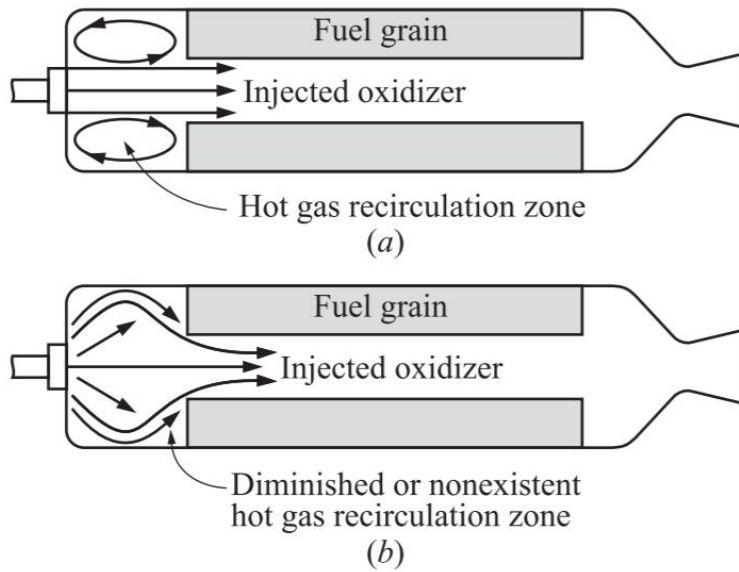
Figure 2.6: Classical shower-head without (a) and with (b) diverging jets. [24]

2.9   Throat material erosion rate

The nozzle of a hybrid motor uses the same technologies as those used for solid motors (Table 2.1). The exhaust gases are very chemically aggressive for throat materials. Therefore, one has to take into account that the same combustion pressure requires a lower average area ratio which results in a lower average specific impulse. [24]

Table 2.1: Comparison of erosivity [50]

Throat materials	Erosivity, mm/s	
	Solid (HTPB)	Classical hybrid
Carbon/phenolc resin	0.252	0.65
Silica/phenolic resin	0.42	1.12
Carbon/carbon	0.13	0.24

Some advanced hybrid propellants (including hydrides) whose exhaust gas composition is close to that of solid propellants, will exhibit much better behaviour and will not show significant differences with the solids. The effluents of typical hybrid propellants (excluding after burning in the exhaust plume) could have very low erosivity: a potential low-cost formulation (LO_x/Wax/MgH_2) will show lower erosivity than a classical solid formulation (Table 2.2) with its large amount of hydrogen and without water and CO_2. [24]

Table 2.2: Combustion gas composition (moles/$100g$) [24]

Composition	$LO_x - CH_4$	Solid	Wax	Wax MgH_2
H	0.161	0.1560	0.035	0.016
H_2	0.398	1.136	0.074	2.955
OH	0.359	0.024	0.278	0.000
H_2O	2.112	0.035	1.255	0.005
O	0.085	0.002	0.076	
O_2	0.178	0.000	0.506	
CO	0.824	0.847	0.455	1.404
CO_2	0.562	0.032	0.961	0.000
N_2		0.288		
AL_2O_3		0.337		
HCl		0.467		
MGO				1.090

2.10 Residuals

Solid propellants have a negligible amount of residuals and liquids of less than 2%. Classical hybrid propellants with a low regression rate associated with wagon wheel geometry (see figure 2.7) will have a much greater level of residuals and the regression of the surface will be not regular. Moreover, stopping the engine upon full fuel consumption will be a hazardous procedure. Mainly for multi-ports, the amount of residuals in hybrid motors is very important. The 1100-kilo-newton AMROC motor (see figures 2.5 and 2.6) had a high level of residuals (> 15%). To obtain a very low and reproducible level of residuals on multiple ports will be a hard point. [24]

On the one hand, the mass of residuals has to be considered as a dead mass penalizing the performance of a hybrid motor. On the other hand, if hybrid propellants with a high regression rate exist, then with a single port geometry, efficient internal insulation and low erosive formulation, the number of residuals may be very low. [24]

2.11 Fabrication, Storage, and Testing

As for handling, virtually, all hybrid fuels are considered inert (exhibit zero TNT equivalency), i.e., they can be transported using normal shipping techniques with no additional safety requirements. This is a meaningful benefit when compared to traditional solid propellants, where any processing is considered a hazardous operation and special handling considerations must be seen. As for fabrication, manufacturing and inert grain is a major parameter influencing the production cost due to a lower safety cost. Classical hybrid motors can be cast in light industrial facilities using the techniques of traditional solid propellant casting. [24]

The level of safety is increased: "In liquid bi-propellant systems, leakage of propellants or structural failures due to mishandling or excess loads, whether on the launch pad or in flight,
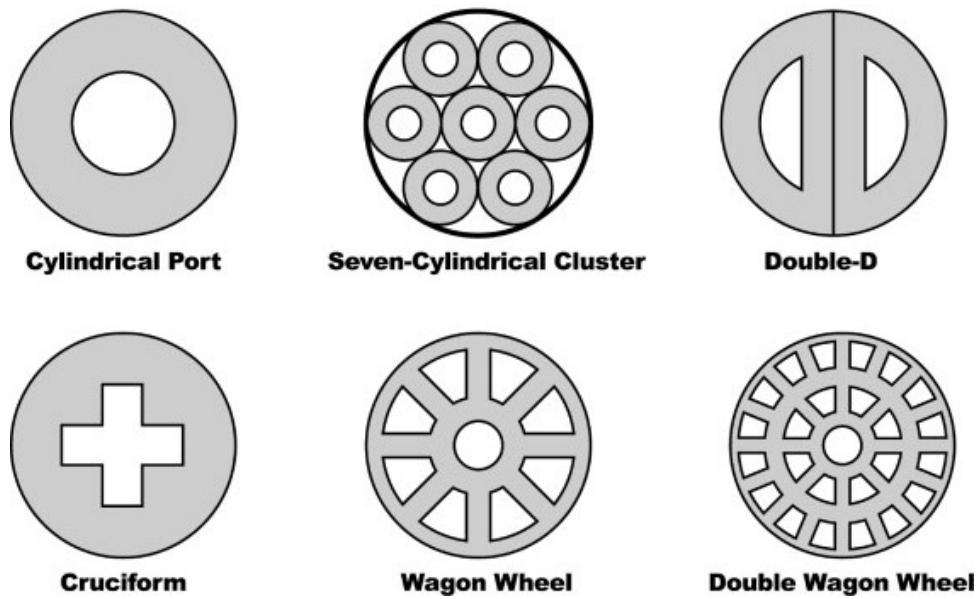
Figure 2.7: Examples of Grain Shapes [52]

could lead to a catastrophic conflagration if the leakage or failure results in a fuel/air fire or mixing of the fuel and oxidizer. On the opposite, there is a much lower chance for any violent energy release hazard involved in the event of leakage or structural failure in the hybrids liquid oxidizer system. These safety features represent the most desirable characteristics of hybrid rockets. Their safety characteristics will clearly have a strong impact for reducing future propulsion hazards to the payload of unmanned missions, launch facilities, and manned flights". [48]

2.12 Operability, Reliability and Cost

Compared to liquid rockets, the relative simplicity of hybrid rockets offers crucial benefits in pre-launch operations due to their fewer components and operational steps. Hybrid rockets are more complex than solid due to the need for an oxidizer delivery system, with an associated oxidizer tank pressurization system and pump if necessary. [24]

Although hybrid motors are more complex than solid, they use only one fluid system, which makes them less complex than bi-liquid systems (liquid propellant rocket engines).

The handling and casting process costs should be significantly lower than those for solid fuels. Since there is only one liquid (oxidizer) used, the system costs should be significantly lower than those for a liquid system. When dealing with advanced hybrid propellants, the use of a toxic or hazardous additive has to be proscribed as being the origin of a cost increase.

2.13 Minimal Environmental Impact + Nontoxicity = "Green" propellant

Rocket launchers are known to have four types of effects on the atmosphere, including stratospheric ozone depletion, acid rain, reduction of local air quality due to dispersion of toxic compounds, and global warming. The effect of solid and liquid propellants on ozone depletion is a very controversial subject. The following major points may be noticed:

- with the current number of flights per year, this effect is entirely negligible [53] in comparison with other human activities and natural sources. From a long-term perspective and regulatory demand to decrease the pollution to a minimum, the classical solution is a good answer vs. storable propellants or solids; and

- advanced hybrid propellants have to comply with these requirements; it means that some additives such as beryllium whose oxide is a highly toxic species will be prohibited.

2.14 Stop-Start Restart Capabilities

This is the most important point that may solve many safety problems. For illustration, in the hybrid project for the Shuttle, this is the only solution to save and recover the astronauts during the boost phase (need to stop the propulsion before astronauts ejection). In a typical launch vehicle, it is the only solution with liquids to be able to respect the safety zones. The stop restart capabilities are mainly required for upper stages and result in launch vehicle optimization in terms of cost and performance. This advantage over the solid motor is also highly recognised when designing small launch vehicles where solid fuels are generally the best answer in terms of cost-efficiency. [24]

2.15 Throttling Capabilities

Several researchers emphasize the flexibility given by the throttling capabilities of hybrid motors. This feature allows tailoring the shutdown and obtaining an accurately delivered velocity increment (DV) and, consequently, an accurate position, as the liquid engines can do (figure 2.8).

OPTIMIZATION PARAMETERS:
F_m, F_m/F_a, T_c via SRB performance;
Thrust law shape, T_c via trajectography
and launcher mass (general loads)

P_{dyn}, ϕ_{th}, β_{max}, In-flight loads

Thrust

F_m

γ_{max}

F_a

CONSTRAINTS:
Maximum values of P_{dyn}, ϕ_{th}, β_{max},
launch-pad safety, stages fallout, etc.

Twin boosters: slope, β_{max}

Stage separation

T_c Time
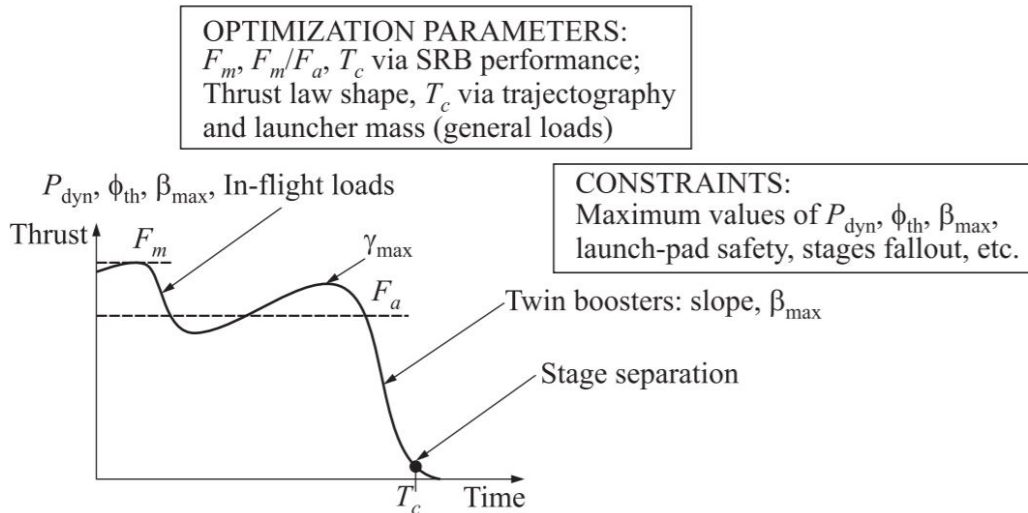
Figure 2.8: Thrust law shape optimization and design criteria [54]

This throttling capability of hybrid propulsion is virtually not a real advantage over solid motors where the thrust can be tailored as required without losses in specific impulse. For a solid motor, the mixture ratio is invariant by nature. For hybrid motors with a constant oxidizer mass flow rate, the thrust will decrease and the mixture ratio increase leading as a counterpart to an average specific impulse loss that will depend on the motor design. [24]

Nevertheless, with long grain and oxidizer flow regulation (to stay at the maximum specific impulse), the thrust law shape is naturally decreasing, which is a better compromise than a liquid engine with constant thrust.

2.16   The problem of low regression rate

The main disadvantage of the hybrid is that the combustion process relies on a relatively slow mechanism of fuel melting, evaporation and diffusive mixing as depicted in figure 2.3. In a solid rocket, the flame is much closer to the fuel surface and the regression rate is typically an order of magnitude larger. As a rough comparison, the regression rate in a solid rocket at a typical rocket combustion chamber pressure may be on the order of 1.0 cm/sec whereas a typical hybrid using a classical polymeric fuel such as HTPB may have a regression rate on the order of 0.1 cm/sec. To compensate for the low regression rate, the surface area for burning must be increased. This is achieved through the use of a multi-port fuel grain such as that depicted in figure 2.9. Most attempts to increase the regression rate involve some method for increasing the heat transfer rate to the fuel surface. This can be done, for example, by increasing turbulence levels in the port or by adding roughness to the fuel grain. The difficulty is that as the heat transfer rate is increased, the radial velocity of the evaporating fuel toward the center of the port increases. This so-called "blocking effect" tends to decrease the temperature gradient at the fuel surface leading to a reduction in the amount of heat transfer increase that can be achieved. A regression rate increase on the order of $25 - 30$ %

or so can be obtained using this approach - not the factor of 2 or 3 that is needed for a single port design. [3]
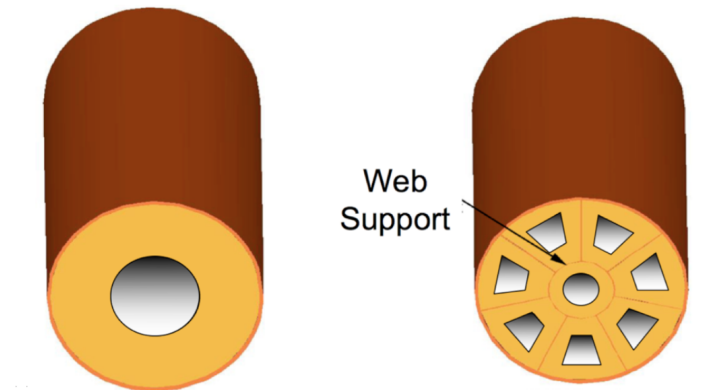
Figure 2.9: Single versus multi-port (wagon wheel) grain design. [3]

The most noticeable problem with the multi-port design is that the amount of fuel that can be loaded into a given volume is reduced, leading to an increase in the vehicle diameter for a given total fuel mass. There are other difficulties. The grain may need to be produced in segments and each segment must be supported structurally, adding weight and complexity. In addition, it is very difficult to get each port to burn at the same rate. If one burns slightly faster than another, then the oxidizer will tend to follow the path of least resistance leading to further disparity in the oxidizer flow rate variation from port to port. Toward the end of burning, the port that reaches the liner first forces the motor to be shut down prematurely leading to an inordinately large sliver fraction of unburned fuel. Small pressure differences from port to port can lead to grain structural failure and loss of fuel fragments through the nozzle. Aside from possible damage to the nozzle, the resulting increase in the overall O/F ratio leads to a reduction of the specific impulse and an increase in the nozzle throat erosion rate. Due to the high erosion, the nozzle area ratio decreases excessively leading to an additional loss of specific impulse. [3]

2.17   High regression rate fuels

In the late 1990s, the U.S. Air Force studied some exotic cryogenic designs for hybrid rockets. The fuel was liquid hydrogen and the oxidizer was solid oxygen. While investigating this unusual configuration, the Air Force also studied a different combination of cryogenic propellants: liquid oxygen and pentane, a hydrocarbon that is liquid at room temperature, but in this application was frozen solid using a bath of liquid nitrogen. The Air Force researchers found that solid pentane burns 3 to 4 times faster than normal fuels. [3] After some careful analysis, it appeared that mass transfer from the surface of this fuel involved more than simple evaporation.

Pentane produces a very thin, low viscosity, low surface tension, liquid layer on the fuel sur-

face when it burns. The instability of this layer driven by the shearing effect of the oxidizer gas flow in the port leads to the lift-off and entrainment of droplets into the gas stream greatly increasing the overall fuel mass transfer rate. The multitude of entrained droplets offers an enormous amount of surface area for evaporation and burning without the usual reduction caused by the blocking effect. [3] The basic mechanism is illustrated in figure 2.10.
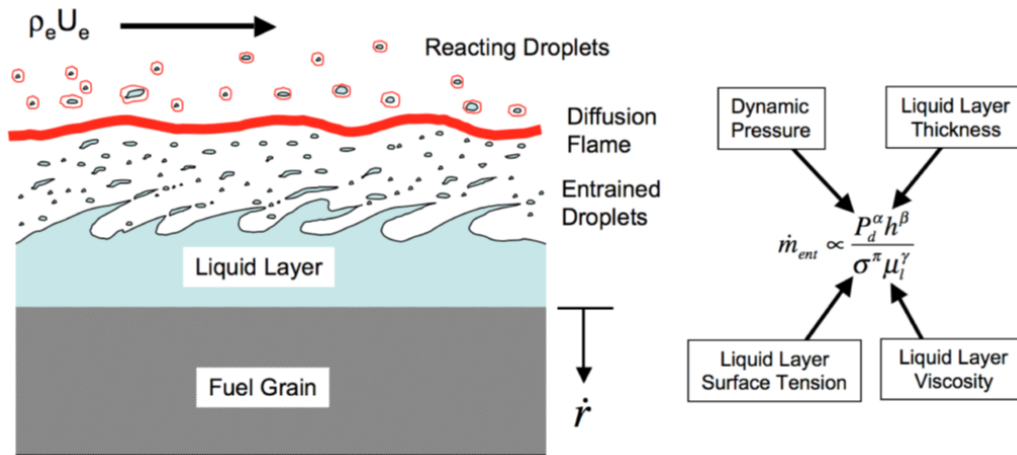
Figure 2.10: Liquid layer entrainment mechanism. [3]

In effect, this mechanism acts like a continuous spray injection system distributed along with the port with most of the fuel vaporization occurring around droplets convecting between the melt layer and the flame front. Since droplet entrainment is not limited by diffusive heat transfer to the fuel from the combustion zone, this mechanism can lead to much higher surface regression rates than can be achieved with conventional polymeric fuels that rely exclusively on evaporation. Equation (2.1) shows how the entrainment mass transfer component of the regression rate illustrated in figure 2.10 depends on the parameters of the flow. The exponents in (2.1) are determined empirically and are of order one. [3]

The key fuel properties are in the denominator of (2.1) - low surface tension and low viscosity of the melt layer, evaluated at the characteristic temperature of the layer. This forms the basis of a fundamental criterion that can be used to identify high regression rate fuels. Not all fuels that form a melt layer at the fuel surface will entrain. For example, high density-polyethelene (HDPE), which is a conventional hybrid fuel, does form a melt layer but the viscosity of the liquid is four orders of magnitude larger than pentane - too viscous to permit significant droplet entrainment. But frozen pentane itself is not a particularly promising fuel. It is not practical to have to soak the rocket motor in a liquid nitrogen bath before launch. This led to a search for a fuel that would be solid at room temperature, that would produce a low-viscosity liquid when it melted and would be strong enough to withstand the high-temperature, high-pressure, high-vibration environment of a rocket motor's combustion chamber. [3]

Figure 2.11 shows the effect of molecular weight on the melt temperature and boiling temperature for the normal alkanes. The middle curve is an estimate of the mean melt layer

temperature. The normal alkanes are linear, fully saturated hydrocarbons with the formula C_nH_{2n+2}. Familiar examples include methane (one carbon atom per molecule), ethane (two carbons), and propane (three carbons). As the number of carbon atoms in the molecule increases, the normal alkanes become room-temperature liquids, such as pentane (five carbons), and eventually solids such as waxes and polyethelene.
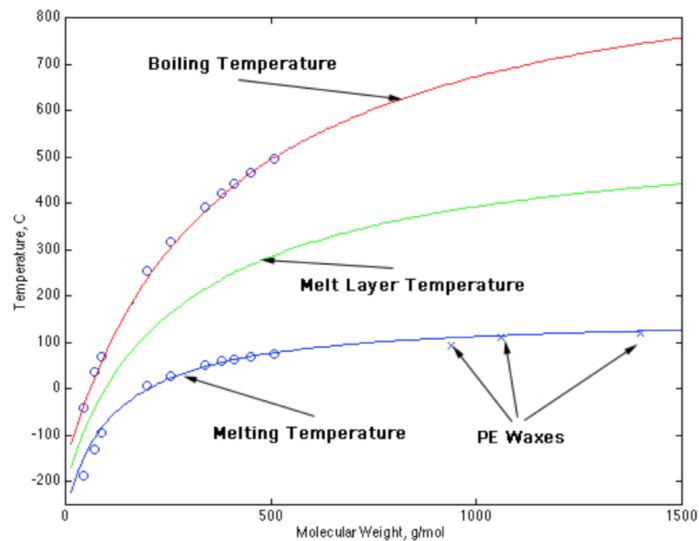
Figure 2.11: Effect of molecular weight on key temperatures for the normal alkanes. [3]

The melt layer temperature rises quickly at low molecular weights but much more slowly at high molecular weights. In general, the viscosity of a liquid tends to increase with molecular weight. But, the viscosity of most liquids tends to decrease exponentially fast with temperature. These facts can be applied to the melt layer of the normal alkanes. At high molecular weight, where the melt layer temperature increases only slowly, the viscosity increases through the dominance of the molecular weight effect. But at lower molecular weight, where the melt layer temperature increases rapidly, the tendency for the viscosity to increase with molecular weight is strongly offset by the tendency for viscosity to decrease with temperature. [3]

The design aim is to find a hydrocarbon with the right molecular weight. At high molecular weights, the viscosity of the liquid form of the alkane is too large for droplets to form readily. At low molecular weights, the alkanes are either gaseous or liquid or soft solids, much too weak to withstand the rigours of a rocket combustion chamber. In between is a sweet spot; Fuels with roughly 25 to 50 carbon atoms per molecule that are structurally robust and produce low-viscosity liquids when they melt. Figure 2.12 indicates schematically the range of carbon numbers that are likely to produce significant entrainment mass transfer.
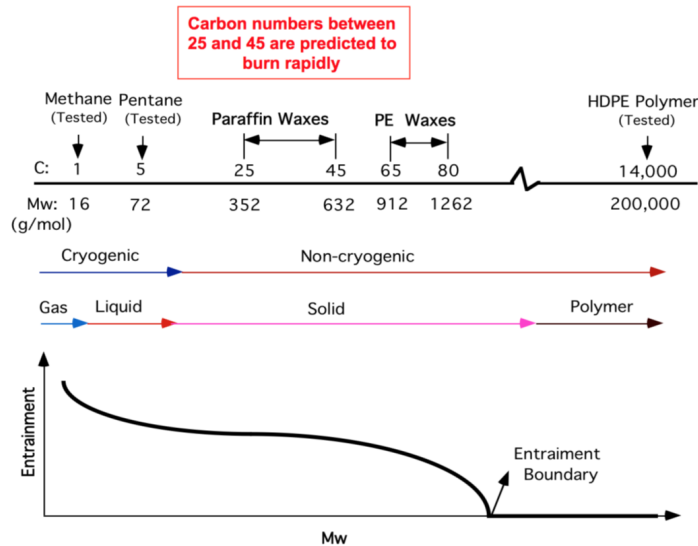
Figure 2.12: Schematic diagram indicating the normal alkanes that are expected to exhibit a high regression rate. [3]

These fuels, which include the paraffin waxes and polyethylene waxes, are predicted to have high regression rates at oxidizer mass fluxes covering a wide range of hybrid rocket applications. In fact, the viscosity of the melt layer in paraffin is comparable to pentane and so the regression rate is also similar despite the disparity in molecular weight. The kind of paraffin wax we use is a relatively high carbon number, fully refined, wax sometimes called sculptor's wax or hurricane wax. Fabricating, handling, and transporting traditional solid rocket propellants is usually very costly, but a paraffin-based fuel is easy to deal with in all those regards. It is nontoxic, and indeed not hazardous at all. What's more, the complete combustion of this fuel with oxygen produces no hazardous gases. The products are simply carbon dioxide and water. In contrast, the by-products of burning conventional solid rocket propellant often include carbon monoxide as well as acid-forming gases such as hydrogen chloride. [3]

Regression rates 3 to 4 times the predicted classical rate have been observed in a laboratory-scale motor using gaseous oxygen and industrial-grade paraffin wax. The specific impulse of a paraffin-based hybrid motor is slightly higher than that of a kerosene-based liquid motor and solid paraffin is approximately 20% denser than liquid kerosene. Figure 2.3 shows the ideal specific impulse of paraffin wax and HTPB burning with liquid oxygen. The waxes comprise a wide range of molecular weight, surface tension and viscosity and therefore can be used to create mixtures whose regression rate characteristics are tailored for a given mission. [3]

2.18 O/F **shift**

Over the course of a burn at a fixed oxidizer mass flow rate there is a tendency for the oxidizer to fuel (O/F) ratio to shift to higher values as the port opens up. This can be seen from the following. For a single circular port, a rough estimate of the O/F ratio at the end of the port

28

is, using (2.6)

$$O/F = \frac{\dot{m}_0}{\dot{m}_f} = \frac{\dot{m}_0}{\rho_f \pi D L \alpha (\frac{\dot{m}_0}{\pi r^2})^n} = \frac{\dot{m}_0^{1-n} D^{2n-1}}{4^n \pi^{1-n} \alpha \rho_f L} \quad (2.9)$$

where L is the port length and r is the port radius. Recall that the exponent is generally in the range $0.6 < n < 0.8$. As the port diameter increases the burning area increases and the oxidizer mass flux goes down. For $n > 0.5$ the decrease in mass flux dominates the increase in burning area and the overall generation rate of fuel mass goes down. The net effect is to cause the chamber pressure and hence the thrust to decrease naturally over the course of the burn as the vehicle mass decreases. This feature is desirable for a launch system where the payload is subject to a maximum acceleration constraint. Compare this to a solid rocket where the thrust tends to increase during the burn and a throttling option is not available.

Note the relatively strong sensitivity in figure 2.4 of the specific impulse to the O/F ratio. The change of O/F implies a change in specific impulse and a possible reduction in vehicle performance. This is a factor that must be taken into account by the designer seeking to get the maximum total delivered impulse from the motor. In practice, the maximum payload acceleration limit leads to a requirement that the oxidizer mass flow be throttled back while the port opens up and the two effects tend to offset one another. A typical case might be a factor of two decreases in the oxidizer mass flow rate and a factor of three increases in the port diameter. For $n = 0.62$ the net effect is less than a one percent change in O/F.

2.19   Combustion Fundamentals

"Combustion is generally recognized as a chemical reaction accompanied by the release of heat and light". [55] Combustion is perhaps described most simply as an exothermic reaction of a fuel and an oxidant. The overall objective of combustion in the present work, is the controlled generation of maximum combustion heat, with a minimum of harmful emission products. This section will be present an insight into all the basic fundamental aspects regarding combustion.

2.19.1   Combustion flames

Types of flames

Most fundamental studies of flame combustion are performed using gaseous or pre-vaporized fuels. Furthermore, although a flame can propagate through a static gas mixture, it is usual to stabilize the flame at a fixed point and supply it with a continuous flow of the combustible mixture. Under these conditions, flames can be classified as premixed and diffusion flames, depending on whether the fuel and air are mixed before combustion, or mixed by diffusion

in the flame zone. [56] Both types of flame can be further classified as laminar or turbulent, depending on the prevailing flow velocities. [56]

In the systems burning liquid fuels, if the fuel is not completely vaporized before entering the flame zone, heterogeneous spray combustion may take place. [56] This process, involving diffusion flame burning of individual evaporating fuel droplets, may be superimposed on a premixed turbulent flame zone. However, if both reactants are in the same physical state, the combustion process is described as homogeneous. [56]

Flammability limits

Not all fuel-air mixtures will burn or explode, flames can propagate through fuel-air mixtures only within certain limits of composition. If small amounts of combustible fuel gas or vapour are gradually added to the air, a point will be reached at which the mixture just becomes flammable. At this point, the percentage of fuel gas is called the lower flammable limit, weak limit, or lean limit. If more fuel is added, another point will eventually be reached at which the mixture will no longer burn. At this point, the percentage of fuel gas is called the upper flammable limit or rich limit. For many fuels, the weak limit corresponds to an equivalence ratio of around 0.5, and the rich limit to an equivalence ratio of around 3. [56]

An increase in pressure above atmospheric usually widens the flammability limit of gases and vapours. Even though the effect is usually less than that of pressure, the flammability range is also widened by an increase in temperature. In the practically important range of pressures from 10 kPa to 5 MPa, the weak flammability limit is not strongly pressured dependent. [56]

For liquid fuels, the formation of combustible mixtures is only possible within definite temperature limits. The lower temperature limit is taken as the minimum temperature at which the fuel's vapour pressure is enough to form the weak-limit volume concentration of vapour in the air. And below this temperature, the mixture becomes too weak for flammability. The upper-temperature limit corresponds to the rich-limit concentration, and a subsequent increase in temperature enriches the mixture to a condition of non-flammability. [56]

The lowest temperature at which a flammable mixture can be formed above the liquid phase is called the flashpoint when quoted for atmospheric pressure. The ease with which enough vapour is formed to produce a flammable mixture depends on the vapour pressure of the fuel. Highly volatile fuels produce high vapour pressures that give low flashpoints. [56]

2.19.2   Definitions

Density of a mixture

Any given mixture, which can be gas, liquid or solid, is defined as the weight per unit volume. In the case of a gas mixture, the density can be approximated using the ideal gas law, represented by Eq. 2.10:

$$PV = nR_uT \quad (2.10)$$

Mixture ratios

The mixture ratio is one of the most important parameters in a combustor system because it affects the combustor's performance, life span, efficiency and pollution characteristics.

The mixture ratio represents the ratio in which the fuel and air are present in a system. In premixed combustion systems, there is only one mixture ratio throughout the entire combustion process. However, in the present non-premixed combustion (diffusion flame) study case, there is an infinite range of ratios, that spreads from pure air to pure fuel. The mixture ratio can be defined through the FAR, the equivalence ratio, through excess air and by the mixture fraction. The FAR is commonly used in the gas turbine industry and is the inverse of the AFR, which is more used for internal combustion engines. [57] The FAR refers to the ratio of fuel to the air at any given moment, and is expressed through Eq.2.11:

$$FAR = \frac{m_f}{ma} \quad (2.11)$$

In order to determine if a mixture is rich or lean, i.e., excess fuel or air respectively, an equivalence ratio (Φ) is used, and is represented by Eq. 2.12. The stoichiometry describes the actual FAR compared to the chemically correct or stoichiometric ratio. The primary zone is typically rich (Φ >1.0), in order to promote reaction stability (e.g. avoid flameout).

$$\Phi = \frac{FAR_{actual}}{FARstoi} = \frac{m_f/m_a}{(m_f/m_a)_s} \quad (2.12)$$

The mixture fraction (ξ) is a very useful variable in combustion modelling, in particular for diffusion flames. This is because all parameters have a value of infinity when in the presence of pure fuel or pure air (FAR and AFR respectively). This is no good for computer modellers since computers face many difficulties when they attempt to calculate infinities [58]. The mixture fraction is then defined as the ratio by mass of mixture which originated from the fuel, as opposed to the oxidizer stream, and is represented by Eq. 2.13:

$$\xi = \frac{m_f}{m_f + m_a} = \frac{m_f/m_f}{m_f/m_f + m_a m_f} = \frac{1}{1 + AFR} \quad (2.13)$$

As we can verify with Eq. 2.13, in the air stream (when the AFR $\rightarrow \infty$) $\xi = 0$, and in the fuel stream (when $AFR = 0$), $\xi = 1$.

2.19.3 Combustion Stoichiometry

When it comes to the complete oxidation of a simple hydrocarbon fuel ($C_x H_y$) there is always the formation of CO_2 from all of the carbon, and H_2O, from all of the hydrogen. However, there are more species present in combustion products. The nitrogen present participates in the combustion process, which in turn produces the unwanted NO_x. Another aspect to take into account while analysing Eq. 2.14, is that combustion is not always complete, and the effluent gases contain unburned and partially burned products in addiction to CO_2 and H_2O. N_2 does not alter significantly the O_2 balance, however, it does have a major impact on the thermodynamics, chemical kinetics, and formation of pollutants in combustion systems [58]. This said the complete stoichiometric relation for complete oxidation of a hydrocarbon fuel ($C_n H_m$) in N_2O has been calculated for the studying case with the CEA NASA software. CEA allows the user to introduce each of the species, as well as their concentration in the fuel and then calculates several user-defined output thermodynamic properties, which include the stoichiometric ratio.

A trade-off has to be made between the number of species and the memory requirements, so the products with a mass fraction magnitude lower than 10^3 have been neglected.

This relation for a given hydrocarbon fuel, with the general composition $C_n H_m$, is shown in Eq. 2.14:

$$C_n H_m + \left(n + \frac{m}{4}\right) O_2 \longrightarrow nCO_2 + \frac{m}{2} H_2O \quad (2.14)$$
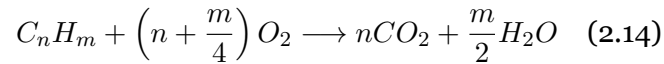
2.19.4 Absolute enthalpy, enthalpy of formation and enthalpy of combustion

The Absolute enthalpy (h_i), also known as standardized enthalpy, is very a very important variable in chemical reacting systems. For any given species, it is possible to define an absolute enthalpy, which is the sum of the enthalpy of formation (h_f) and the sensible enthalpy change (Δh_s). The first takes into account the energy associated with the chemical bonds, while Δh_s is associated only with the temperature. Eq. 2.15 represents the absolute enthalpy at a temperature T:

$$\overline{h}_i(T) = \overline{h}_{f,i}^o(T_{ref}) + \Delta \overline{h}_{s,i}(T_{ref}) \quad (2.15)$$

where $\overline{h}_{s,i} \equiv \overline{h}_i(T) - \overline{h}_{f,i}^o(T_{ref})$

The subscript ref presented in Eq. 2.15 refers to the standard reference state. Thus, the

standard state temperature and pressure are $T_{ref} = 25°C$ (298.15 K) and $P_{ref} = P^o = 1$ atm (101.325 Pa), respectively, which are consistent with Chemkin and NASA thermodynamic databases [59]. The enthalpy of formation is conventionally adopted as zero for the elements that are in their natural state, and for enthalpies of formation other than the reference state, these are tabulated in many literatures.

Once expressed the enthalpy for mixtures of reactants and mixtures of products, it is possible to define the enthalpy of combustion, when it comes to combustion reactions. For any given complete combustion process, for the products to exit at the same temperature as the entering reactants, heat necessarily has to be removed from the combustor. Applying the first law of thermodynamics (Eq. 2.16), the amount of heat removed can be related to the absolute enthalpies of the reactants and the products, as shown in Eq. 2.17:

$$q_{cv} - w_{cv} = h_0 - h_i + \frac{1}{2}(v_0^2 - v_i^2) + g(z_0 - z_i) \quad (2.16)$$

$$q_{cv} = h_0 - h_i = h_{prod} - h_{reac} \quad (2.17)$$

thus, the definition of enthalpy of combustion (or enthalpy of reaction (Δh_R) per mass of mixture), is given by Eq. 2.18, or in terms of extensive properties, which is given by Eq. 2.19:

$$\Delta h_R \equiv q_{cv} = h_{prod} - h_{reac} \quad (2.18)$$

$$\Delta h_R \equiv H_{prod} - H_{reac} \quad (2.19)$$

2.19.5   Heat of combustion

The heat of combustion (Δh_c), commonly known as the heating value, is the energy released as heat when a compound undergoes complete combustion with oxygen and is symmetric to the enthalpy of reaction. There are two heating values; the Higher Heating Value (HHV) and the Lower Heating Value (LHV). The HHV is the heat of combustion calculated, with the assumption that all of the water in the products has condensed to the liquid state. Is within this state that most of the energy is released. The calculation of the LHV assumes that none of the water is condensed. The standard state of the heating values for a variety of hydrocarbons are present in several literatures. The HHV and the LHV can be related by Eq. 2.20:

$$HHV = LHV + h_v(n_{H2O,out}/n_{fuel,in}) \quad (2.20)$$

2.19.6 Adiabatic flame temperature

For a given combustion process, the adiabatic flame temperature (T_{ad}) is the maximum temperature that the products can achieve, forgiven reactants. Lower temperatures can occur due to heat transfer, incomplete combustion and dissociation. The maximum (T_{ad}) for a given mixture occurs at stoichiometric proportions. [59]

In combustion studies, two adiabatic flame temperatures can be used; one for the combustion at constant pressure and the other one for constant volume. If combustion occurs at constant pressure, the absolute enthalpy of the reactants at T_ref is equal to the absolute enthalpy at the final state ($T = T_{ad}$, $P = 1atm$). The first law statement, represented by Eq. 2.21, is what defines this constant-pressure adiabatic flame temperature, and was obtained by applying Eq. 2.16:

$$h_{reac}(T_i, P) = h_{prod}(T_{ad}, P) \quad (2.21)$$

Another parameter of interest is the heat capacity (C), which is defined as the ratio of the heat added (or removed from an object), to the resulting temperature, as shown in Eq. 2.22:

$$C \equiv \frac{Q}{\Delta T} \quad (2.22)$$

More heat is required from the system to achieve the same temperature change for an ideal gas at constant pressure than it is required at constant volume. This is because, at constant volume, all heat added is used to raise the temperature. On the other hand, at constant pressure, some of the heat performs work. The specific heat capacity at constant pressure (cp) is represented by Eq. 2.23:

$$c_p = (\frac{\partial h}{\partial T})_p \quad (2.23)$$

2.20 Emissions

As could be realized during this work, the pollutants that are most concerned are CO, UHC, NO_x and PM (or smoke). At low power conditions, the inlet combustor pressure and temperature are relatively low, which implies that the reaction rates for kerosene-type fuels are low. These fuels must be adequately atomized, evaporated and combusted, with a sufficient residence time at high enough temperatures to achieve the best combustion efficiency, i.e., maximum conversions of the fuel into CO_2. When this is not the case and the flow field permits fuel vapour to exit the combustor without any reaction (or partially reacted), to species of lower molecular weights, UHC will be formed and be present along with the exhaust gases. If a portion of this flow field intersects with a zone in which temperature has been decreased, e.g. due to film-cooling, these incomplete or quenched reactions, lead to the production of
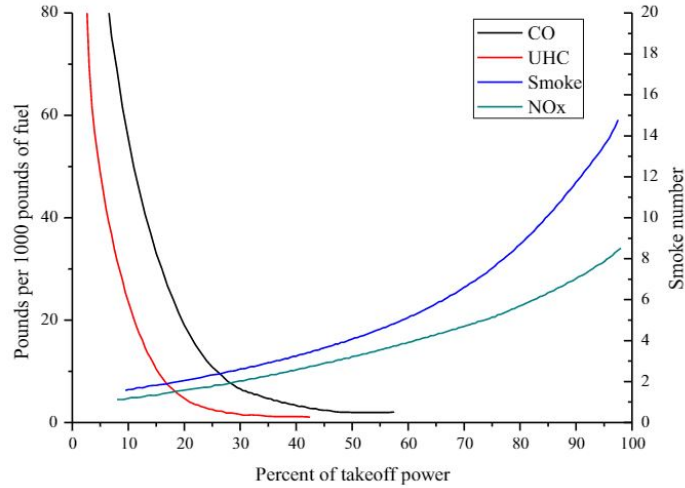
Figure 2.13: Relation between the powers output of the gas turbine and the number of emissions. [58]

CO.

With the increase of engine power, the high air pressures and temperatures lead to fast reactions, meaning that CO and UHC are virtually zero. However, at these high temperatures, the formation of NO_x and PM become prevalent. This as we can see presents a problem because as efforts are held to, e.g., reduce CO and UHC, this leads to an inevitable increase in NO_x and PM emissions, as can be seen in Figure 2.13. This is a problem that persists due to the configuration of modern combustors, thus to solve these problems other combustor configurations have to be developed, and staged combustion is a very interesting alternative.

2.20.1   Hydrocarbon oxidation and CO formation

CO is an intermediate species in the oxidation of hydrocarbon fuels to CO_2 and H_2O. Within fuel-rich regions of the flame, the CO levels are high because there is not enough oxygen for complete combustion. Thus, CO can only be oxidized when a sufficient amount of air is mixed with the hot gases. The extent to which CO is actually oxidized depends greatly on the kinetics of oxidation reactions and the manner of cooling. [60] The following four equations describe the oxidation of CO [61]:

$$CO + O_2 \rightleftharpoons CO_2 + O \quad (2.24)$$

$$O + H_2O \rightleftharpoons OH + OH \quad (2.25)$$

$$CO + OH \rightleftharpoons CO_2 + H \quad (2.26)$$

$$H + O_2 \rightleftharpoons OH + O \quad (2.27)$$

35

Eq. 2.24 serves as the initiation of the chain sequence but does not contribute significantly to CO_2 formation, because it is a slow reaction. Eq. 2.26 is also an initiation chain sequence but is the principal reaction in the overall scheme; it produces H atoms that react with O_2 to form OH and O (Eq. 2.27). These radicals react with CO and H_2O, through Eq. 2.26 and Eq. 2.25 respectively.

2.20.2   Zeldovich reaction and NO_x formation

Two mechanisms that are responsible for the formation of NO_x; these are thermal NO_x and prompt NO_x. When there is no fuel-bond nitrogen, thermal NO_x mechanism is predominant in combustion systems with flame temperatures greater than 1800 K. [62] Thermal NO_x is then associated with the formation of NO_x through high-temperature oxidation of diatomic nitrogen (N_2) and O_2, found in the air for combustion. These then dissociate into their atomic states and participate in a series of reactions that produce thermal NO_x. The greater the residence time of nitrogen at that temperature, the higher will be the NO_x formation. [63]

The three principal reactions that produce thermal NO_x, are represented in Eq. 2.28, Eq. 2.29 and Eq. 2.30, which are known as the extended Zeldovich mechanism. Zeldovich was the first to notice the importance of Eq. 2.28 and Eq. 2.29 for thermal NO_x formation. [64] Eq. 2.30 was added later by [65], which describes the reaction of the nitrogen atom in 2.28 with an OH radical to form NO. Eq. 2.30 makes a significant contribution to the formation of NO_x, however, Eq. 2.28 is the rate-limiting step for the formation of thermal NO_x, because of its high activation energy. [62]

$$N_2 + O \rightleftharpoons NO + N \quad (2.28)$$

$$N + O_2 \rightleftharpoons NO + O \quad (2.29)$$

$$N + OH \rightleftharpoons NO + H \quad (2.30)$$

The rate at which NO_x can be produced by the Zeldovich reaction, can be estimated through the equilibrium concentration of O_2 in the post-flame zone, using Eq. 2.31:

$$\frac{d[NO]}{dt} = 6 \times 10^{16} T_{eq}^{-0.5} exp\left(\frac{-69.090}{T_{eq}}\right)[O_2]_{eq}^{0.5}[N_2]_{eq} \qquad \left[\frac{moles}{cm^3 sec}\right] \quad (2.31)$$

Pollutant emissions are generally expressed as Emission Index (EI), defined as grams per pollutant per kilogram of fuel (g/kg fuel), for a certain power setting. [66]

Prompt NO_x occurs in the earliest stage of combustion and is associated with the reaction of molecular N_2 with radicals such as C, CH and CH_2, which are fragments derived from fuel.

This reaction results in the formation of nitrogen species such as Cyanonaphthalene (NCN), which in turn undergo fast oxidation with OH and O radical species to form NO [67], through Eq. 2.32 and Eq. 2.33 respectively:

$$NCN + OH \rightleftharpoons NO + HCN \quad (2.32)$$

$$NCN + O \rightleftharpoons NO + CN \quad (2.33)$$

It is important to note that there is very little prompt NO_x formation in the post flame zone, but this mechanism can be a great source of NO_x formation when at low combustion temperatures of oxygenated fuels, such as biodiesel. [68]

Chapter 3

DHX-4 Phoenix Hybrid Rocket Motor

In this chapter will be introduced the experimental-related activities that are been used for performing the numerical analyses in this thesis.

Since 2006 the Hybrid Propulsion Team of DARE has been developing hybrid rocket technology. To keep alive the hybrid rocket technology proficiency of DARE, Project Phoenix (see figure 3.1) began to train new members of the association. The purpose of the venture is to realize a test motor to experiment with new hybrid solutions, which may be used in the upcoming Stratos III. Besides serving as a testbed, the DHX-4 Phoenix rocket motor is fully compatible with the CanSat V7 rocket [1].

Figure 3.1: Project Phoenix Mission Patch

3.1 DHX-4 Design

The main design requirements are:

– Motor Type Hybrid Propulsion;

– Total Impulse 4000 Ns;

– Specific Impulse 185 s;

---

[1]The Cansat V7 is the last version of a cansat launcher commissioned to DARE in 2007 by the European Space Education Resource Office of the European Space Agency. It can carry up to 4 payloads to an apogee of 1 kilometre [69]

– Average Thrust 1000 N;

– Burn Time 4 s;

– Fuel Sorbitol, Paraffin;

– Oxidizer Nitrous Oxide.

3.1.1 Tank and Feed System

For the rocket in the study the oxidizer chose has been Nitrous Oxide. Nitrous Oxide is considered a green propellant: it's nontoxic when released into the atmosphere, it contains an adequate oxygen content for a combustion reaction and its positive heat of formation adds to combustion energy. [70] The main advantage of this choice is that Nitrous Oxide is a Self-Pressurizing Propellant: it exists as a saturated liquid at room temperature and has a relatively high vapour pressure of 5.279 MPa at 293.15 K. Therefore it can be injected into a combustion chamber without the aid of turbopumps or other pressurization systems, reducing the weight, cost and complexity of the motor. [71] The required Tank Pressure can be achieved just by heating the tank.

The oxidizer tank used, shown in figure 3.2, consist of a cylinder with an internal radius of 45 mm and height of 474 mm, with a wall thickness of 5 mm. The dry mass of the tank is about 0.5 kg and can hold about 2 kg of oxidizer at a pressure of 60 bar.

Figure 3.2: Close-up of the tank and the motor

The feed system has the purpose of transfer the liquid fuel from an external container to the tank of the motor, or run tank, and then transfer it from the run tank to the chamber.

Sensors, hoses and connectors aside, the main features of the subsystem are [72]:

- Main Valve (MV) is the main gateway connecting the run tank to the combustion chamber. During the burn phase, the oxidizer flows through it.

- Ignition Valve connects the run tank to the combustion chamber as the MV, but let's flow only the small amount of oxidizer required to ignite the motor.

- Bleed Valve is attached directly to the tank and is used to discharge the gas oxidizer in excess. This process is necessary to obtain saturated vapour inside the tank.

- Fill Valve is attached to the external Nitrous Oxide container and opens to transfer the oxidizer to the run tank.

- Dump Valve, necessary to discharge the oxidizer trapped inside the hoses while all the other valves are closed. It is also used to empty the run tank of the residual oxidizer left after the burn, if the MV is closed before the total discharge, to avoid damaging the fuel grain.

3.1.2   Combustion Chamber

The propulsive unit of the motor is composed of three subsystems: injector plate, combustion chamber and nozzle. The envelope of the motor is an aluminium pipe with an internal diameter of 60 mm and a length of 245 mm, where the fuel grain is integrated and the nozzle and the injection assembly are inserted at the extremities.

3.1.3   Injector Plate

This part is composed of a small empty gap that connects the hose coming from the feed system to the propulsive unit to a 1 mm thick aluminium plate, where holes are drilled to create the injection orifices.

3.1.4   Fuel Grain

The fuel grain is a hollow cylinder with an internal diameter at the beginning of the burn of 36 mm, and an external diameter of 58 mm. The grain is wrapped in a cardboard liner 1 mm thick. The cylinder length is about 236 mm, which is less of the empty space inside the combustion chamber. It leans against the convergent part of the nozzle, thus leaving an empty space between the injector plate and the grain itself. This empty space constitutes the Pre-Combustion Chamber and is essential for the diffusion of the oxidizer inside the chamber. This rocket uses a blend of Sorbitol and Paraffin, in particular Shell Sarawax SX70, where the first provides a high density and good structural properties, while the latter is used to increase the regression rate and specific impulse. The grain composition is 80% Sorbitol and 20% Paraffin.

3.1.5 Nozzle

The nozzle is a bell-shaped nozzle made in graphite. Its properties are listed in table 3.1.

Table 3.1: Nozzle Properties

Expansion Ratio	7.32
Convergence Angle	35 degrees
Divergence Angle	15 degrees
Throat Radius	8.5 mm
Total Length	79.7 mm

3.2 DHX-4 Tests

The tests lasted six months, from late June to November 2016. 8 tests have been performed, with 2 different motor configurations. The experiments have been performed on Dawn's Labscale Hybrid Engine Test Facility.

3.2.1 Test Reports

The Phoenix Test Campaign consisted of 8 tests, listed in table 3.2.

Table 3.2: Test Matrix

Test Number	Date	Burn Time	Description
Test 1	9 July	-	Main Valve Mulfunction
Test 2	12 July	-	Igniter Failure
Test 3	20 July	3.8 s	Successful, config. A
Test 4	24 Aug.	-	Overheating of the Tank
Test 5	10 Sep.	2.7 s	Successful, config. A
Test 6	10 Sep.	2 s	Successful, config. A
Test 7	14 Oct.	1.6 s	Successful, config. B
Test 8	25 Nov.	-	Injector Plate Failure

The thesis will only rely on Test 5 to fulfil the research objectives. Test 5 was one of the tests that were successfully performed with the first injector configuration (configuration A), the main valve was shut after 2.7 seconds.

3.3 Experimental Data

This section provides the data that has been obtained from the experimental results, particularly from Test 5, since that is what will be studied.
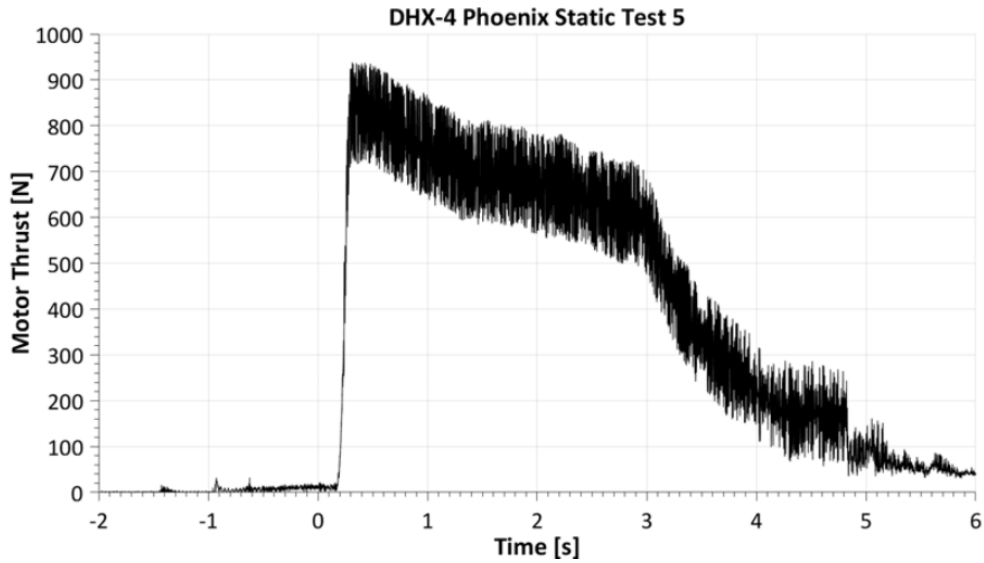
Figure 3.3: Test 5 Motor Thrust

In figure 3.3 different sections of the curve shall be identified. Before t = 0 s it coincides with the X-axis since the motor is off. During ignition, the values quickly rise to their maximum. Then the nominal burn phase begins, the liquid oxidizer is injected into the combustion chamber and the curve slowly descends. When the liquid Nitrous in the tank depletes, the curve abruptly climbs down to a second less efficient burning phase, where the oxidizer is injected into the gas phase. When the main valve is closed or the run tank is completely empty, the combustion stops and the curve leans on the X-axis again.

The average values are listed in the table 3.3, while the peak values are reported in the table 3.4.

Table 3.3: Average Values of the Experimental Results

	Test 3	Test 5	Test 6	Test 7
Nominal Burn Time [s]	3.8	2.7	2	1.6
Specific Impulse [s]	138	148	151	170
Thrust [N]	680	704	750	822
Thrust Coefficient	1.31	1.27	1.26	1.28
Characteristic Velocity [m/s]	1025	1139	1174	1303
Oxidizer Mass Flow [kg/s]	0.278	0.360	0.385	0.336
Fuel Mass Flow [kg/s]	0.120	0.113	0.124	0.157
Regression Rate [mm/s]	2.82	2.12	3.2	4
Injection Pressure Drop [bar]	7.9	9.3	7.87	17.43
Combustion Chamber Pressure [bar]	22.6	24.2	26.2	28.3

Table 3.4: Peak Values of the Experimental Results

	Test 3	Test 5	Test 6	Test 7
Thrust [N]	877	877	884	1090
Characteristic Velocity [m/s]	1263.7	1318	1327	1587
Combustion Chamber Pressure [bar]	28.3	28.4	30.38	35.1

It is important to specify that the performance parameters, such as the combustion chamber pressure and the thrust, decrease over the increasing burn time.

The measured efficiencies are listed in the table 3.5. For higher average pressure, the efficiency increases as the average pressure of the system slightly increase. However, the efficiency is rather low, fluctuating between 70% and 80%.

Table 3.5: Combustion Efficiency

	Measured c^* [m/s]	Combustion Efficiency
Test 3	1025	72.18%
Test 5	1139	80.21%
Test 6	1174	82.67%
Test 7	1303	91.76%

3.4 Parameters

While some parameters, like the length or the composition of the grain, prevailed constant, other values change from test to the other. The quantities are listed in tables 3.6 and 3.7.

Table 3.6: Constant Inputs Regardless of the Test

Grain Length [m]	0.236
Burn Rate Coefficient [m/s]	0.004
Port Diameter [m]	0.036
Tank Volume [m^3]	0.003
Fuel Density [kg/m^3]	1260
Pressure Exponent	0.31
Throat Diameter [m]	0.017
Pressure Line Losses [bar]	10

Table 3.7: Variable Inputs

	Test 3	Test 5	Test 6	Test 7
Burn Time [s]	3.8	2.7	2	1.6
Initial Tank Pressure [bar]	57.4	58	58.5	57
Initial N_2O Mass [kg]	2	1.55	1.57	1.45
Average N_2O Mass Flow Rate	0.321	0.360	0.385	0.336
N_2O Flow Rate Constant	1.0932	1.0728	1.0559	1.0740
Combustion Efficiency %	72.18	80.21	82.67	91.76
Pressure Drop %	35	30	30	40

Chapter 4

CFD Simulations

In this work, was created a predictive model by building upon previously presented results [73] and validated it through a rebuilding of the experimental data taken from the firing test 5 of the DHX-4. The computational approach is able to compute the correct flow field, capture the fluid/surface interaction without losing predictive capabilities, and account for the radioactive heat transfer. A particular hypothesis employed is that, in super-critical conditions, the turbulent diffusion and convection of liquefied paraffin wax occurs similarly to that of the other species constituting the mixture and, as a consequence, that the entrainment is part of the turbulent mixing process.

The CFD software used was ANSYS. ANSYS is a software suite that spans the entire range of physics, providing access to lots of fields of engineering simulation that a design process requires. In particular, the module Fluent is appropriate for this work. Fluent's models are focused on fluids flow and chemical reactions, including a very good model to run first-approach simulations of combustion systems. [74]

The computer used for creating the case was an 8-core CPU Intel i7-4770 with a 3.4 GHz clock and 32 gigabytes of RAM. For running the case it has been used a cluster with 92 cores.

The procedures for performing a simulation in ANSYS Fluent are the following:

1. Design the geometry of the system.

2. Generate an appropriated mesh.

3. The physical modelling is afterwards defined. It is defined, for example, the equations of fluid motion, enthalpy, and species conservation.

4. Boundary conditions are defined, i.e. specifying the fluid behaviour and properties at all bounding surfaces of the fluid domain.

5. Analysis and visualization of the resulting solution.

4.1 Turbulent flow analysis

There is a lot to talk about when it comes to turbulent flow combustion modelling because this is a very broad subject area. Thus, it will not be possible to review all of the important aspects regarding this subject in the present work. The focus in this section will then be to introduce the CFD-based modelling techniques used in this work, to introduce the governing equations that will be solved in the CFD code (ANSYS Fluent), and to present the closure schemes that are used to calculate the turbulent transport.

4.1.1 Turbulence models

Techniques have been developed throughout the years in order to obtain useful information and to allow predictions of turbulent flows. These techniques can be divided into two basic levels; the First-order Eddy Viscosity/diffusivity (EVM) models and the second-order Reynolds Stress Models (RSM); within these models, several variants exist, however, the predictions obtained from this study will rely on the RSM. The RSM was chosen among other models such as the standard $k - \varepsilon$ model, because it was verified that better results were obtained from the RSM, despite being more CPU expensive and more difficult to converge than EVM. It was also chosen because it is proven that RSM is more advantageous over other models, in complex 3D swirling flows such as the combustor in the study, and consequently it is an efficient way to improve the simulation accuracy. [75]

It is possible, in theory, to directly resolve the whole spectrum of turbulent scales using an approach known as direct numerical simulation (DNS) [60], in which the Navier-Stokes equations are numerically solved without the need to use turbulence models. However, it is not feasible for practical engineering problems involving high Reynolds number flows. [60] For high Reynolds number flows, the cost becomes prohibitive. There are, however, two other numerical simulation methods, not DNS, the Large Eddy Simulation (LES) and the Reynolds Average Navier-Stokes (RANS).

4.1.2 Governing Equations

One of the best methods of analysing turbulent flows is to write out the partial differential equations that embody the basic conservation principles, i.e, mass, momentum, energy and species; perform a Reynolds decomposition and then average the equations over time. [76] The result of this decomposition is then the so-called Reynold Averaged Navier-Stokes (RANS) equations.

In the Reynolds Average Navier-Stokes (RANS) method the flow properties are decomposed into an average value and turbulence-related fluctuation.

The Reynolds Averaged Navier-Stokes (RANS) equations are the following:

- Continuity:

$$\frac{\partial \bar{p}}{\partial t} + \frac{\partial}{\partial x_i}(\bar{p}\widetilde{u}_i) = 0 \quad (4.1)$$

- Momentum:

$$\frac{\partial}{\partial t}(\bar{p}\widetilde{u}_i) + \frac{\partial}{\partial x_j}(\bar{p}\widetilde{u}_i\widetilde{u}_j) - \frac{\partial}{\partial x_j}(\overline{pu_iu_j}) - \frac{\partial}{\partial x_j}\left[\mu\left(\frac{\partial \widetilde{u}_i}{\partial x_j} + \frac{\partial \widetilde{u}_j}{\partial x_i} - \frac{2}{3}\partial_{ij}\frac{\partial \widetilde{u}_i}{\partial x_j}\right)\right] = \frac{\partial \bar{p}}{\partial x_i} \quad (4.2)$$

- Scalar transport:

$$\frac{\partial}{\partial t}(\bar{p}\widetilde{\Upsilon}_\alpha) + \frac{\partial}{\partial x_i}(\bar{p}\widetilde{u}_i\widetilde{\Upsilon}_\alpha) + \frac{\partial}{\partial x_i}(\overline{pu_i\Upsilon_\alpha}) - \frac{\partial}{\partial x_i}(\Gamma_\alpha\frac{\partial \widetilde{\Upsilon}_\alpha}{\partial x_i} = \widetilde{\omega}_\alpha \quad (4.3)$$

In laminar flow, the fluid stress is proportional to the rate of strain with the viscosity being a constant of proportionality. [77] In turbulent flow, the turbulent stress is related to the mean rate of strain through turbulent viscosity (μ_T). This is the so-called Boussinesq's hypothesis, and is represented in:

$$-\overline{pu_iu_j} = \mu_T\left(\frac{\partial \widetilde{u}_i}{\partial x_j} + \frac{\partial \widetilde{u}_j}{\partial x_i}\right) - \frac{2}{3}\bar{p}k\partial_{ij} - \frac{2}{3}\mu_T\frac{\partial \widetilde{u}_k}{\partial x_k}\partial_{ij} \quad (4.4)$$

The turbulent viscosity is calculated from the kinetic energy of turbulence (k) and from the dissipation rate (ε) [77]; these are related through Eq. 4.5:

$$\mu_T = \bar{p}C_\mu\frac{k^2}{\varepsilon} \quad (4.5)$$

The transport equations for k and ε are used, and the scalar flux is set proportional to the mean scalar gradient [77], as shown in Eq. 4.6:

$$-\overline{pu_i\phi} = \left(\frac{\mu}{\sigma} + \frac{\mu_T}{\sigma_T}\right) \quad (4.6)$$

For this study will be used, and this software provides the following choices of turbulence models:

1. **Spalart-Allmaras model**

   The Spalart-Allmaras model is a relatively simple one-equation model that solves a modelled transport equation for the kinematic eddy (turbulent) viscosity. This embodies a relatively new class of one-equation models in which it is not necessary to calculate a length scale related to the local shear layer thickness. The Spalart-Allmaras model was designed specifically for aerospace applications involving wall-bounded flows and

has been shown to give good results for boundary layers subjected to adverse pressure gradients. It is also gaining popularity in turbomachinery applications. [60]

In its original form, the Spalart-Allmaras model is effectively a low-Reynolds-number model, requiring the viscosity-affected region of the boundary layer to be properly resolved. In ANSYS FLUENT, however, the Spalart-Allmaras model has been implemented to use wall functions when the mesh resolution is not sufficiently fine. This might make it the best choice for relatively crude simulations on coarse meshes where accurate turbulent flow computations are not critical. [60]

On a cautionary note, the Spalart-Allmaras model is still relatively new, and no claim is made regarding its suitability to all types of complex engineering flows. Furthermore, one-equation models are often criticized for their inability to rapidly accommodate changes in length scale, such as might be necessary when the flow changes abruptly from a wall-bounded to a free shear flow. [60]

2. k-ε **models**

This section presents the standard, RNG, and realizable k-ε models. All three models have similar forms, with transport equations for k and ε. The major differences in the models are as follows:

- the method of calculating turbulent viscosity

- the turbulent Prandtl numbers governing the turbulent diffusion of k and ε

- the generation and destruction terms in the ε equation

- The transport equations, the methods of calculating turbulent viscosity, and model constants are presented separately for each model. The features that are essentially common to all models follow, including turbulent generation due to shear buoyancy, accounting for the effects of compressibility, and modelling heat and mass transfer.

(a) **Standard k-ε model**

The simplest "complete models" of turbulence are the two-equation models in which the solution of two separate transport equations allows the turbulent velocity and length scales to be independently determined. The standard k-ε model in ANSYS FLUENT falls within this class of models and has become the workhorse of practical engineering flow calculations in the time since it was proposed by Launder and Spalding [78]. Robustness, economy, and reasonable accuracy for a wide range of turbulent flows explain its popularity in industrial flow and heat transfer

simulations. It is a semi-empirical model, and the derivation of the model equations relies on phenomenological considerations and empiricism. [60]

As the strengths and weaknesses of the standard k-ε model have become known, improvements have been made to the model to improve its performance. Two of these variants are available in ANSYS FLUENT: the RNG k-ε model and the realizable k-ε model. [79]

(b) **Renormalization-group (RNG) k-ε model**

The RNG k-ε model was derived using a rigorous statistical technique (called renormalization group theory). It is similar in form to the standard k-ε model, but includes the following refinements:

  i. The RNG model has an additional term in its ε equation that significantly improves the accuracy for rapidly strained flows.

  ii. The effect of swirl on turbulence is included in the RNG model, enhancing accuracy for swirling flows.

  iii. The RNG theory provides an analytical formula for turbulent Prandtl numbers, while the standard k-ε model uses user-specified, constant values.

  iv. While the standard k-ε model is a high-Reynolds-number model, the RNG theory provides an analytically-derived differential formula for effective viscosity that accounts for low-Reynolds-number effects. Effective use of this feature does, however, depend on the appropriate treatment of the near-wall region.

These features make the RNG k-ε model more accurate and reliable for a wider class of flows than the standard k-ε model.

The RNG-based k-ε turbulence model is derived from the instantaneous Navier-Stokes equations, using a mathematical technique called "renormalization group" (RNG) methods. The analytical derivation results in a model with constants different from those in the standard k-ε model, and additional terms and functions in the transport equations for k and ε.

(c) **Realizable k-ε model**

The realizable k-ε model is a relatively recent development and differs from the standard k-ε model in two important ways.

The realizable k-ε model contains a new formulation for the turbulent viscosity. A new transport equation for the dissipation rate, ε, has been derived from an exact equation for the transport of the mean-square vorticity fluctuation.

The term "realizable" means that the model satisfies certain mathematical constraints on the Reynolds stresses, consistent with the physics of turbulent flows. Neither the standard k-ε model nor the RNG k-ε model is realizable.

An immediate benefit of the realizable k-ε model is that it more accurately predicts the spreading rate of both planar and round jets. It is also likely to provide superior performance for flows involving rotation, boundary layers under strong adverse pressure gradients, separation, and recirculation.

3. k-ω **models**

This section presents the standard and shear-stress transport (SST) k-ω models. Both models have similar forms, with transport equations for k and ω. The major ways in which the SST model differs from the standard model are as follows:

- gradual change from the standard k-ω model in the inner region of the boundary layer to a high-Reynolds-number version of the k-ε model in the outer part of the boundary layer

- modified turbulent viscosity formulation to account for the transport effects of the principal turbulent shear stress

- The transport equations, methods of calculating turbulent viscosity, and methods of calculating model constants and other terms are presented separately for each model.

(a) **Standard k-ω model**

The standard k-ω model in ANSYS FLUENT is based on the Wilcox k-ω model, which incorporates modifications for low-Reynolds-number effects, compressibility, and shear flow spreading. The Wilcox model predicts free shear flow spreading rates that are in close agreement with measurements for far wakes, mixing layers, and plane, round, and radial jets, and is thus applicable to wall-bounded flows and free shear flows. [60]

The standard k-ω model is an empirical model based on model transport equations for the turbulence kinetic energy (k) and the specific dissipation rate (ω), which can also be thought of as the ratio of ε to k.

As the k-ω model has been modified over the years, production terms have been added to both the k and ω equations, which have improved the accuracy of the model for predicting free shear flows.

(b) **Shear-stress transport (SST) k-ω model**

The shear-stress transport (SST) k-ω model was developed by Menter to effectively blend the robust and accurate formulation of the k-ω model in the near-wall region with the free-stream independence of the k-ε model in the far-field. To achieve this, the k-ε model is converted into a k-ω formulation. The SST k-ω model is similar to the standard k-ω model, but includes the following refinements:

i. The standard k-ω model and the transformed k-ε model are both multiplied by a blending function and both models are added together. The blending function is designed to be one in the near-wall region, which activates the standard k-ω model, and zero away from the surface, which activates the transformed k-ε model.

ii. The SST model incorporates a damped cross-diffusion derivative term in the ω equation.

iii. The definition of the turbulent viscosity is modified to account for the transport of the turbulent shear stress.

iv. The modelling constants are different.

These features make the SST k-ω model more accurate and reliable for a wider class of flows (e.g., adverse pressure gradient flows, airfoils, transonic shock waves) than the standard k-ω model.

4. **Transition k-kl-ω model**

The k-kl-ω transition model is used to predict boundary layer development and calculate transition onset. This model can be used to effectively address the transition of the boundary layer from a laminar to a turbulent regime.

5. **Transition SST model**

The transition SST model is based on the coupling of the SST $k - \omega$ transport equations with two other transport equations, one for the intermittency and one for the transition onset criteria, in terms of momentum-thickness Reynolds number.

6. v^2- f **model (add-on)**

The v^2- f model is similar to the standard k- ε model but incorporates near-wall turbulence anisotropy and non-local pressure-strain effects. A limitation of the v^2- f model is that it cannot be used to solve Eulerian multiphase problems, whereas the k- ε model is typically used in such applications. [60]

The distinguishing feature of the v^2- f model is its use of the velocity scale, $\overline{v^2}$, instead of the turbulent kinetic energy, k, for evaluating the eddy viscosity. [60]

7. **Reynolds stress models (RSM)**

The Reynolds stress model (RSM) is the most elaborate type of turbulence model that ANSYS FLUENT provides. Abandoning the isotropic eddy-viscosity hypothesis, the RSM closes the Reynolds-averaged Navier-Stokes equations by solving transport equations for the Reynolds stresses, together with an equation for the dissipation rate. This means that five additional transport equations are required in 2D flows, in comparison to seven additional transport equations solved in 3D. [60]

Since the RSM accounts for the effects of streamline curvature, swirl, rotation, and rapid changes in strain rate in a more rigorous manner than one-equation and two-equation models, it has greater potential to give accurate predictions for complex flows. However, the fidelity of RSM predictions is still limited by the closure assumptions employed to model various terms in the exact transport equations for the Reynolds stresses. The modelling of the pressure-strain and dissipation-rate terms is particularly challenging and often considered to be responsible for compromising the accuracy of RSM predictions. [60]

The RSM might not always yield results that are clearly superior to the simpler models in all classes of flows to warrant the additional computational expense. However, the use of the RSM is a must when the flow features of interest are the result of anisotropy in the Reynolds stresses. Among the examples is cyclone flows, highly swirling flows in combustors, rotating flow passages, and the stress-induced secondary flows in ducts. [60]

8. **Detached eddy simulation (DES) model**

In the DES approach, the unsteady RANS models are employed in the boundary layer, while the LES treatment is applied to the separated regions. The LES region is normally associated with the core turbulent region where large unsteady turbulence scales play a dominant role. In this region, the DES models recover LES-like subgrid models. In the near-wall region, the respective RANS models are recovered. [60]

DES models have been specifically designed to address high Reynolds number wall-bounded flows, where the cost of a near-wall resolving Large Eddy Simulation would be prohibitive. The difference with the LES model is that it relies only on the required resolution in the boundary layers. The application of DES, however, may still require significant CPU resources and therefore, as a general guideline, it is recommended that the conventional turbulence models employing the Reynolds-averaged approach be used for practical calculations. [60]

The DES models often referred to as the hybrid LES/RANS models combine RANS modelling with LES for applications such as high-Re external aerodynamics simulations.

9. **Large eddy simulation (LES) model**

Turbulent flows are characterized by eddies with a wide range of length and time scales. The largest eddies are typically comparable in size to the characteristic length of the mean flow. The smallest scales are responsible for the dissipation of turbulence kinetic energy. [60]

It is possible, in theory, to directly resolve the whole spectrum of turbulent scales using an approach known as direct numerical simulation (DNS). No modelling is required in DNS. However, DNS is not feasible for practical engineering problems involving high Reynolds number flows. The cost required for DNS to resolve the entire range of scales is proportional to $\mathrm{Re}_t^{3/4}$, where Re_t is the turbulent Reynolds number. Clearly, for high Reynolds numbers, the cost becomes prohibitive. [60]
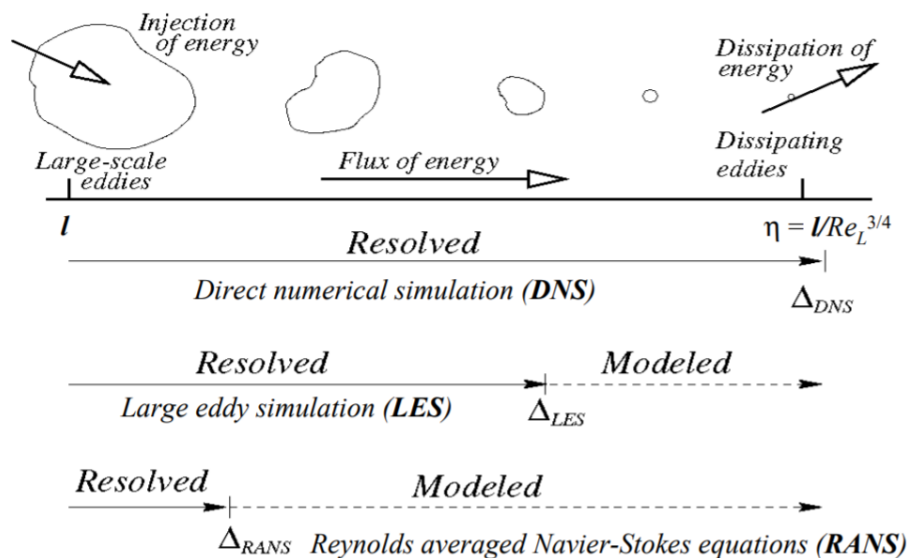

Figure 4.1: Methods To Simulate Turbulent Flow [80]

In LES, large eddies are resolved directly, while small eddies are modelled. Large-eddy simulation (LES) thus falls between DNS and RANS in terms of the fraction of the resolved scales (figure 4.1).

The rationale behind LES can be summarized as follows:

(a) Momentum, mass, energy, and other passive scalars are transported mostly by large eddies.

(b) Large eddies are more problem-dependent. They are dictated by the geometries and boundary conditions of the flow involved.

(c) Small eddies are less dependent on the geometry, tend to be more isotropic, and are consequently more universal.

(d) The chance of finding a universal turbulence model is much higher for small eddies.

Resolving only the large eddies allows one to use much coarser mesh and larger times-step sizes in LES than in DNS. However, LES still requires substantially finer meshes than those typically used for RANS calculations. In addition, LES has to be run for a sufficiently long flow-time to obtain stable statistics of the flow being modelled. As a result, the computational cost involved with LES is normally orders of magnitudes higher than that for steady RANS calculations in terms of memory (RAM) and CPU time. Therefore, high-performance computing (e.g., parallel computing) is a necessity for LES, especially for industrial applications. [60]

4.1.3 Regimes of turbulent combustion

In order to derive models for turbulent combustion, a physical approach is required. This approach is based on the comparison of the various time scales present in turbulent combustion. The Damkohler number is very important because it compares the turbulent (τ_t) with the chemical (τ_c) time scales, through:

$$Da = \frac{\tau_t}{\tau_c} \quad (4.7)$$

When the Damkohler number is very large ($Da \gg 1$), the flame front is thin and its inner structure is not affected by turbulence, which at most can wrinkle the flame surface. [81] This occurs when the Kolmogorov scales, which are the smallest turbulence scales, have a τ_t greater than τ_c, which means that the turbulent motions are too slow to affect the flame structure.

4.1.4   Choosing a Turbulence model

It is an unfortunate fact that no single turbulence model is universally accepted as being superior for all classes of problems. The choice of turbulence model will depend on factors such as the physics incorporated in the flow, the approved practice for a specific class of problem, the level of accuracy needed, the available computational resources, and the amount of time available for the simulation. To make the most suitable choice of model for the application is required to understand the capabilities and limitations of the various options.

The purpose of this section is to give an overview of issues related to the turbulence models provided in ANSYS FLUENT. The computational effort and cost in terms of CPU time and memory of the individual models are discussed. While it is impossible to state categorically which model is best for a specific application, general guidelines are presented to help to choose the suitable turbulence model for the flow that will be model.

For the present study, the selected model was the RSM due to the following characteristics:

- First, accounts for the effects of streamline curvature, swirl, rotation, and rapid changes in strain rate in a more rigorous manner than one-equation and two-equation models.

- Avoids isotropic eddy viscosity assumption.

- Suitable for complex 3D flows with strong streamline curvature, strong swirl/rotation (e.g. curved duct, rotating flow passages, swirl combustors with very large inlet swirl, cyclones).

- And has greater potential to give accurate predictions for complex flows.

4.2   Test Cases

The Simulations have been performed using the results of Tests 5, that has been mentioned in the previous chapter.

4.2.1   Geometry

The CAD software was chosen for the design of the DHX-4 was CATIA V5 R21. This choice was mainly because the author was more familiar with this software and also because it offers a wide variety of tools to enable all sorts of drafts.

To obtain the 3D model the author use a blueprint of the DHX-4 configuration that is presented in [73]. The geometry chosen as the fluid flow domain is nevertheless the inside boundary of the combustion chamber, from the injector plate to the exit section of the nozzle, including the fuel grain internal border. While the other geometrical characteristics are invariant during the fire, the fuel grain thickness reduces over time, therefore the port area

increases. Figure 4.2 is a representation of a model used for the simulations, in particular for Test 5 at burn time 1.5 seconds. The frontal part of the rocket is the pre-combustion chamber, where the injector orifices are located. The middle part is the burning area of the fuel grain while the rear part is the convergent-divergent nozzle. The dimensioned section of the model of Test 5 can be seen in Appendix A. The construction is axisymmetric so the sketch is simply rotated $360°$ degrees to obtain the 3D figure.
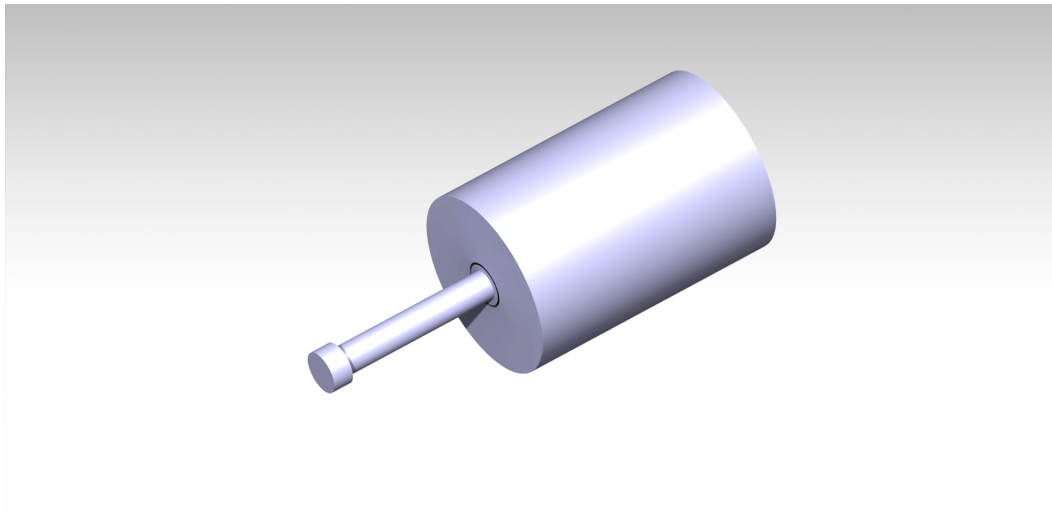
Figure 4.2: Geometry Model

4.2.2   Generation of the Numerical Mesh

The most important aspect of a CFD simulation is the generation of the model mesh. Mesh generation is one of the most time-consuming aspects of computational solutions of problems involving partial differential equations. The aim of this mesh is to provide a distribution of points where the solution will be calculated, and the finer the grid better will be the resolution of all the flow features. However, it is important to note that the finer the grid, or in order words, increasing the number of elements will inevitably lead to an increase in computational cost (CPU) and time. Thus it is important to study all of the important aspects of the mesh, such as the grid spacing ratio and the cells aspect ratio, in order to achieve the best comprise between mesh size, computational cost and solution accuracy. A resume of a meshing best practice is shown in the figure 4.3.
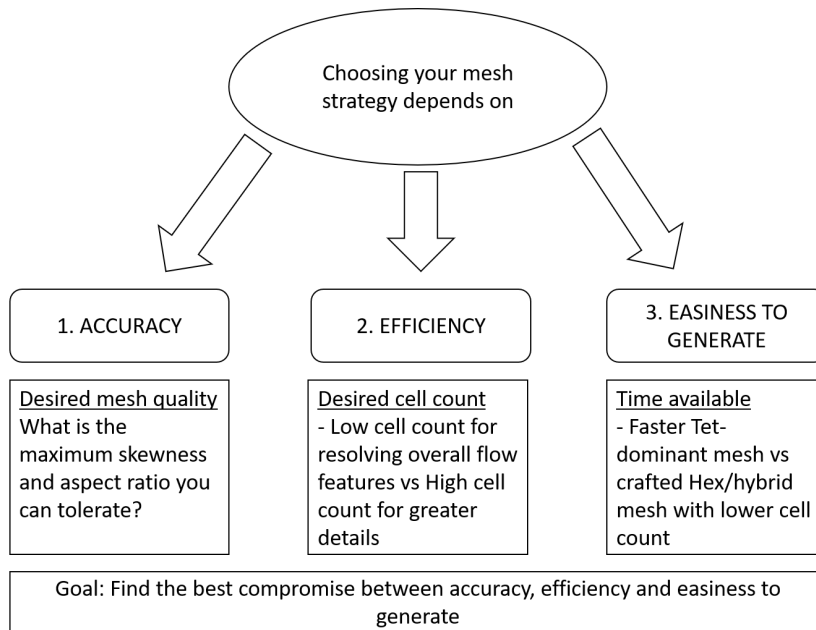
Figure 4.3: Meshing Best Practice Guidelines

A good quality mesh means that:

- Mesh quality criteria are within correct range: - Orthogonal quality, Skewness,...

- Mesh is valid for studied physics: - Boundary layer,...

- Solution is grid-independent

- Important geometric details are well captured

Bad quality mesh can cause:

- Convergence difficulties

- Bad physics description

- Diffuse solution

4.2.2.1   Mesh Quality Metrics

Orthogonal Quality

- For a *cell* it is the minimum of:

$$\frac{A_i f_i}{|\overrightarrow{A_i}||\overrightarrow{f_i}|} \qquad \frac{A_i c_i}{|\overrightarrow{A_i}||\overrightarrow{c_i}|}$$
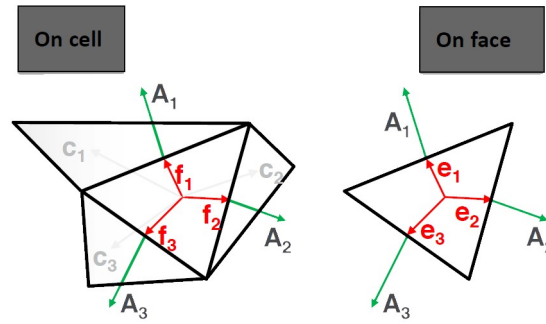
Figure 4.4: Representation of the f_i and e_i. [82]

computed for each face i

For the $face$ it is computed as the minimum of $\frac{A_i e_i}{|\vec{A_i}||\vec{e_i}|}$ computed for each edge I.

Where A_i is the face normal vector and f_i is a vector from the centroid of the cell to the centroid of that face, and c_i is a vector from the centroid of the cell to the centroid of the adjacent cell, where e_i is the vector from the centroid of the face to the centroid of the edge.

At boundaries and internal walls, c_i is ignored in the computations of Orthogonal Quality.

Skewness

Two methods for determining skewness:

1. Equilateral Volume deviation:

$$Skewness = \frac{optimalcellsize - cellsize}{optimalcellsize}$$

   Applies only for triangles and tetrahedrons

2. Normalized Angle deviation:

$$Skewness = max\left[\frac{\theta_{max} - \theta_e}{180 - \theta_e}, \frac{\theta_e - \theta_{min}}{\theta_e}\right]$$

Where θ_e is the equiangular face/cell (60 for tets and tris, and 90 for quads and hexas)

   – Applies to all cell and face shapes

   – Used for hexa, prisms and pyramids
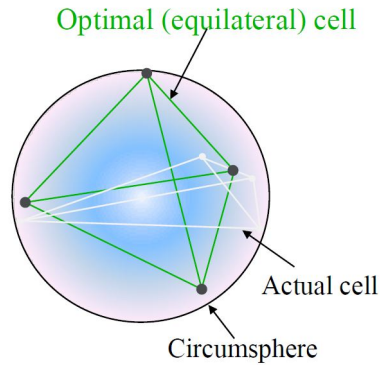
(a) Equilateral Volume deviation. [82]

(b) Normalized Angle deviation. [82]

The mesh generation was performed using ANSYS. The author started trying to use HELYX-OS, which is based on SnappyHex Mesh. HELYX-OS had many advantages over other mesh generation software's. Advantages include a quicker mesh generation time and user-friendly software which enables the user to better refine any given part of the mesh. HELYX-OS is an OpenFoam program, and as such is not available for Windows in the free version. Thus, Linux is the operating system in which HELYX-OS can be freely handled, and as such, another computer, with 8GB of RAM, provided by Dr Francisco Brójo was used for this phase. However, HELYX-OS proved not to be the right software for this work, only because of the fact that for this work it will need to create two contact regions between the fuel zone and the injector zone and the fuel zone and the nozzle zone. For this reason, the author used ANSYS ICEM CFD to generate the mesh. One of the advantages over HELYX-OS is the possibility to import the .CATPart[1] directly to ANSYS without needing to convert the CAD model to .STL file format every time a modification in geometry was done.

After the .CATPart file has imported to Ansys we have everything to begin the mesh generation setup. Firstly was select in the Geometry section the option Fluid in the Fluid/Solid area under the Material subsection. The next step is to choose the right configurations in the Mesh section. The full configuration is shown in the form of table 4.1.

---

[1]Part file created by CATIA V5, a 3D CAD manufacturing application; stores a part model, including the three-dimensional geometry and structure data; can be combined with other parts into a .CATPRODUCT assembly file.

Table 4.1: Mesh configuration.

Defaults	
Physics Preference	CFD
Solver Preference	Fluent
Element Order	Program Controlled
Element Size	0.9 mm
Export Format	Standart
Export Preview Surface	No
Sizing	
Use Adaptive Sizing	No
Growth Rate	1.15
Max Size	12 mm
Mesh Defeaturing	Yes
Defeature Size	Default ($4.5e - 003$ mm)
Capture Curvature	Yes
Curvature Min Size	Default ($9.e - 003$ mm)
Curvature Normal Angle	10º
Capture Proximity	Yes
Proximity Min Size	Default ($9.e - 003$ mm)
Num Cells Across Gap	Default (3)
Proximity Size Function Sources	Faces and Edges
Quality	
Check Mesh Quality	Yes, Errors
Target Skewness	0.75
Smoothing	High
Inflation	
Use Automatic Inflation	None
Assembly Meshing	
Method	None
Advanced	
Number of CPUs for Parallel Part Meshing	8
Triangle Surface Mesher	Program Controlled
Topology Checking	Yes
Pinch Tolerance	Default ($6.3e - 003$ mm)
Generate Pinch on Refresh	No
Statistics	
Nodes	11403928
Elements	5654460

For the fuel and injector faces, it was necessary to create an inflation layer because is a good practice to have a minimum of 5 layers on the inlets. For this option is need to get more caution because the resultant mesh may be of poor quality, especially in high aspect ratio cells. For the inflation layer, the following options have been selected.

Table 4.2: Inflation configuration.

Scope	
Scoping Method	Geometry Selection
Geometry	1 Body (Pre-chamber / Combustion Chamber)
Definition	
Supressed	No
Boundary Scoping Method	Geometry Selection
Boundary Scoping Method	8 Faces / 1 Face (Injector's / Fuel)
Inflation Option	Smothing Transition
Transition Ratio	Default (0.272)
Maximum Layers	5
Growth Ratio	1.05
Inflation Algorithm	Pre

In the outlet zone has been create a local body sizing with the option of Body of Influence in the zone where the flow will become supersonic. The options used are shown in the table 4.3 and the geometry of the body of influence (in green) can be seen on the figure 4.13.

Table 4.3: Body sizing configuration.

Scope	
Scoping Method	Geometry Selection
Geometry	1 Body
Definition	
Suppressed	No
Type	Body of Influence
Body of Influence	1 Body
Element Size	2.5 mm
Advanced	
Growth Ratio	1.15

The fluid volume has been discretized with tetrahedron cells in the injector and nozzle zones. The choice of the element size is related to the time for convergence and the quality of the results due to the curvature of the nozzle and the fact of the injector inlets in the injector zone. For the fuel zone, the volume has been discretized with hexahedrons which allow for more accurate results because the direction of the flow is well known. Then Quad/Hex aligned with the flow are more accurate than Tri with the same interval size. A 5.7 million elements grid has been adopted, refined in the volume sector corresponding to the fuel grain, where the chemical reaction takes place. The combustion is highly sensitive to the solidity of the mesh. Simulations run on a coarse mesh may never reach convergence, and the pressure and temperature are often underestimated. The final mesh is shown in figure 4.6 and the Metric Graph of some of the most important aspects of the mesh is shown in figure 4.7. Using the Mesh Metric Graph that displays Mesh Metrics graph for the element quality distribution, different element types are plotted with different colour bars and was used to help locate poor quality elements.
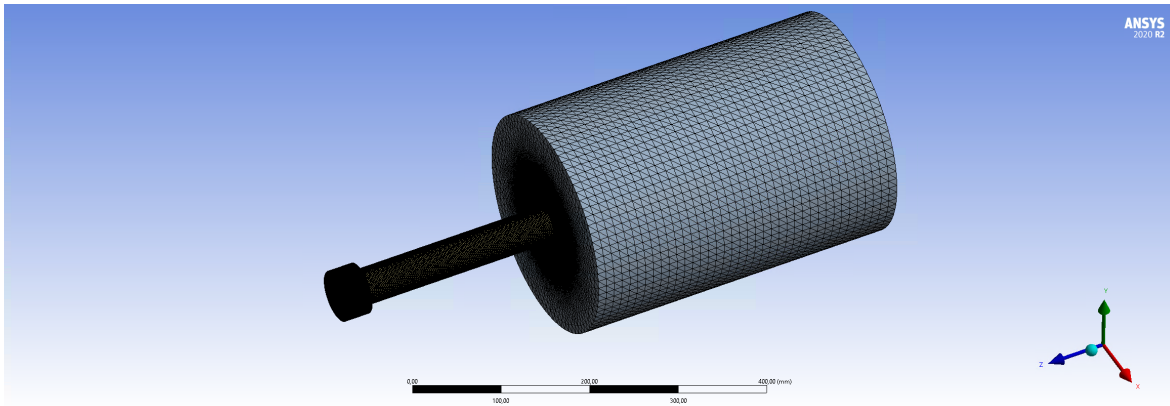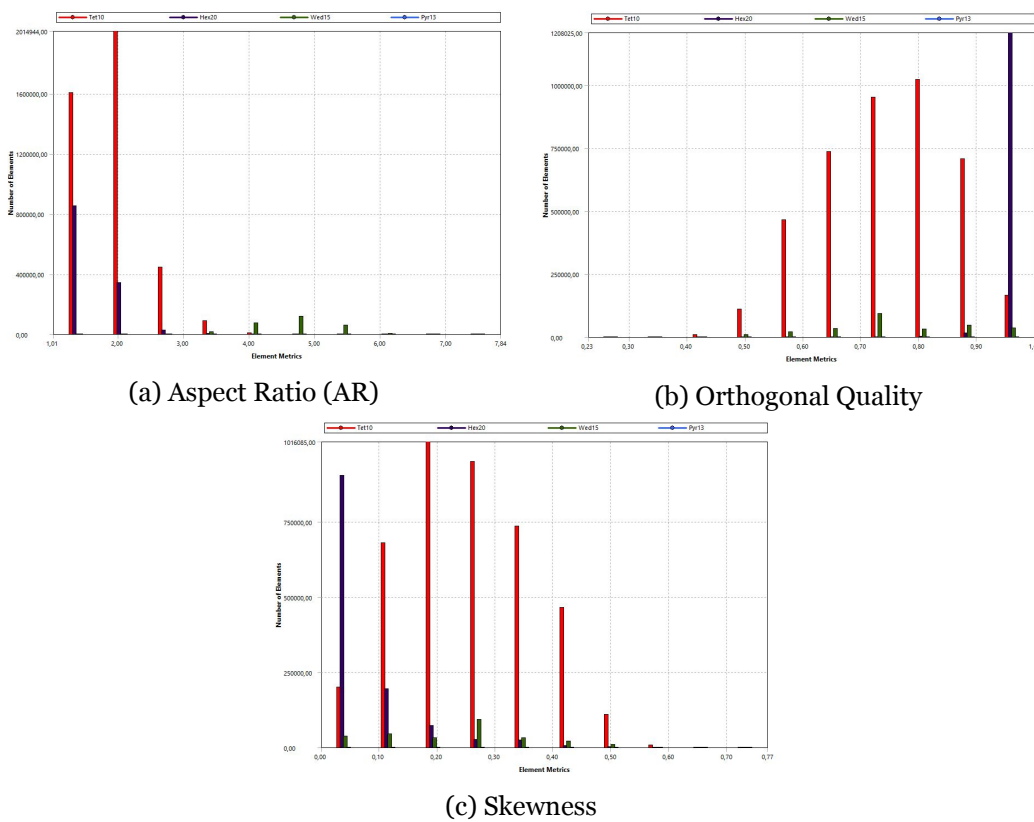
Figure 4.6: Mesh

(a) Aspect Ratio (AR)

(b) Orthogonal Quality

(c) Skewness

Figure 4.7: Mesh Metric

4.3 Problem Setup

Once the mesh is ready, the problem setup can now begin. ANSYS Fluent 20.2 is the software used to perform this simulation.

When initiating ANSYS Fluent, a window named Fluent Launcher is displayed. Here it is necessary to ensure that $3D$ dimension is checked, and it is also necessary to choose whether the calculation will be performed in single or double precision. If double precision is enabled,

the solution will be slower but the results will be more accurate. So, the double-precision has been selected. Still, in the same window, it is possible to run the simulation with single or parallel processors, in which the latter reduces significantly the computational time. Thus, the parallel was chosen and the number of processes was set to 8, which is the maximum number of processors available in the computer.

Once ANSYS Fluent is launched, the quality of the mesh must be checked as this greatly affects the solution's convergence and results. It is then first necessary to check if there are any negative cell values, which was not the case. Following this, reporting the mesh quality will display in the command window some important aspects regarding mesh quality; these are the aspect ratio, orthogonal quality and mesh skewness. Some of the mesh quality recommendations are low Orthogonal quality or high skewness values are not recommended. Generally, try to keep minimum orthogonal quality > 0.1, or maximum skewness < 0.95. However, these values may be different depending on the physics and the location of the cell.

Excellent	Very good	Good	Acceptable	Bad	Unacceptable
0-0.25	0.25-0.50	0.50-0.80	0.80-0.94	0.95-0.97	0.98-1.00
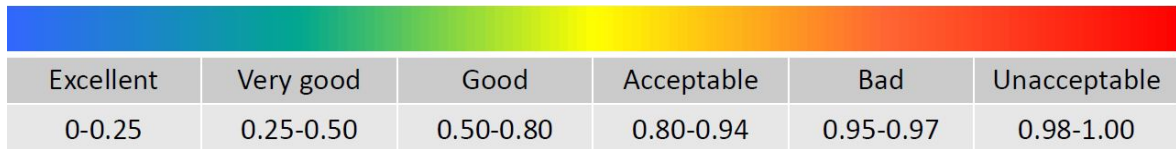
Figure 4.8: Skewness mesh metrics spectrum. [82]

Unacceptable	Bad	Acceptable	Good	Very good	Excellent
0-0.001	0.001-0.14	0.15-0.20	0.20-0.69	0.70-0.95	0.95-1.00
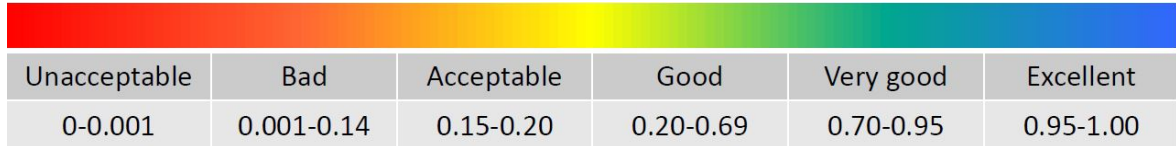
Figure 4.9: Orthogonal Quality mesh metrics spectrum. [82]

A section plane has been created to view the elements inside of the body mesh. This allow for a better understand the mesh interior composition. The result was shown in figure 4.10.
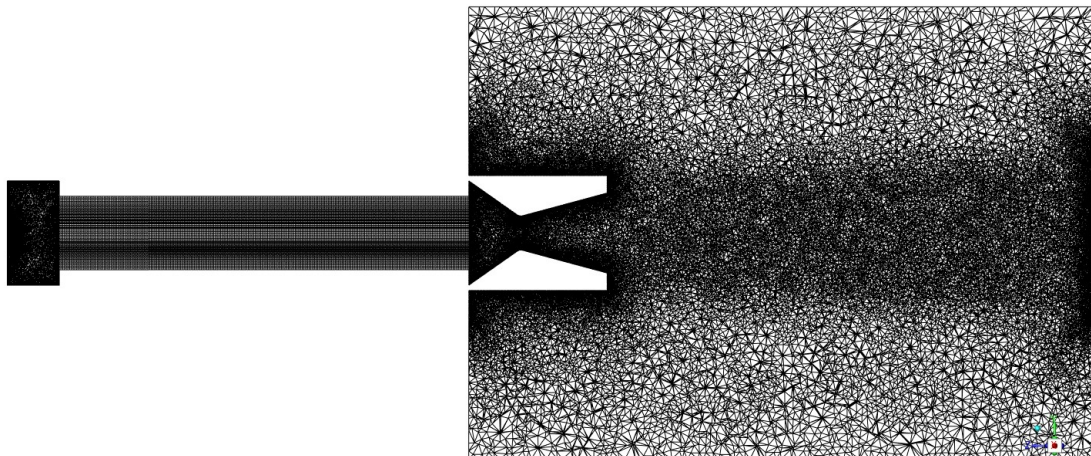

Figure 4.10: Cut section of the mesh

4.3.1 Models

ANSYS Fluent is a very versatile code, and as so there are a variety of models that can be chosen, depending on the necessity of the simulation. For this setup, five models are used:

1. Energy model - The energy model must be activated as this regards the energy related to the temperature change within the combustion process or heat transfer.

2. Radiation model - The P-1 radiation model was the chosen one, is the simplest case of the more general P-N model, which is based on the expansion of the radiation intensity I into an orthogonal series of spherical harmonics. The biggest advantage is a lower CPU cost. [60]

3. Viscous Model -Through this model, inviscid, laminar and turbulent flows can be studied. As discussed in section Turbulent flow analysis, the chosen model was the RSM with all its constants maintained at the default values.

4. Species model - This model allows ANSYS Fluent to model the mixing, transport and combustion of chemical species. Due to the importance of this model for this work, the inputs will be explained in detail.

   First-off, non-premixed combustion is selected as this describes the combustor system in the study. Regarding the PDF table creation, inlet diffusion is selected as this includes the diffusion flux of species at the flow inlet. In the chemistry tab, chemical equilibrium is selected and as for the energy treatment, non-adiabatic is enabled.

   Operating pressure is less significant for higher-Mach-number compressible flows. The pressure changes in such flows are much larger than those in low-Mach-number compressible flows, so there is no real problem with roundoff error and, therefore, no real need to use gauge pressure. In fact, it is common convention to use absolute pressures in such calculations. Since ANSYS Fluent always uses gauge pressure, the operating pressure was set to zero, making gauge and absolute pressures equivalent. As for the Fuel Stream Rich Flammability limit (FSRFL), a value larger than 10 % of the stoichiometric mixture fraction can be used. [60] The stoichiometric ratio of Paraffin is difficult to calculate because is composed of several hydrocarbons/species. Thus NASA's Chemical Equilibrium with Application (CEA) was used for this purpose. CEA allows the user to introduce each of the species, as well as their concentration in the fuel and then calculates several user-defined output thermodynamic properties, which include the stoichiometric ratio. The stoichiometric ratio obtained with CEA is 1.26. The last thing to check in the chemistry tab is to ensure that the thermo.db file, in which the thermodynamic properties of the fuel species will be introduced, is correctly chosen.

   The specification of the fuel species name and concentration is done in the boundary tab. It is important to check if the species that are intended to introduce are presented

by their thermodynamic properties, in the thermo.db file[2]. For the present study the paraffin ($nC_{28}H_{58}$) had to be introduced.

It is important to note that the introduction of this thermodynamic data in the thermo.db file has to agree with CHEMKIN format, otherwise ANSYS Fluent will not add the new species to the fuel. Still in the boundary tab, the oxidizer species and concentration, as well as the temperatures of the oxidizer and the fuel have to be introduced. The oxidizer used has the (N_2O). As for the fuel temperature, this gives respect to the flash-point, the value is 700 K. The oxidizer temperature was 300 K. After the previous steps being performed, the last step in the species model is the calculation of the PDF table in the Table tab. Here all of the table default parameters were maintained, and the Automatic Grid Refinement was enabled. Finally, the PDF table can be calculated, and as a result, the number of species created can be checked in Materials. The $3D$ look-up tables are reviewed on a slice-by-slice basis has can been seen in figure 4.11. By default, the slice selected is that corresponding to the adiabatic enthalpy values. You can also select other slices of constant enthalpy for display. The maximum and minimum values for mean temperature and the corresponding mean mixture fraction will also be reported in the console. The maximum mean temperature is reported as 2888.18 K at a mean mixture fraction of 0.2.
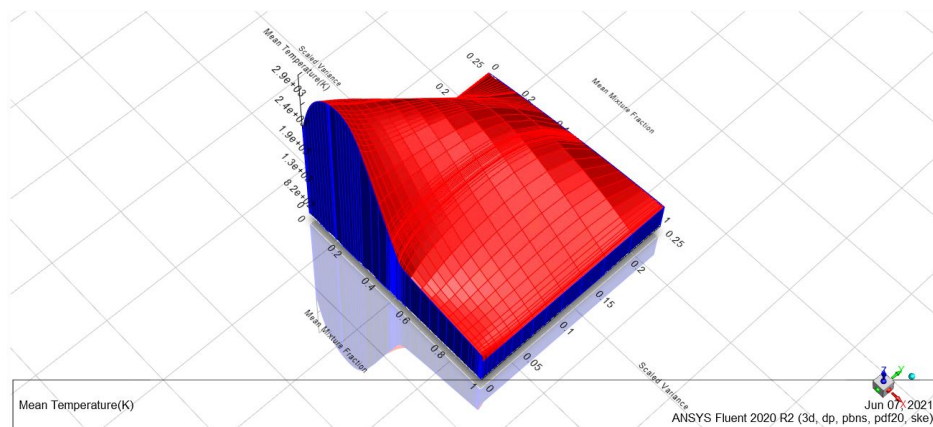
Figure 4.11: 3D Plot of Look-Up Table for Temperature

4.3.2   Boundary Conditions

The most important part of this entire work set-up of the boundary conditions, as this greatly affects convergence and results. Thus, all of the input values for the boundary conditions are explained in this section.

Three types of boundary conditions were applied; mass flow inlet's, pressure-outlet and walls. In the thermal tab, the stream temperature has to be introduced accordingly these being oxidizer inlets or fuel inlets. In the species tab, the Mean Mixture Fraction has to be

---

[2]This can be done by checking directly in the thermo.db file or by clicking List Available Species, which will display the species that are present in the command window.

set to unity, when injecting fuel (fuel injectors) and the Pollutant NO mass Fraction and the Mixture Fraction Variance were maintained. The wall boundaries have remained at default settings and the exit gauge pressure was set to 101325 Pa as this considers the system pressure at the exit to be the ambient pressure. In the appendix E is show a table with a resume of the boundary conditions used.

4.3.2.1 Oxidizer Injection

The oxidizer injection has been define in Fluent with a mass flow inlet. The values of the mass flow rate has been calculated in Gelain thesis [73].

The parameters calculated by Gealin [73] have listed in table 4.4.

Table 4.4: Injection Parameters [73]

	Test 5
Time instant [s]	1.5
Total Mass Flow Rate [g/s]	377.2021
Vapor Quality [-]	0.1866
Liquid Mass Flow Rate [g/s]	306.8162
Liquid Mass Flow Rate per Injector [g/s]	43.8309
Vapor Mass Flow Rate [g/s]	70.3859
Vapor Mass Flow Rate per Injector [g/s]	10.0551
Density [kg/m3]	336.0419
Liquid Density [kg/m3]	897.1387
Vapor Density [kg/m3]	90.1821
Temperature [K]	275.0763
Port Radius [mm]	21.5

One modification in the area of the injectors has need to be done because the data used by Gelain has liquid injection and in this thesis it will be neglected the liquid phase and the injection will be done all in the gas phase. This can be done because the N_2O has a evaporation temperature of 298 K and the oxidizer is injected with 300 K. This assumption caused the diameter of the injector's to change to 4 mm.

The DHX-4 Phoenix motor injectors are not perpendicular to the plate, to imprint a swirling motion to the oxidizer flow. The motor studied in this thesis has a swirl angle of 15 degrees.

Before setting the boundary condition, one has to ensure that the 'axial' direction as referred to in the boundary condition is correctly setup. The axial direction of your system must be equal to the axial direction as defined by the solver. For this case the axial direction was Z (i.e. $X = 0$, $Y = 0$ and $Z = 1$). Once the axial direction is defined, we can go to the second step and define the boundary condition, for Test 5 the injection configuration is shown in appendix B. In order to imprint the swirl motion, it was necessary to select for the Coordinate System the Local Cylindrical (Radial, Tangential, Axial) (see figure 4.12).
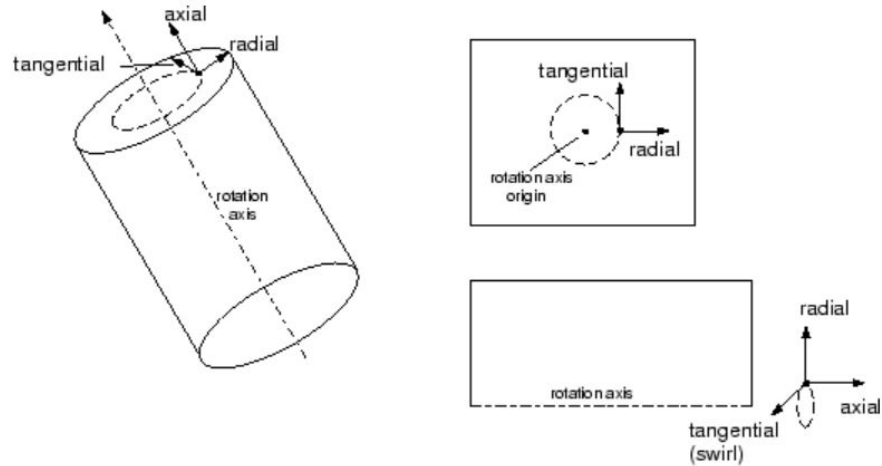
Figure 4.12: Cylindrical Velocity Components in 3D, 2D, and Axisymmetric Domains. [60]

Was assumed that the radial flow direction is 0. If the angle of swirl is 15 degrees, we have an axial component $V_x = V \times cos(15)$ and a tangential component $V_\theta = V \times sin(15)$. Hence, the input should be the following:

Direction Specification Method	Direction Vector
Coordinate System	Local Cylindrical (Radial, Tangential, Axial)
Radial- Component of Flow Direction	0
Tangential-Component of Flow Direction	0.2588
Axial-Component of Flow Direction	0.9659

Axis Origin		Axis Direction	
X (mm)	0	X	0
Y (mm)	0	Y	0
Z (mm)	0	Z	-1

In the Turbulence section, the Specification Method selected was Intensity and Hydraulic Diameter with a Turbulent Intensity of 5% and a Hydraulic Diameter of 4 mm. For the Reynolds-Stress Specification Method, the K or Turbulent Intensity was selected. In the Thermal tab, a Total Temperature of 300 K has been chosen, the other tabs have been left with the defaults values.

4.3.2.2 Fuel Injection

After the ignition, a diffusion flame develops above the fuel grain. The heat of the flame decomposes and vaporizes the solid fuel, which mixes with the oxidizer sustaining the combustion. [83] Near the fuel grain, in the boundary layer, this phenomenon takes place. In particular, due to the high heat transfer, the surface of the vaporizing fuel is subjected to pyrolysis. [48] The fuel polymeric chain breaks up into smaller molecules, that enters the combustion chamber in the gas phase. The reagents of the combustion chemical reaction are not the original fuel molecules but a mixture of smaller elements. Karabeyoglu proposed a

theory to model the pyrolysis chemistry of homologous series of normal alkanes, like paraffin waxes, in hybrid rocket motors. The regression rate predicted by his theory matched test data with reasonable accuracy. [20] In particular, a normal alkane decomposition abides by the following rule:

$$C_nH_{2n+2} = H_2 + \frac{n}{2}C_2H_4$$
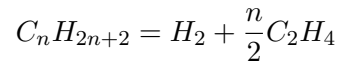
The alkane is decomposed into a mixture of Hydrogen and Ethylene. The paraffin wax used for the experiments is the *Shell Sarawax SX70*. From the datasheet given by the supplier, the properties of the fuel are approximately the same as *Hentriacontane*, $C_{31}H_{64}$, so the following decomposition is adopted [73]:

$$C_{31}H_{64} = H_2 + 15.5C_2H_4$$
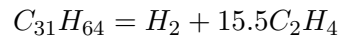
As suggested by Karabeyoglu, this methodology could be applied to normal alcohols or normal acids. Using this theory as a baseline, a similar approach is used for Sorbitol, $C_6H_{14}O_6$, which is a sugar alcohol. Pyrolysis decomposes Sorbitol into Hexane, Carbon Dioxide and Water. [84] Unfortunately, an exact stoichiometric rule couldn't be found in literature, and an arbitrary choice had to be made to fit the theory of Karabeyoglu. The combination closest to the results for the actual Sorbitol - Nitrous Oxide reaction has been adopted [73]:

$$19C_6H_{14}O_6 = 13C_6H_{14} + 36CO_2 + 42H_2O$$
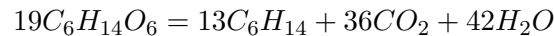
The species obtained from the decomposition are then injected into the combustion chamber as a gas mixture. The mass fractions of the components are listed in table 4.5.

Table 4.5: Fuel Mass Fractions

	Sorbitol 100%	Paraffin 100%	S. 80% P. 20%
C_6H_14	0.32331	-	0.25865
CO_2	0.45807	-	0.36645
H_2O	0.21862	-	0.17490
C_2H_4	-	0.977	0.19940
H_2	-	0.003	0.0006

4.3.2.3 Combustion
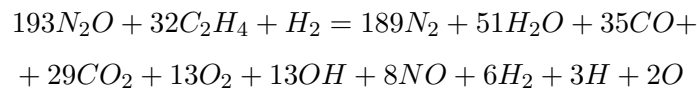
Chemical Reaction

The impact of the chemical reaction on the results is related to the number of species used: the higher the number, the closer to the truth is the simulation. Using the software CEA, which allows obtaining the equilibrium composition, the reaction products and the adiabatic flame temperature can be determined.

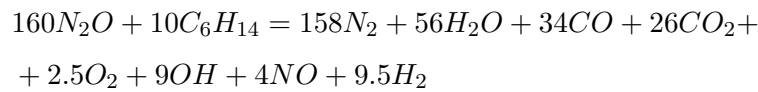From the mass fraction of the products, the stoichiometric coefficients of the reaction have

been calculated, while the coefficients of the products are set to the stoichiometric O/F ratio. A trade-off has to be made between the number of species and the memory requirements, so the products with a mass fraction magnitude lower than 10^{-3} have been neglected.

The resulting balanced equations are:

- **Paraffin:**

$$193N_2O + 32C_2H_4 + H_2 = 189N_2 + 51H_2O + 35CO +$$
$$+ 29CO_2 + 13O_2 + 13OH + 8NO + 6H_2 + 3H + 2O$$

- **Sorbitol:**

$$160N_2O + 10C_6H_{14} = 158N_2 + 56H_2O + 34CO + 26CO_2 +$$
$$+ 2.5O_2 + 9OH + 4NO + 9.5H_2$$

If the number of chemical species used is too low, the flame temperature of the reaction would become higher than the real flame adiabatic temperature, thus creating an error in the simulation. A similar reaction was used for paraffin wax by Lazzarin [85], even though the paraffin used in her research is *Pentacontane*, $C_{50}H_{102}$.

The chemical reactions have to be calculated and balanced since these are inputs required by the CFD solver to simulate the combustion process inside the chamber. For simplicity's sake, the combustion is single-phase, therefore the elements react only in the gas phase: liquid Nitrous Oxide has to evaporate before it can react with the gaseous fuel injected from the walls. The evaporation greatly influences the structure of the flame inside the combustion chamber, highlighting again why accurate secondary break-up and evaporation models have to be chosen.

4.3.2.4 Nozzle and Outlet

The nozzle function is to accelerate and eject the hot gases from the combustion chamber, creating thrust. In the CFD simulation, the boundary condition is set to an pressure-outlet type with a pressure of 101325 Pa and an Pressure Profile Multiplier of 1. Figure 4.13 represents the nozzle and the outlet region, with a cut section in the plane YZ, modelled in CATIA V5.
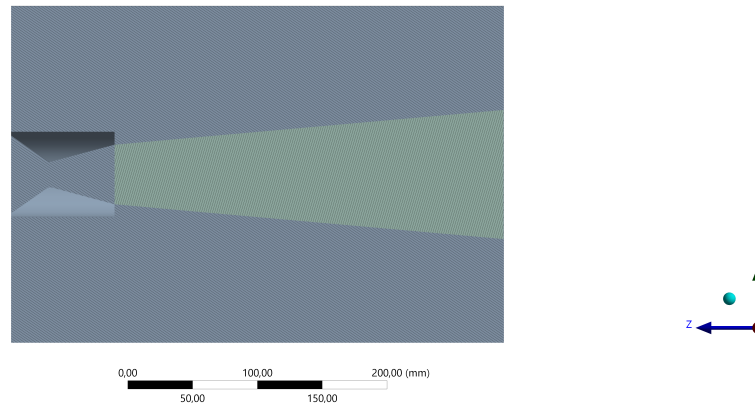
Figure
07/06/2021 16:30

Figure 4.13: Nozzle and Outlet

4.3.3 Dynamic Mesh

In the dynamic mesh section, it has been selected in the Mesh Methods the Smoothing, Layering and Remeshing options.

When smoothing is used to adjust the mesh of a zone with a moving and/or deforming boundary, the interior nodes of the mesh move, but the number of nodes and their connectivity does not change. In this way, the interior nodes "absorb" the movement of the boundary.

In the Smoothing settings, the diffusion methods has been checked with the boundary-distance selected for the diffusion function with a diffusion parameter of 0 which allows performing a diffusion uniformly (a diffusion parameter of 1 will perform a diffusion closer to the moving wall and a value of 2 a diffusion far from the moving wall).

In prismatic (hexahedral and/or wedge) mesh zones, the dynamic layering can be used to add or remove layers of cells adjacent to a moving boundary, based on the height of the layer adjacent to the moving surface. The dynamic mesh model in ANSYS Fluent allows you to specify an ideal layer height on each moving boundary.

You can control how a cell layer is split by specifying either Height Based or Ratio Based under Options. Note that for Height Based, the height of the cells in a particular new layer will be constant, but you can choose to have this height vary from layer to layer as a function of time or crank angle when you specify the Cell Height in the Dynamic Mesh Zones dialogue

box.

The Split Factor and Collapse Factor are the factors that determine when a layer of cells (hexahedra or wedges in $3D$, or quadrilaterals in $2D$) that is next to a moving boundary is split or merged with the adjacent cell layer, respectively.

For the Layering settings, it has been chosen the Height Based option with 0.4 for the Split factor and 0.2 for the Collapse factor.

On zones with a triangular or tetrahedral mesh, the spring-based smoothing method is normally used. When the boundary displacement is large compared to the local cell sizes, the cell quality can deteriorate or the cells can become degenerate. This will invalidate the mesh (for example, result in negative cell volumes) and consequently, will lead to convergence problems when the solution is updated to the next time step. If the local new cells satisfy the skewness criterion, the mesh is updated by a new cell; otherwise, the new cells are discarded

The remeshing methods are suitable for particular kinds of cell types:

- The local cell remeshing method only affects triangular and tetrahedral cell types in the mesh (that is, in mixed cell zones the non-triangular/tetrahedral cells are skipped).

- The local face remeshing method is available in $3D$ only and can remesh tetrahedral cells and wedge cells in boundary layer meshes.

- The zone remeshing method replaces all cell types with triangular tetrahedral cells (in $2D$ and $3D$ domains, respectively), and can remesh and produce wedge cells in $3D$ boundary layer meshes.

- The face region remeshing method is applied to triangular cells in $2D$ and tetrahedral cells in $3D$. In $3D$ domains, the face region remeshing method can also remesh and produce wedge cells in $3D$ boundary layer meshes.

- The CutCell zone remeshing method works for all cell types.

- The $2.5D$ remeshing method only works on hexagonal meshes or wedge cells extruded from triangular surface elements.

In the Remeshing tab for the setting, the local cell and the CutCell zone methods have been selected. With the following parameters:

- Minimum Length Scale (mm) - 0.022046

- Maximum Length Scale (mm) - 1.979056

– Maximum Cell Skewness - 0.75

– Size Remeshing Interval - 0 (that allows performing the remeshing method only when one of the parameters is not met.

After all the parameters have been set it was needed to create the UDF[3] (User-Defined Function) that will allow to make the grid motion and simulate the regression rate of the fuel. For a better understanding of the motion of the fuel boundary it has been created a MATLAB code (see appendix C) that use the nodes of the mesh correspondent to the fuel (this has been done in the FLUENT going to File > Export > Solution Data and select the ASCII for the file type, Node for location, fuel for Surface and X velocity, Y Velocity and Z Velocity in the Quantities). The function of the code is to read the solution data export from the FLUENT organise the data that is needed, calculate the movement for a specified velocity (regression rate), time and step size, then the coordinates of the nodes in which time step is write in a vector and plotted in a $3D$ plot to get a better understanding of the motion. The $3D$ plot of the fuel surface coordinates at each time is shown in figure 4.14.

(a) XY plane view

(b) 3D view
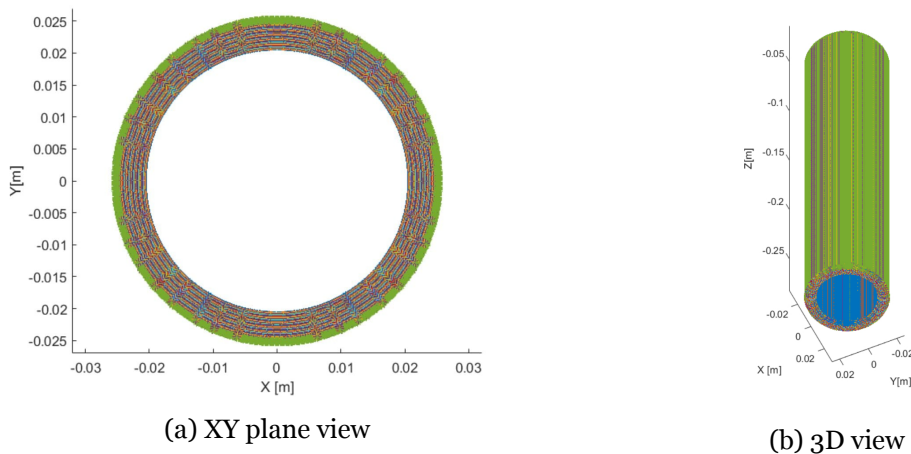
Figure 4.14: Fuel motion (each color represents a time step and the green color is the last one).

Next, the movement has been defined in the MATLAB code the UDF file (appendix D) is written with the same parameters used in the first code. Then the UDF file needs to be compiled. The following procedure has been a maid in Fluent: In Define > User-Defined > Functions > Compiled, in the source files the UDF file is add and the library is built (for this work the library name was regression_rate) and then the library is loaded.

Then in the Dynamic Mesh Zone, it created a User-Defined for the fuel zone, selecting for the Mesh Motion UDF the UDF that has been compiled and in the Meshing Option tab a Cell Height of 0.7 mm has been used (this value correspond to the Height of the cells closer to the

---

[3]A UDF is a function that is programmed and can be dynamically loaded with the ANSYS FLUENT solver to enhance the standard features of the code. UDFs are written in the C programming language using any text editor and the source code file is saved with a .c extension (e.g., myudf.c).

fuel surface in the fuel zone)

Also in the Dynamic Mesh, it has been created an Event that allows change of the zone type of the injectors from inlets to walls, this was necessary because the main valve was shut after 2.7 s of the experimental which correspond to 1.2 s in the simulation.

4.3.4 Solution Methods, Solution Controls and Monitors

4.3.5 Choosing a Solver

So far we have looked at how to setup the flow simulation in FLUENT. By modifying the solver settings you can improve both the rate of convergence of the simulation and the accuracy of the computed result. We should not assume that just because you have 'an answer' that is the 'correct answer'.

The fluxogram in figure 4.15 shows the basic workflow for this simulation.
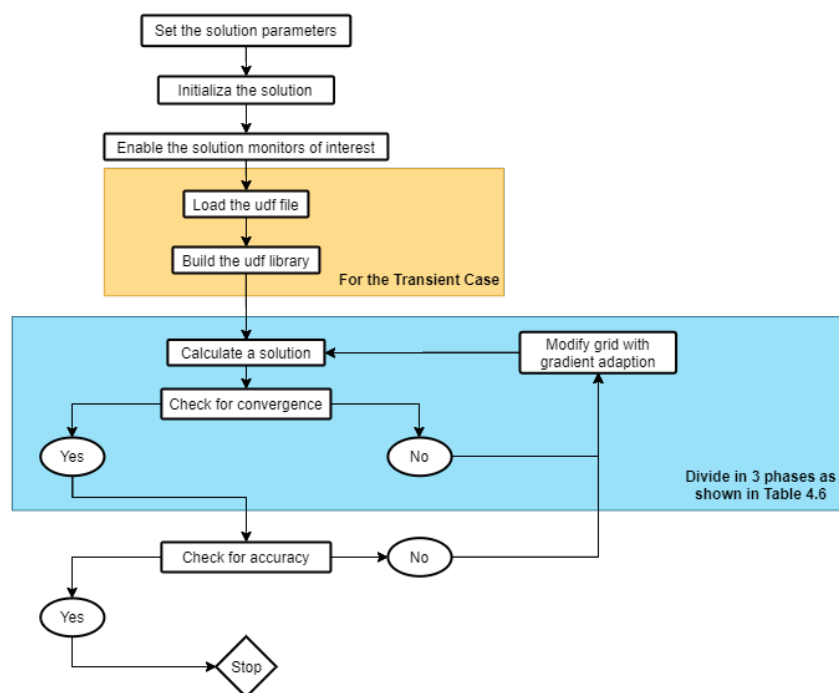
Figure 4.15: Basic workflow. [82]

There are two kinds of solvers available in FLUENT:

- – Pressure-based

- – Density-based
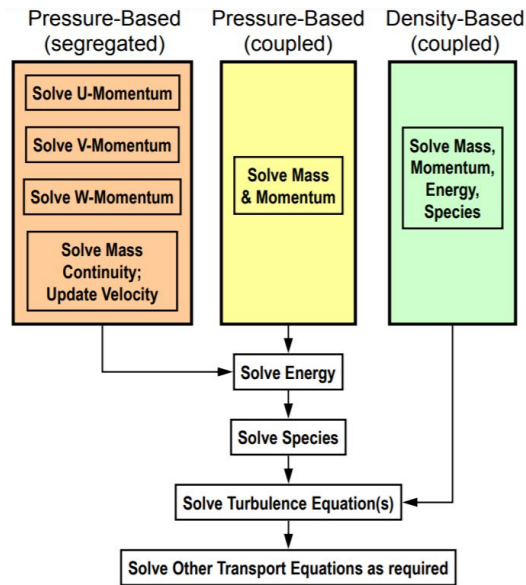
Figure 4.16: Available Solvers. [82]

The selected solver was pressure-based that takes moment and pressure (or pressure correction) as the primary variables. Pressure-velocity coupling algorithms are derived by reformatting the continuity equation. The pressure-based solver is applicable for a wide range of flow regimes from low-speed incompressible flow to high-speed compressible flow. Requires less memory (storage) and allows flexibility in the solution procedure. Allows flexibility in the solution procedure. [82]

4.3.5.1 Discretisation

In FLUENT, solver variables are stored at the centre of the grid cells (control volumes). Field variables (stored at cell centers) must be interpolated to the faces of the control volumes.
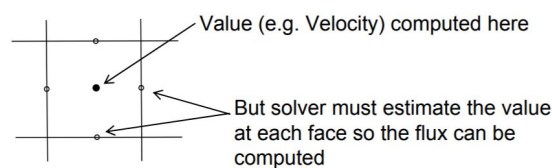
Figure 4.17: Control Volume

The interpolation schemes for the convection term are:

– First-Order Upwind – Easiest to converge, only first-order accurate.

– Power Law – More accurate than first-order for flows when Recell < 5 (typical low Re flows)

– Second-Order Upwind – Uses larger stencils for 2nd order accuracy, essential with

74

tri/tet mesh or when the flow is not aligned with the grid; convergence may be slower mesh or when the flow is not aligned with the grid; convergence may be slower.

– Monotone Upstream-Centered Schemes for Conservation Laws (MUSCL) – Locally 3rd order convection discretisation scheme for unstructured meshes; more accurate in predicting secondary flows, vortices, forces, etc.

– Quadratic Upwind Interpolation (QUICK) – Applies to quad/hex and hybrid meshes, useful for rotating/swirling flows, 3rd-order accurate on a uniform mesh.

Gradients of solution variables are required in order to evaluate diffusive fluxes, velocity derivatives, and for higher-order discretisation schemes.

The gradients of solution variables at cell centers can be determined using three approaches:

– Green-Gauss Cell-Based – Least computationally intensive. The solution may have false diffusion.

– Green-Gauss Node-Based – More accurate/computationally intensive; minimizes false diffusion; recommended for unstructured meshes.

– Least-Squares Cell-Based – Default method; has the same accuracy and properties as Node-based Gradients and is less computationally intensive.

Interpolation schemes for calculating cell-face pressures when using the pressure-based solver in FLUENT are available as follows:

– Standard – The default scheme; reduced accuracy for flows exhibiting large surface-normal pressure gradients near boundaries (but should not be used when steep pressure changes are present in the flow – PRESTO! scheme should be used instead) should be used instead.)

– PRESTO! – Use for highly swirling flows, flows involving steep pressure gradients (porous media, fan model, etc.), or in strongly curved domains

– Linear – Use when other options result in convergence difficulties or Use when other options result in convergence difficulties or unphysical behaviour

– Second-Order – Use for compressible flows; not to be used with porous media, jump, fans, etc. or VOF/Mixture multi-phase models

– Body Force Weighted – Use when body forces are large, e.g., high Ra natural convection or highly swirling flows

4.3.5.2 Pressure-Velocity Coupling

Pressure-velocity coupling refers to the numerical algorithm which uses a combination of continuity and momentum equations to derive an equation for pressure (or pressure correction) when using the pressure-based solver. [82]

Five algorithms are available in FLUENT.

- Semi-Implicit Method for Pressure-Linked Equations (SIMPLE). The default scheme, robust.

- SIMPLE-Consistent (SIMPLEC). Allows faster convergence for simple problems (e.g., laminar flows with no physical models employed).

- Pressure-Implicit with Splitting of Operators (PISO). Useful for unsteady flow problems or for meshes containing cells with higher than average skewness

- Fractional Step Method (FSM) for unsteady flows. Similar characteristics as PISO.

- Coupled (this is how the pressure-based coupled solver, described previously, is enabled)

For this work, the settings used are shown in table 4.6. Using the RSM creates a high degree of coupling between the momentum equations and the turbulent stresses in the flow, and thus the calculation can be more prone to stability and convergence difficulties than with the k-ε models. When we use the RSM, therefore, we may need to adopt special solution strategies in order to obtain a converged solution. The following strategies are generally recommended and have been adopted:

- Begin the calculations using the standard k-ε model. Turn on the RSM and use the k-ε solution data as a starting point for the RSM calculation.

- Use low under-relaxation factors (0.2 to 0.3).

Table 4.6: Solution Methods

	1º Phase	2º Phase	3º Phase
Pressure-Velocity Coupling			
Scheme	Coupled	Coupled	Coupled
Spatial Discretization			
Gradient	Green-Gauss Node Based	Green-Gauss Node Based	Green-Gauss Node Based
Pressure	Second Order	Second Order	Second Order
Density	First Order Upwind	First Order Upwind	Second Order
Momentum	First Order Upwind	First Order Upwind	Second Order
Turbulent Kinetic Energy	First Order Upwind	First Order Upwind	Second Order
Turbulent Dissipation Rate	First Order Upwind	First Order Upwind	Second Order
Reynolds Stresses	First Order Upwind	First Order Upwind	Second Order
Energy	First Order Upwind	First Order Upwind	Second Order
Mean Mixture Fraction	First Order Upwind	First Order Upwind	Second Order
Mixture Fraction Variance	First Order Upwind	First Order Upwind	Second Order

For this reason, it has been used the standard k-ε and first-order upwind (this will be denominated as the first phase) for the interpolation schemes for the convection term because allows for an easy convergence and is a good starting point. After this converge the model is changed to the RSM (second phase) and after it was converged the interpolation schemes for the convection term is change to Second Order. In between all of these phases done a gradient adaption with the method Gradient using the gradients of the Absolute Pressure, refine Threshold should be set to 10% of the value reported in the Max field.

4.3.5.3 Standard Initialization

The solver works in an iterative manner. Therefore before the very first iteration, a value must exist for every quantity in every grid cell. The more realistic the value, the better (quicker) convergence will be. For this case, it has been selected the Standard Initialization with the compute from Injector_1 that is the central injector, the FLUENT guide advice using an inlet because will allow for a better starting point.

4.3.5.4 Convergence

The solver should be given sufficient iterations such that the problem is converged. At convergence, the following should be satisfied:

- The solution no longer changes with subsequent iterations.

- Overall mass, momentum, energy, and scalar balances are achieved.

- All equations (momentum, energy, etc.) are obeyed in all cells to a specified tolerance.

The convergence criteria that has been chosen is shown in table 4.7.

Table 4.7: Convergence Criteria

Residual	Absolute Criteria
continuity	0.001
x-velocity	0.001
y-velocity	0.001
z-velocity	0.001
energy	$1e^{-06}$
k	0.001
epsilon	0.001
uu-stress	0.001
vv-stress	0.001
ww-stress	0.001
uv-stress	0.001
vw-stress	0.001
uw-stress	0.001
fmean	0.001
fvar	0.001
p1	$1e^{-06}$

Another important metric to assess whether the model is converged is to check the overall heat and mass balance.

The net flux imbalance (shown in the GUI as Net Results) should be less than 1% of the smallest flux through the domain boundary.

If solution monitors indicate that the solution is converged, but the solution is still changing or has a large mass/heat imbalance, this clearly indicates the solution is not yet converged.

4.3.5.5 Under-Relaxation Factors

Under-relaxation factor, α, is included to stabilize the iterative process for the pressure-based solver. If the value is too high, the model will be unstable, and may fail to converge unstable, and may fail to converge. If the value is much too low, it will take longer (more iterations) to converge. The Under-Relaxation Factors used are shown in table 4.8.

Table 4.8: Solution Controls: Under-Relaxation Factors (URF)

	1º Phase	2º Phase	3º Phase
Flow Courant Number	1	1	1
Explicit Relaxation Factors			
Momentum	0.3	0.3	0.3
Pressure	0.4	0.4	0.4
Under-Relaxation Factors (URF)			
Density	0.3	0.25	0.2
Body Forces	0.3	0.25	0.2
Turbulent Kinetic Energy	0.7	0.7	0.7
Turbulent Dissipation Rate	0.7	0.7	0.7
Turbulent Viscosity	1	1	1
Reynolds Stresses	0.5	0.47	0.47
Energy	1	1	1
Temperature	1	1	1
P1	0.99	0.99	0.98
Mean Mixture Fraction	1	1	1
Mean Fraction Variance	0.9	0.9	0.9

Chapter 5

Results

In this chapter will be discussing the CFD outcomes. The flow field is accurately analysed to identify causes of combustion inefficiency, and the results are compared with the experimental measurements to infer the reliability of the model.

It will start with an evaluation of convergence; an evaluation of the y^+ to make sure that this parameter is between the recommended range and an evaluation of the mass imbalance.

5.1   Convergence Evaluation

There are three indicators that convergence has been reached:

1. The residuals have decreased to a sufficient degree. The solution has converged when the Convergence Criterion for each variable has been reached. The default criterion is that each residual will be reduced to 10^{-3}, except the energy residual, for which the default criterion is 10^{-6}.

2. The solution no longer changes with more iterations.

3. The overall mass, momentum, energy, and scalar balances are obtained.

   A way of checking if the residuals tolerance are correct, and the solution completely converges, is through the mass imbalance. The net imbalance should be less than 0.5% of the net flux through the domain when the solution has converged, i.e., the flow that enters the system should be equal to that going out. In the present study, the mass imbalance obtained does not fulfilled this requirement because the flow at the outlet was compressible, but the mass imbalance contour has been visualized and there was not a wide range of values in the region of interest.

5.2 Y^+

The wall y^+ is a non-dimensional number similar to local Reynolds number, determining whether the influences in the wall-adjacent cells are laminar or turbulent, hence indicating the part of the turbulent boundary layer that they resolve.

The subdivisions of the near-wall region in a turbulent boundary layer can be summarized

as follows:

1. $y^+ < 5$: in the viscous sublayer region.

2. $5 < y^+ < 30$: buffer region.

3. $y^+ > 30$: Fully turbulent portion or log-law region.

Accurate presentation of the flow in the near-wall region determines successful prediction of wall-bounded turbulent flows. Values of close to the lower bound ($y^+ \approx 30$) are most desirable for wall functions where $y^+ \approx 1$ are most desirable for near wall modeling.
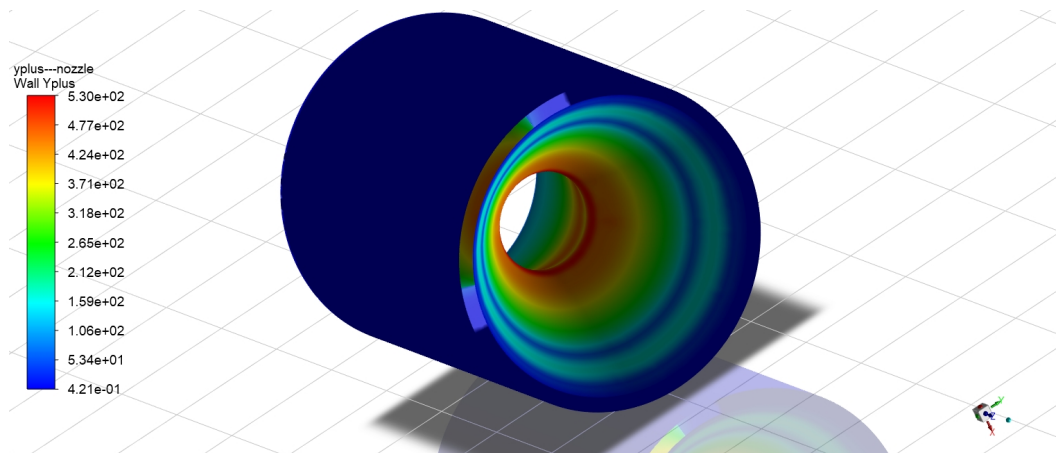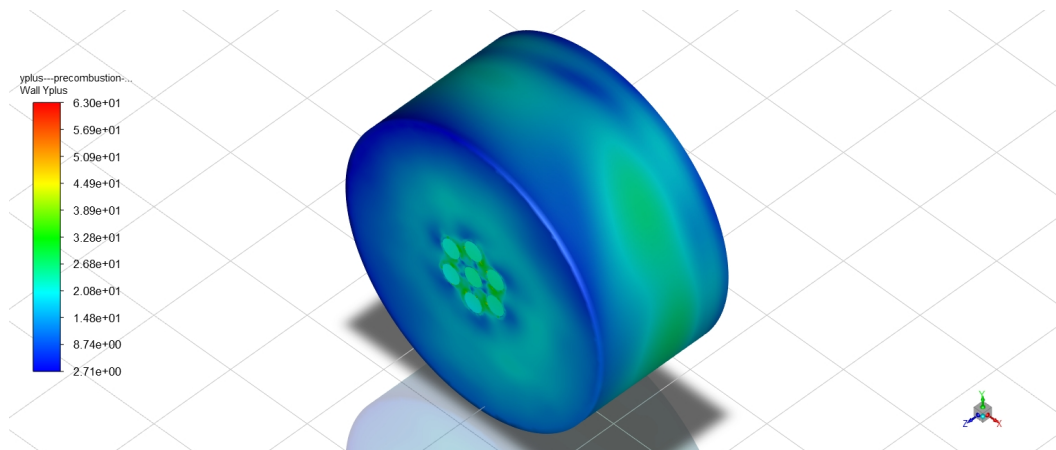

Figure 5.1: Contours of Wall y^+ for the nozzle

Figure 5.2: Contours of Wall y^+ for the precombustion chamber

The average value obtained was 58. In figure 5.1 is possible to see that there are some zones that acquire a high y^+ value. This means that the mesh in these zones needs to be more refined, but as the use of the computer was already on the limit, it would be more difficult to refine the desired areas. However, this parameter is not important because in this study is not considered the heat transfer.

5.3 Test 5

Set with the parameters inferred in the previous chapter, the simulation of Test 5 is described in this section.

5.3.1 Steady ($t_b = 1.5\ s$)

The chamber pressure measured in the experiment at $t_b = 1.5\ s$ was $24\ bar$. Figure 5.3 is a mapping of the combustion chamber pressure calculated with FLUENT in a plane YZ section. The software underestimates the pressure providing a measure of $18.5\ bar$, which is the $76.4\ \%$ of the measured combustion chamber pressure. This error is probably due to the combustion and turbulence models chosen, and different solutions will be implemented in a future research.
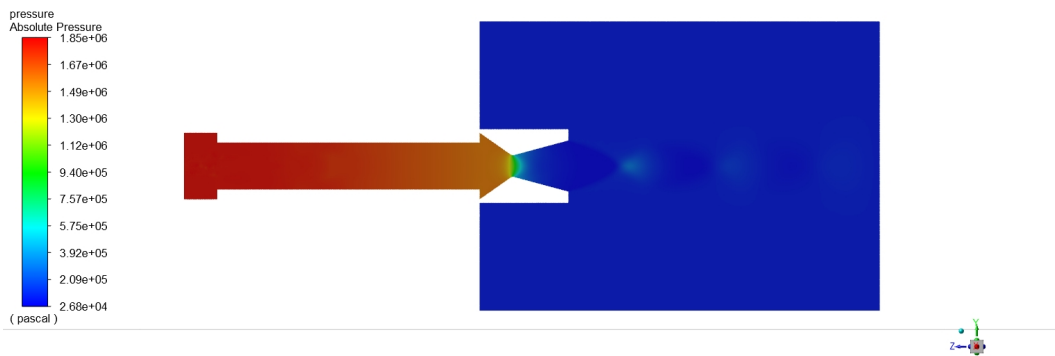
Figure 5.3: Contours of absolute pressure (pascal)

While the absolute values predicted with the CFD often prove to be unreliable, they can be used for a comparison between design solutions and to investigate why the performance dissatisfied the requirements. In fact, the predicted flow field resembles the typical flow in the experimental tests.
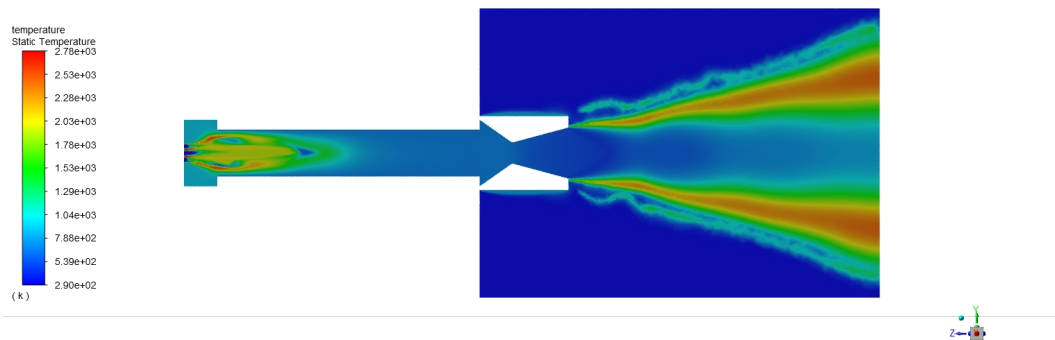
Figure 5.4: Contours of static temperature (K)

The temperature contour of figure 5.4 illustrates the flame structure inside the chamber. The countors highlight one relevant feature of the flow field. Near the injection plate, due to the step connecting the fuel grain to the precombustion chamber, the hot gas recirculates. This vorticity acts as flame holder.

Another way to see the flame structure is with the OH mass fraction contours (figure 5.5).
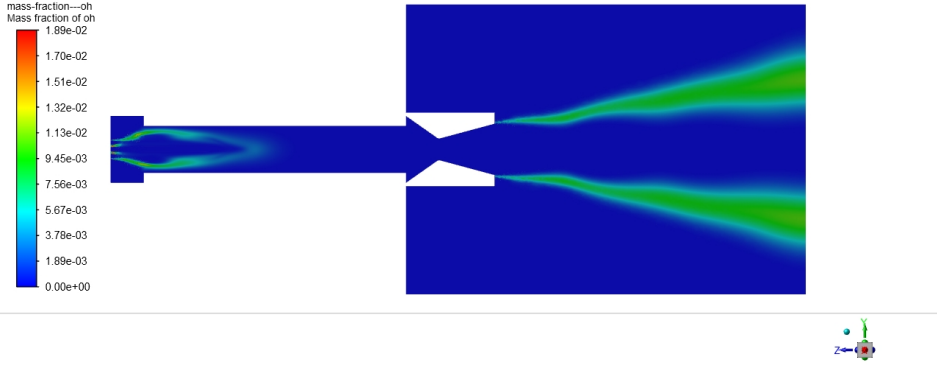
Figure 5.5: Contours of mass fraction of OH

The flame is closer to the chamber walls but the flow is faster so the fuel is stripped away from the grain, as shown in the C_2H4 mass fraction (figure 5.6). The temperature in this region is slightly lower than on the rest of the burning surface. However this is true only for the surface hit by the injectors. Since the oxidizer stream is swirling it doesn't impact homogeneously with the grain, thus resulting in a different combustion behaviour, dependent on the angular position with respect to the plate. This was experimentally confirmed, as shown in figure 5.7, which is a photograph of the inside of the combustion chamber, seen from the injectors, after a burn shorter than 2 seconds.
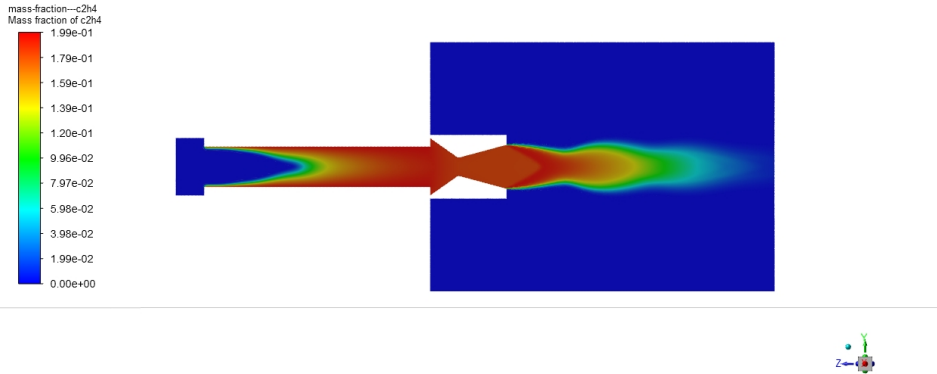
Figure 5.6: Contours of mass fraction of C_2H_4

Figure 5.7: Fuel Grain burn pattern

The excess of oxidizer in the internal part of the combustion chamber is also highlighted by the streamlines of the flow. If they are plotted from an external injector to the nozzle (figure 5.8), it can be seen that the rotation given by the swirl pushes the oxidizer closer to the walls feeding the reaction. The streamline from the internal injector (figure 5.9), on the other hand, never deviates from a straight trajectory and the flow exits the motor almost undisturbed. The actual benefit provided by the central orifice to the combustion has been investigated in the next section.
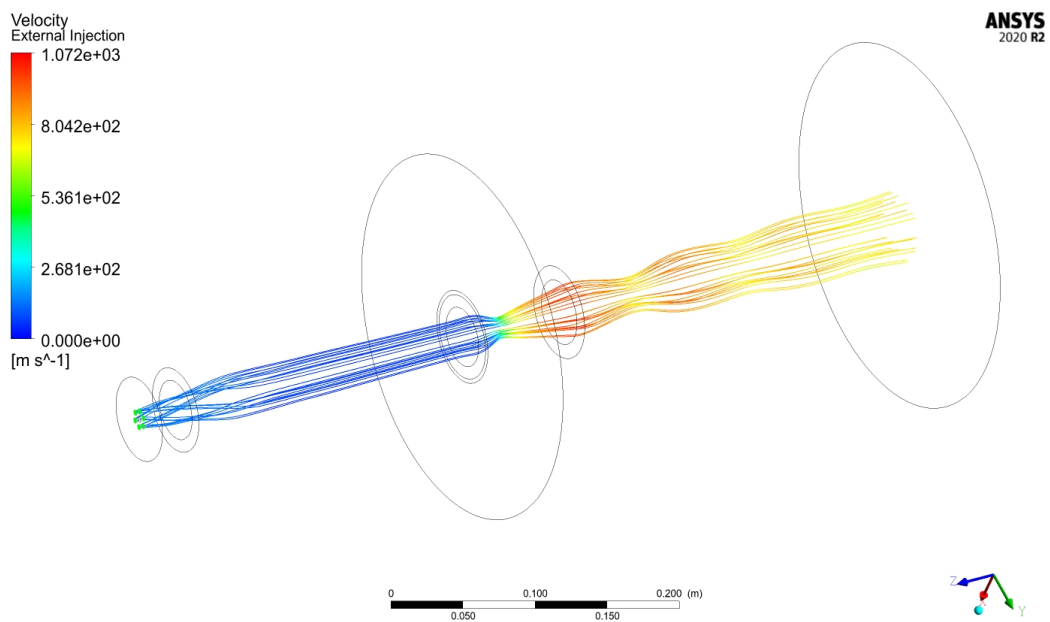
Figure 5.8: External injector velocity streamline
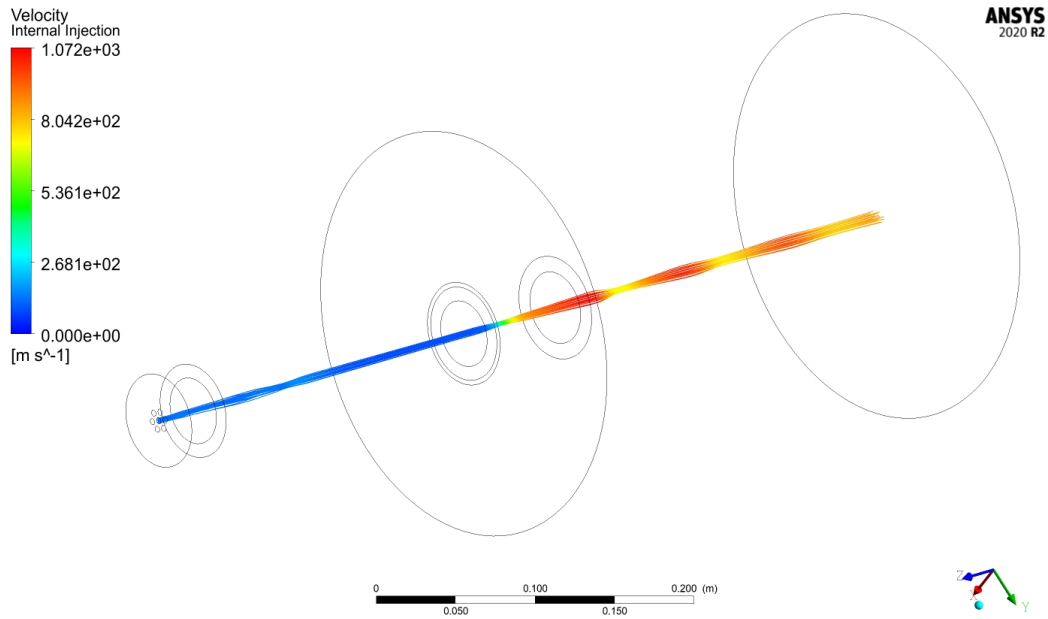
Figure 5.9: Central injector velocity streamline

Only a small amount of fuel flows in the precombustion chamber, but nevertheless the temperature increases. This phenomenon is explained by the recirculation of the hot gases induced by the turbulence. The products accumulate and get warmer; the wall is also modeled as adiabatic so there is no cooling of the flow by heat dissipation. The adiabatic hypothesis is valid for a burn time as short as 1.5 seconds. A closer look on the vorticity in the precombustion chamber is given in figure 5.10, where the plot of the velocity vectors in the plane highlights the hot eddies.
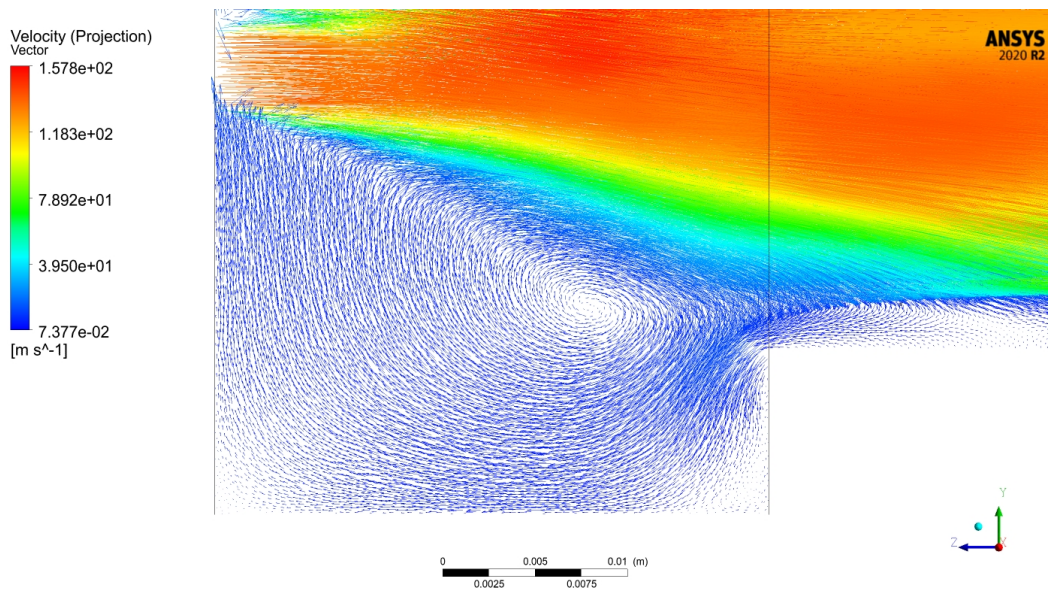
Figure 5.10: Flow recirculation in the precombustion chamber

84

5.3.2 Transient

In this subsection it will be analyse some performance parameters such as thrust, thrust coefficient, characteristic velocity, chamber pressure and the combustion efficiency; and understand the influence of the regression rate in the performance. For a quick analysis of the numerical simulation with the experimental results the average values of the performance were taken into account and are shown in the table 5.1. This comparison is also made graphically, through superimposition of the experimental and numerical values. The investigation is conducted on the curves of the Thrust (figure 5.11) and Combustion Chamber Pressure (figure 5.12). The experimental curve is plotted in black in the figure, while the numerical simulation in red.

Table 5.1: Average Values of the Experimental and Numerical Results and Deviation

	Average Thrust [N]	Chamber Pressure [bar]	Thrust Coefficient	Characteristic Velocity [m/s]
Experimental Result	704	24.2	1.27	1139
Numerical Result	863.96	19.23	1.213	984.82
Deviation [%]	22.72	20.54	21.35	13.54
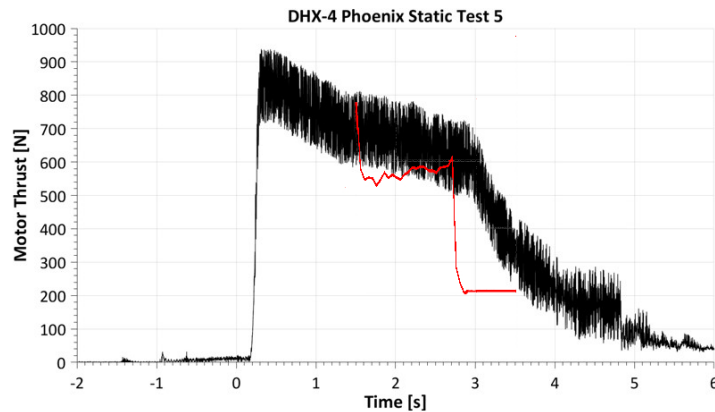
Figure 5.11: Test 5 - Thrust Comparison
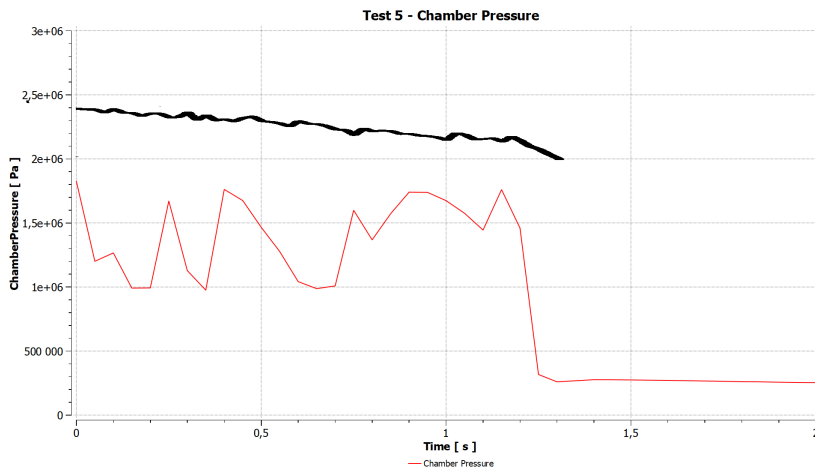
Figure 5.12: Test 5 - Chamber Pressure Comparison

85

(a) 0s

(b) 0.2s

(c) 0.4s

(d) 0.6s

(e) 0.8s

(f) 1s

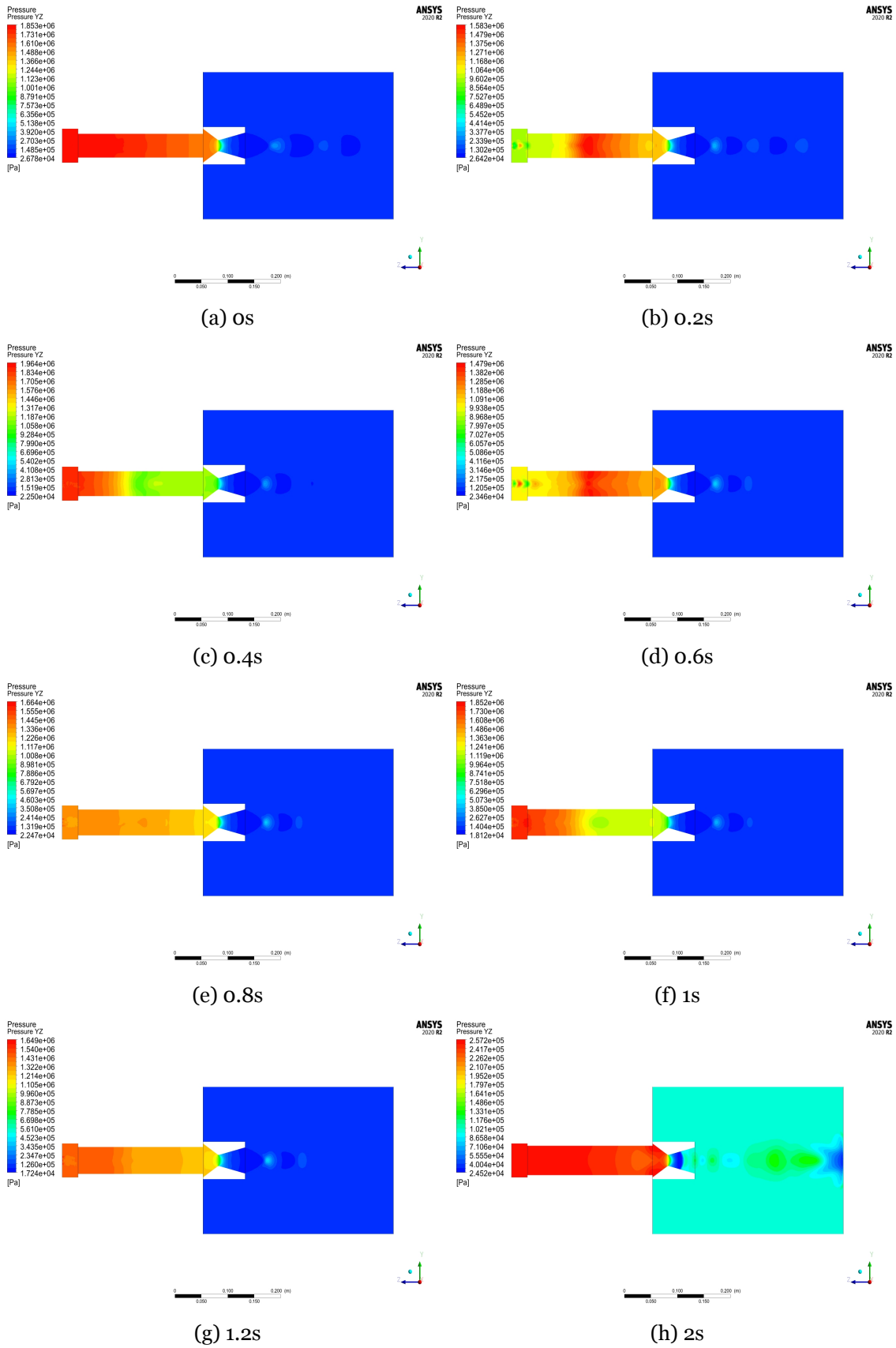(g) 1.2s

(h) 2s

Figure 5.13: Pressure Contours throw time (0 seconds corresponds to 1.7 seconds in the experimental)
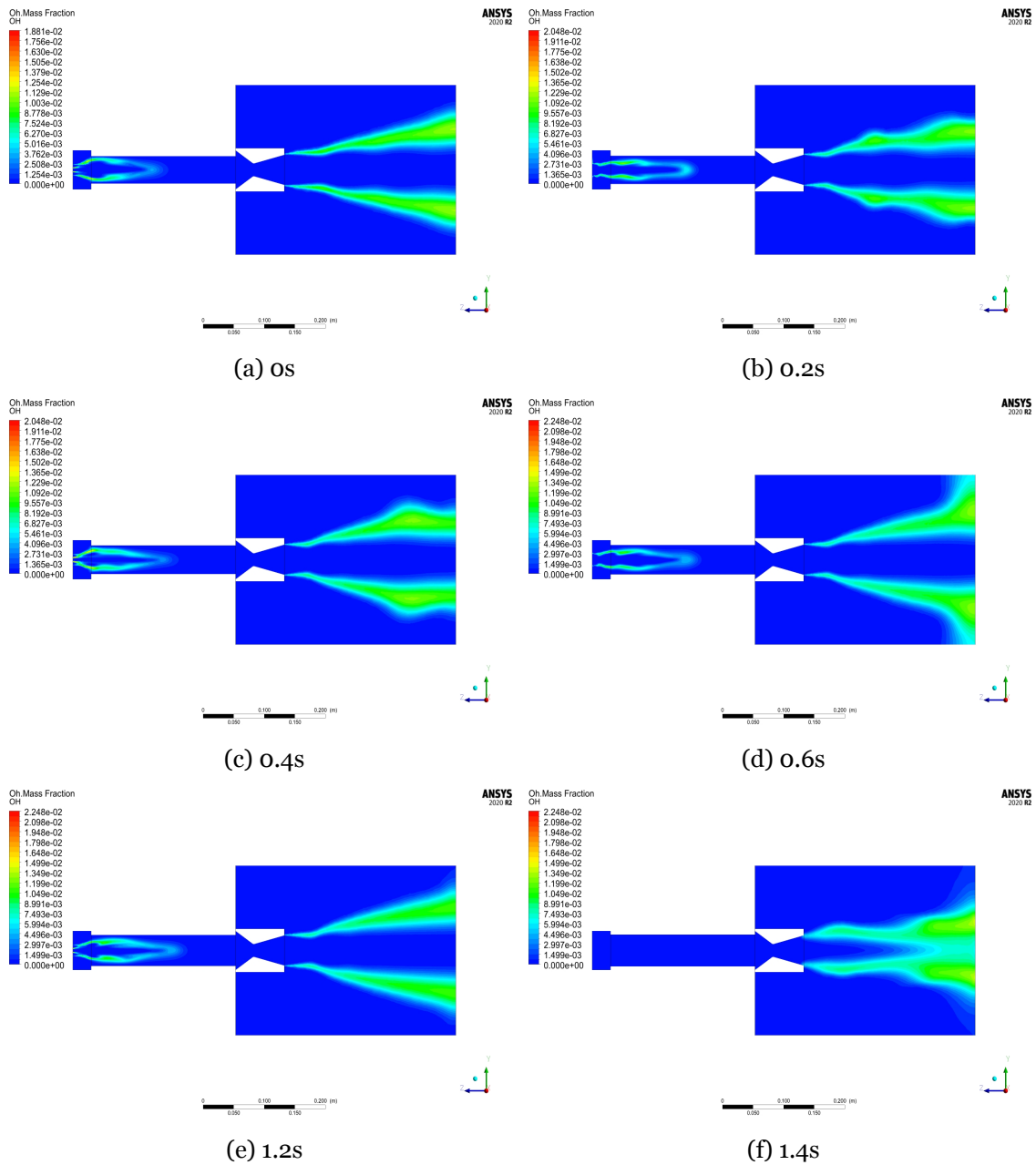
Figure 5.14: OH mass fraction contours throw time (0 seconds corresponds to 1.7 seconds in the experimental)

5.4   Axial Injection

In this section it will be analyse if the injection wasn't swirled but axial. Simulations with a zero angle of injection have been performed. The axial injection allows for a more uniformly distribution of the oxidizer in the combustion chamber, and still accumulates in the core of the motor. The heat still rises in the precombustion chamber.
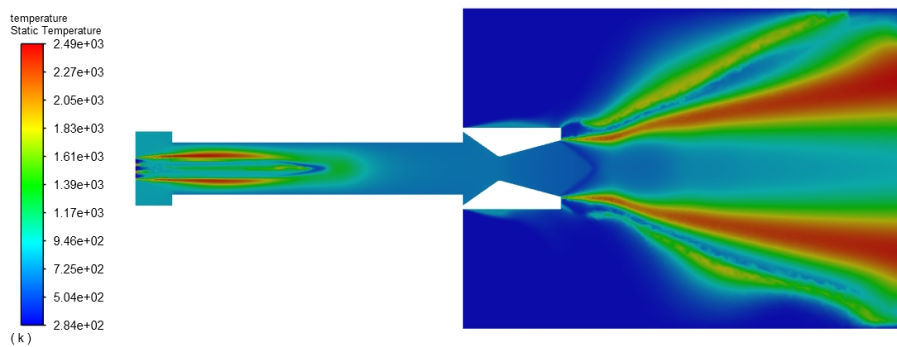
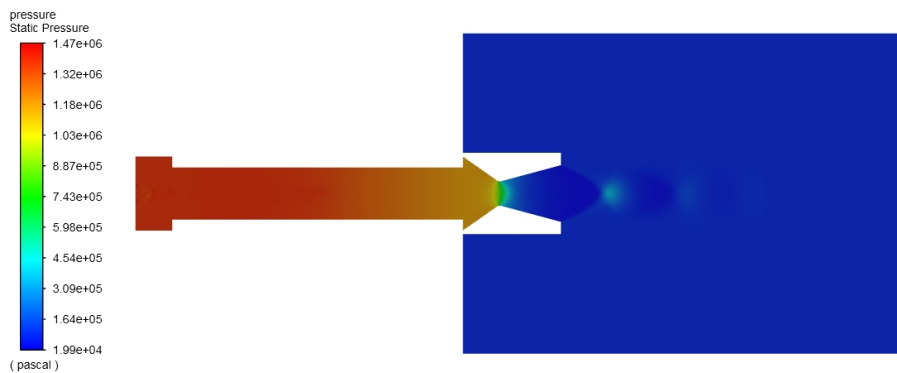Figure 5.15: Contours of static temperature (K)

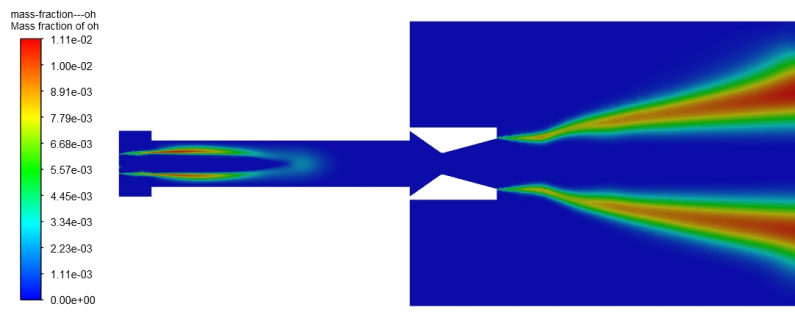Figure 5.16: Contours of absolute pressure (pascal)

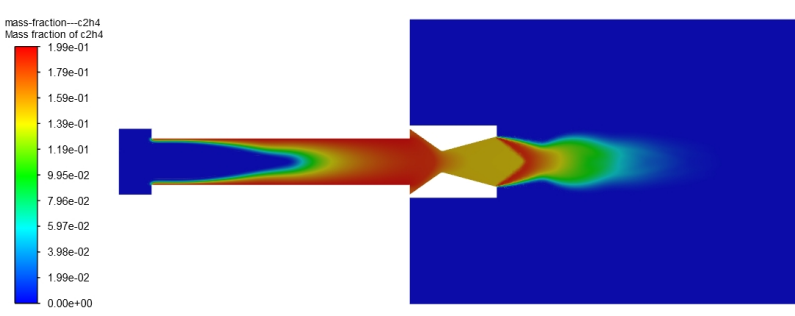Figure 5.17: Contours of mass fraction of OH

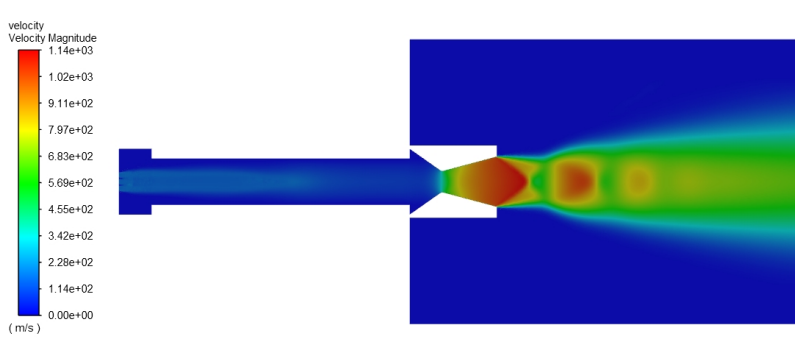Figure 5.18: Contours of mass fraction of C_2H_4

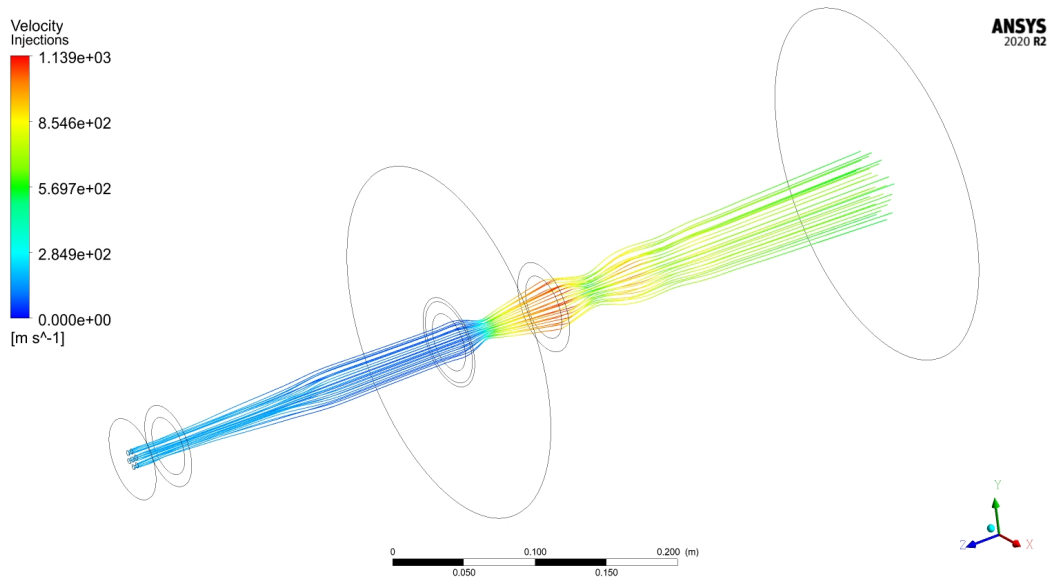Figure 5.19: Contours of velocity magnitude (m/s)
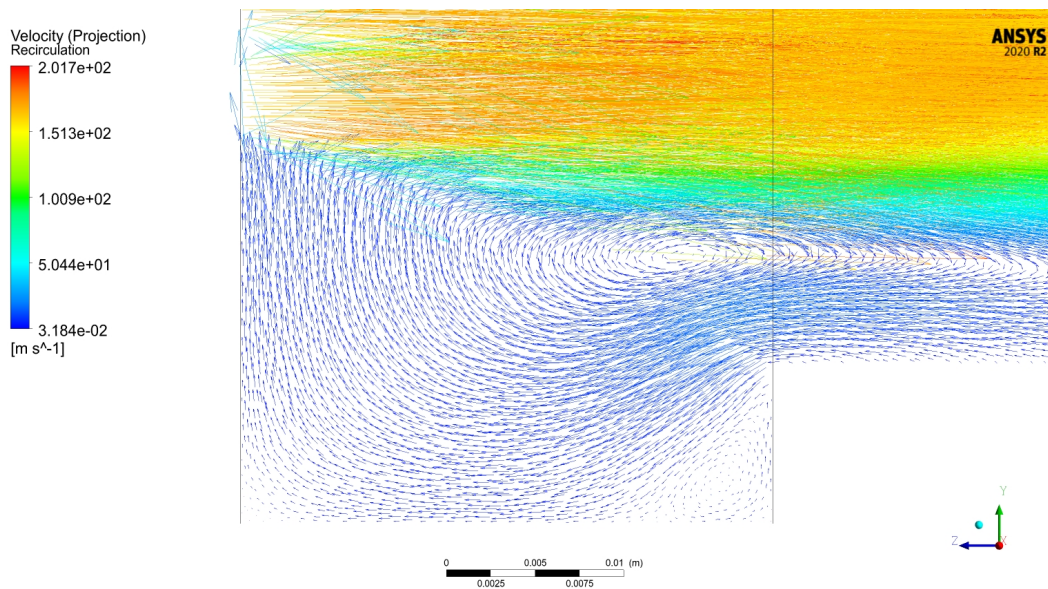
Figure 5.20: Injectors velocity streamline

Figure 5.21: Flow recirculation in the precombustion chamber

If these results are compared with the tests results it emerges that the introduction of a swirl angle of 15 degrees doesn't drastically increase the performances. Another solution could be increasing the swirl angle, which would increase the turbulence in the precombustion chamber and could reduce the phenomenon of re-circulation that reduces the resistant of the motor case. All these statements, as well as the effect of the introduction of a mixer in the system, will be discussed in a future work through more CFD simulations.

Chapter 6

Conclusion

6.1   CFD Results Analysis

The CFD shed some light on the flow field inside the combustion chamber, underlining some weak points of the design:

- The swirl injection allow for a better mixing of the reactants. The results obtained with the axial injection simulation provided a lower performance.

- The step between the precombustion chamber and the fuel grain induces a re-circulation of the flow which increases the temperature of the gas at the beginning of the motor and can represent a structural problem. This vorticity envelopes the Nitrous Oxide flow going against the diffusion of the oxidizer.

- The absence of a re-circulation zone at the end of the fuel grain and before the nozzle doesn't allow for the mixing of the reactants, decreasing the efficiency of the system.

- Nitrous Oxide flowing through the central orifice doesn't leave the core of the motor and is ejected almost undisturbed from the combustion chamber, which prevents it from coming into contact with the fuel.

- The formation of $C_{(s)}$ indicates that the O/F ratio is too high, that will provoke a reduction of the I_{sp} and traction because the presence of the solid carbon implies a worse expansion.

6.2   Design Improvements

From the CFD results some consideration can be made on the design of the system, to increase the performances:

- The precombustion chamber should be longer or with a cross section narrower (an example can be seen in figure 6.1) than the port area, creating a re-circulation of the flow on the opposite direction which could allow for a better diffusion of the oxidizer. This should also decrease the accumulation of hot gas in the area, increasing the life of the motor case.

- The swirl angle could be either increased since the vorticity proved to be insufficient to increase the oxidizer diffusion.

- Since the central orifice doesn't leave the core of the motor and don't contact directly with the fuel, one solution is use a multi-port (example wagon-wheel) grain design that allows a better blending of the oxidizer with the fuel and increase the regression rate.

- A mixing device could be also adopted to increase the reactants blending in the combustion chamber, using either a diaphragm or a mixer at the end of the fuel grain. This would change the flame pattern in the convergent part of the nozzle leading to a complete combustion.

- The regression rate is low and his is one of the biggest problems of this type of rockets, as we already discussed, one of the ways to solve this problem is to use a multi-port grain design, that will increase the burning surface area.
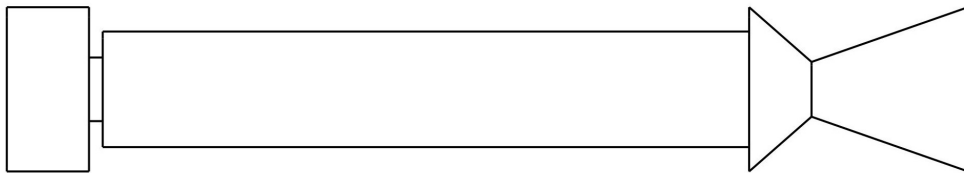

Figure 6.1: Alternative concept

6.3 Future Work

Future developments in this area can be focused in the following items:

- Use of the density-based solver instead of the pressure-based solver, because the first is the recommended to be used when the flow is compressible with M > 0.3. The density-based solver allow to solve in a vector form the equations for continuity, momentum, energy and species simultaneous instead of sequentially. In this way the density density-based solver is applicable when there is a strong coupling, or interdependence, between density, energy, momentum, and/or species. This occur when exist high speed compressible flow with combustion (witch is the case), hypersonic flows and shock interactions.

- With the use of the density-based solver the non-premixed combustion is deactivated and the species transport is the only model that exist for the species. Because of this will be necessary to create a mechanism with all the equations. The better and simple approach it will be to use the eddy dissipation concept, so the inputs were the stoichiometric coefficients. And treat the equation like a simple forward equation, so the rate

92

exponents for the reactants it will be 1, and for the products it will be 0.

- One of the main assumptions is the fuel and oxidizer are already vaporised, for future works the fuel should be, at least, introduced in a form of a liquid. Because the solid fuel creates a very thin liquid layer on the fuel face when it burns. This introduction will allow to study the liquid entrainment mechanism. For this item, it will be necessary to use the $k-omega$ with a y^+ close to 1.

- For this work, it was assumed that the regression rate is constant, this was possible because the burning time was very short. However, for future work in which the simulation time may be longer, a UDF (using the algorithm in Appendix F) can be made which calculates the regression rate as a function of the flow field inside the combustion chamber and the value will vary and will be more closer to the real one.

Bibliography

[1] B. Cantwell, A. Karabeyoglu, and D. Altman, *RECENT ADVANCES IN HYBRID PROPULSION.* 8th ISICP, 2009. 2, 11

[2] Wikipedia. (2017) Gird-09. [Online]. Available: https://pt.wikipedia.org/wiki/ GIRD-09 2

[3] *AA283Aircraft and Rocket Propulsion BOOK.* 3, 4, 9, 10, 11, 16, 17, 18, 25, 26, 27, 28

[4] F. Miranda, "Design optimization of ground and air-launched hybrid rockets: Development of an optimisation tool for multi-technology rocket launch vehicle design," 2015. 3, 5

[5] A. Karabeyoglu, "Hybrid rocket propulsion for future space launch," 2008. 5

[6] . (2014) Virgin galactic, overview - safety. [Online]. Available: http://www. virgingalactic.com/overview/safety/ 5

[7] M. V. Kesteren, "Air launch versus ground launch - literature study," *Literature study for master thesis, Delft University of Technology*, 2008. 5

[8] W. J. Larson and J. R. Wertz, *Space Mission Analysis and Design.* Microcosm Press and Kluwer Academic Publishers, 2005. 6

[9] J. McFarlane, R. Kniffen, and J. Lichatowich, "Alaa 93-2551 design and testing of amroc's 250,000 ibf thrust hybrid motor," 1993. 6

[10] B. Zandbergen, "Hybrid rocket motors (data collection).pdf," 2015. 6

[11] S. Chang, C. Lee, and K. Shin, "The enhancement of regression rate of hybrid rocket fuel by various methods," *43rd AIAA – Aerospace Sciences Meeting and Exhibit, Reno, Nevada*, 2005. 7

[12] L. M. C. Santos, L. A. R. Almeida, A. M. Fraga, and C. A. G. Veras, "Experimental investigation of a paraffin based hybrid rocket," *10th Brazilian Congress of Thermal Sciences and Engineering, Rio de Janeiro*, 2004. 7

[13] L. A. R. Almeida and L. M. C.Santos, "Projecto, construção e lançamento de um foguete híbrido a base do par propelente parafina – n2o," *Projecto de Graduação. Universidade de Brasília*, no. 83, 2005. 7

[14] R. Theba, K. Veale, and C. Bemont, "Development of a combustion visualisation hybrid rocket motor," *R D Journal of the South African Institution of Mechanical Engineering*, no. 33, pp. 97–104, 2017. 7

[15] Y. Pal and V. R. Kumar, "Physical and ballistic characterization of aluminum-loaded paraffin hybrid rocket fuels," *Energy Fuels*, no. 31, p. 10133–10143, 2017. 7

[16] S. R. Gomes, L. R. Junior, J. A. F. F. Rocco, and K. Iha, "Experimental study of polyurethane-based fuels with addition of paraffin and aluminum for hybrid rocket motors," *J. Aerosp. Technol. Manag.*, vol. 5, no. 3, pp. 279–286, 2013. 7

[17] M. T. Migliorino, D. Bianchi, and F. Nasuti, "Numerical analysis of paraffin-wax/oxygen hybrid rocket engines," *JOURNAL OF PROPULSION AND POWER*, 2020. 7

[18] M. A. Karabeyoglu, D. Altman, and B. J. Cantwell, "Combustion of liquefying hybrid propellants: Part 1, general theory," *Journal of Propulsion and Power*, vol. 18, no. 3, pp. 610–620, 2002. 7

[19] M. A. Karabeyoglu and B. J. Cantwell, "Combustion of liquefying hybrid propellants: Part 1, stability of liquid films," *Journal of Propulsion and Power*, vol. 18, no. 3, pp. 621–630, 2002. 7

[20] M. A. Karabeyoglu, B. J. Cantwell, and J. Stevens, "Evaluation of homologous series of normal-alkanes as hybrid rocket fuels," *41st AIAA/ASME/SAE/ASEE Joint Propulsion Conference and Exhibit, AIAA Paper No.2005-3908, Tucson, AZ*, 2005. 8, 68

[21] A. Karabeyoglu and U. Arkun, "Evaluation of fuel additives for hybrid rockets and sfrj systems," *50th AIAA/ASME/SAE/ASEE Joint Propulsion Conference and Exhibit, AIAA Paper No. 2014-3647, Cleveland, OH*, 2014. 8

[22] M. Boiocchi, P. Milova, L. Galfetti, L. DiLandro, and A. K. Golovko, "A wide characterization of paraffin-based fuels mixed with styrene-based thermoplastic polymers for hybrid propulsion," *Progress in Propulsion Physics*, vol. 8, pp. 241–262, 2016. 8

[23] L. Galfetti, L. Merotto, M. Boiocchi, F. Maggi, and L. T. DeLuca, "Experimental investigation of paraffin-based fuels for hybrid rocket propulsion," *Progress in Propulsion Physics*, vol. 4, pp. 59–74, 2013. 8

[24] M. Calabro, "Overview on hybrid propulsion," *Progress in Propulsion Physics*, no. 2, pp. 353–374, 2011. 9, 18, 19, 20, 21, 22, 23, 24

[25] Koelle, *Handbook of astronautical engineering. 1st ed.* McGraw-Hill, 1961. 10

[26] M. Calabro, "Lox/htpb/alh3 hybrid propulsion for launch vehicle boosters," *AIAA 2004-3823, 40th Joint Propulsion Conf., Fort Lauderdale, FL*, pp. 1–5, 2004. 12, 18

[27] L. T. DeLuca, L. Rossettini, C. Kappenstein, and V. Weiser, "Ballistic characterization of alh_3-based propellants for solid and hybrid rocket propulsion," *AIAA 2009-4874, 45th Joint Propulsion Conf*, pp. 1–14, 2009. 12

[28] M. Calabro, L. T. D. Luca, L. Galfetti, H. Raina, and C. Perut, "Advanced hybrid solid fuels," *International Astronautical Federation, IAC-archive, IAC-07-C4.2.09*, 2007. 12

[29] Toru S. (2010) The forefront of space science, japan aerospace exploration agency. [Online]. Available: www.spg-corp.com/space-propulsion-group-resources.html 13

[30] G. P. Sutton, *Rocket Propulsion Elements – 6th Edition.* United States of America: John Wiley Sons, Inc., 1992. 13, 19

[31] R. W. Humble, G. N. Henry, and W. J.Larson, *Space Propulsion Analysis and Designer.* MacGraw-Hill Companies, Inc. Primis Custom Publishing, 1995. 13

[32] D. P. Jansen and L. F. Kletzkine, "Preliminary design of a 3 kn hybrid propellant engine," *ESA Journal*, vol. 12, pp. 421–439, 1998. 13

[33] A. Mazzetti, L. Merotto, and G. Pinarello, "Paraffin-based hybrid rocket engines applications: a review and a market perspective," *ActaAstronautica*, no. 126, pp. 286–297, 2016. 14

[34] M. Chiaverini, "Review of solid-fuel regression rate behaviour in classical and nonclassical hybrid rocket motors," *Progress in Astronautics and Aeronautics*, pp. 37–125, 2007. 14

[35] S. Kim, J. Kim, H. Moon, and et al., "Combustion characteristics of the cylindrical multiport grain for hybrid rocket motor," *Paper presented at: 45th AIAA/ASME/SAE/ASEE Joint Propulsion Conference Exhibit, Denver, Colorado*, 2009. 14

[36] L. Casalino, D. Pastrone, and F. Simeoni, "Hybrid rocket upper stage optimization: effects of grain geometry," *Paper presented at: 47th AIAA/ASME/SAE/ASEE Joint Propulsion Conference and Exhibit, San Diego, California*, 2011. 14

[37] R. Kumar and P. Ramakrishna, "Effect of protrusion in the enhancement of regression rate in hybrid rocket," *Paper presented at: 47th AIAA/ASME/SAE/ASEE Joint Propulsion Conference Exhibit., San Diego, California*, 2011. 14

[38] ——, "Enhancement of hybrid fuel regression rate using a bluff body," *J Propul Power*, no. 30, pp. 909–916, 2014. 14

[39] W. Knuth, M. Chiaverini, D. Gramer, and et al., "Solid-fuel regression rate and combustion behaviour of vortex hybrid rocket engines," *Paper presented at: 35th Joint Propulsion Conference Exhibit., Denver, Colorado*, no. 30, pp. 909–916, 1999. 14

[40] J. J. Caravella, S. Heister, and E. Wernimont, "Characterization of fuel regression in a radial flow hybrid rocket," *J Propul Power*, no. 14, pp. 51–56, 1998. 14

[41] M. Karabeyoglu, D. Altman, and B. Cantwell, "Combustion of liquefying hybrid propellants: Part 1, general theory," *J Propul Power*, no. 18, pp. 610–620, 2002. 14

[42] M. Karabeyoglu and B. Cantwell, "Combustion of liquefying hybrid propellants: Part 2, stability of liquid films," *J Propul Power*, no. 18, pp. 621–630, 2002. 14

[43] M. Karabeyoglu, G. Zilliac, B. Cantwell, and et al., "Scale-up tests of high regression rate paraffinbased hybrid rocket fuels," *J Propul Power*, no. 20, p. 1037–1045, 2004. 14

[44] S. Maruyama, T. Ishiguro, K. Shinohara, and et al., "Study on mechanical characteristics of paraffin based fuel," *Paper presented at: 47th AIAA/ASME/SAE/ASEE Joint Propulsion Conference Exhibit., San Diego, California*, 2011. 15

[45] R. Kumar and P. Ramakrishna, "Studies on eva-based wax fuel for launch vehicle applications," *Propellants Explos Pyrotech*, no. 41, p. 295–303, 2016. 15

[46] S. Kim, H. Moon, J. Kim, and et al., "Evaluation of paraffin–polyethylene blends as novel solid fuel for hybrid rockets," *J Propul Power*, no. 31, p. 1750–1760, 2015. 15

[47] J. Desain, B. Brady, K. Metzler, and et al., "Tensile tests of paraffin wax for hybrid rocket fuel grains," *Paper presented at: 45th AIAA/ASME/SAE/ASEE Joint Propulsion Conference Exhibit., Denver, Colorado*, no. 31, p. 1750–1760, 2009. 15

[48] M. J. Chiaverini and K. K. Kuo, "Fundamentals of hybrid rocket combustion and propulsion," *Progress in Astronautics and Aeronautics, American Institute of Aeronautics and Astronautics Inc.*, vol. 218, no. 31, p. 413–456, 2007. 15, 19, 22, 67

[49] L. Galfetti, L. Merotto, M. Boiocchi, and et al., "Experimental investigation of paraffin-based fuels for hybrid rocket propulsion," *EDP Sci*, p. 59–74, 2013. 15

[50] T. A. Boardman, "Design and test planning for a 250 klbf thrust hybrid rocket motor," *AIAA Paper*, no. 97-2804, 1997. 18, 20

[51] M. Calabro, "History of the european hybrids," *AIAA Propulsion lecture ser. Reno, NV*, 1991. 19

[52] D. Altman, "Rocket motors, hybrid," in *Encyclopedia of Physical Science and Technology (Third Edition)*, third edition ed., R. A. Meyers, Ed. New York: Academic Press, 2003, pp. 303–321. [Online]. Available: https://www.sciencedirect. com/science/article/pii/B0122274105008358 22

[53] A. J. M. Donald, "Chemical rocket propulsion and the environment," *AIAA Paper No. 1992-1660*, 1992. 23

[54] M. Calabro, "Coupled optimization between launch vehicle and large srb," *Advanced Solid Rocket Technologies Short Course. Indianapolis, USA*, 2002. 24

[55] E. M. Goodger and S. O. Ogaji, "Fuels combustion in heat engines," *Cranfield University Press*, no. 39, 2011. 29

[56] A. H. Lefebvre and D. R. Ballal, "Gas turbine combustion, third edition," *CRC Press, Boca Raton, United States Of America*, 2010. 30

[57] A. H. Lefebvre, "Atomization and sprays," *CRC Press*, vol. 1040, no. 2756, 1988. 31

[58] T. C. Lieuwen and V. Yang, "Gas turbine emissions," *Cambridge University Press*, vol. 38, 2013. 31, 32, 35

[59] D. Nascimento, "Desenvolvimento de uma câmara de combustão para uma turbina a gás, master's thesis," *Instituto Superior Técnico, Lisboa ,Portugal*, 2015. 33, 34

[60] ANSYS, *ANSYS FLUENT 12.0/12.1 Documentation.* ANSYS, Inc, 2009. 35, 46, 48, 49, 50, 52, 53, 54, 64, 67

[61] E. M. Goodger, *Transport Fuels Technology.* Norwich, UK: Landfall Press, 2000. 35

[62] P. Moreira, "Influência do ângulo de injeção nas emissões de poluentes e temperatura de combustão, master's thesis," *Universidade da Beira Interior, Covilhã,Portugal*, 2016. 36

[63] P. Queirós, "Atomização e combustão de glicerina, master's thesis," *Instituto Superior Técnico, Lisboa, Portugal*, 2011. 36

[64] T. H. Shih, W. W. Liou, A. Shabbir, Z. Yang, and J. Zhu, "A new k- e eddy-viscosity model for high reynolds number turbulent flows - model development and validation," vol. 24, no. 3, 1995. 36

[65] D. C. Wilcox, "Turbulence modeling for cfd, california: Dcw industries, inc." *La Canada, California*, vol. 24, no. 3, 1998. 36

[66] F. R. Menter, "Two-equation eddy-viscosity turbulence models for engineering applications." *AIAA Journal*, vol. 32, no. 8, 1994. 36

[67] D. K. Walters and D. Cokljat, "A three-equation eddy-viscosity model for reynolds averaged navier-stokes simulations of transitional flows." *Journal of Fluids Engineering*, vol. 130, no. 8, 2008. 37

[68] R. Mercier, "Turbulent combustion modeling for large eddy simulation of nonadiabatic stratified flames," *Master´s thesis, École Centrale Paris, France*, 2015. 37

[69] TUDelft. (2007) Cansat. [Online]. Available: http://dare.tudelft.nl/ projects-and-teams/cansat/ 39

[70] C. Merrill, "Nitrous oxide explosive hazards," *Air Force Research Laboratory, Edwards Air Force Base*, 2008. 40

[71] A. B. Fraters, "Hybrid rocket propulsion - future development steps in the field of hybrid rocket propulsion at delft aerospace rocket engineering," *Literature Survey, Delft University of Technology, Delft*, 2012. 40

[72] P. P. de Oliveira Alcaria Guerreiro, "Preliminary study of a hybrid rocket," 2013. 41

[73] R. Gelain, "Cfd simulations of self-pressurized nitrous oxide hybrid rocket motors," 2017. 45, 55, 66, 68

[74] J. M. I. Fernández, "Study of combustion using a computational fluid dynamics software (ansys)," *Universitat de Barcelona, Barcelona, Spain*, 2015. 45

[75] M. Zedda, "Introduction to cfd for combustion applications," *Gas Turbine Combustion, Cranfield University, short course*, 2015. 46

[76] S. R. Turns and et al., *An introduction to combustion*, ser. 287.   McGraw-Hill New York, 1996. 46

[77] J. Oliveira, "Cfd analysis of the combustion of bio-derived fuels in the cfm56-3 combustor," *Master's Thesis, Universidade da Beira Interior, Covilhã, Portugal*, 2016. 47

[78] B. E. Launder and D. B. Spalding, "Lectures in mathematical models of turbulence," *Academic Press, London, England*, 1972. 48

[79] T.-H. Shih, W. W. Liou, A. Shabbir, Z. Yang, and J. Zhu, "A new k-ε eddy-viscosity

model for high reynolds number turbulent flows - model development and validation," *Computers Fluids*, 1995. 49

[80] André Bakker. (2008) Lectures on applied. [Online]. Available: https://www.bakker.org/Lectures-Applied-CFD.pdf 53

[81] P. Chatterjee, "A computational fluid dynamics investigation of thermoacoustic instabilities in premixed laminar and turbulent combustion systems," *Ph.D. dissertation, Virginia Polytechnic Institute and State University*, 2004. 54

[82] A. Inc., "Lecture 5: Solver settings introduction to introduction to ansys fluent," 2010. 58, 59, 63, 73, 74, 76

[83] F. Barato, "Numerical and experimental investigation of hybrid rocket motors transient behavior," *Doctoral Thesis, University of Padova, Padova, Italy*, 2013. 67

[84] A. Tanksale, J. N. Beltramini, and G. M. Lu, "A review of catalytic hydrogen production processes from biomass," *Renewable and Sustainable Energy Reviews*, vol. 14, pp. 160–182, 2010. 68

[85] M. Lazzarin, M. Faenza, F. Barato, and et al, "Computational fluid dynamics simulation of hybrid rockets of different scales," *Journal of Propulsion and Power*, vol. 31, no. 5, 2015. 69

Appendix A

Drawing

All the dimensions are in [mm]
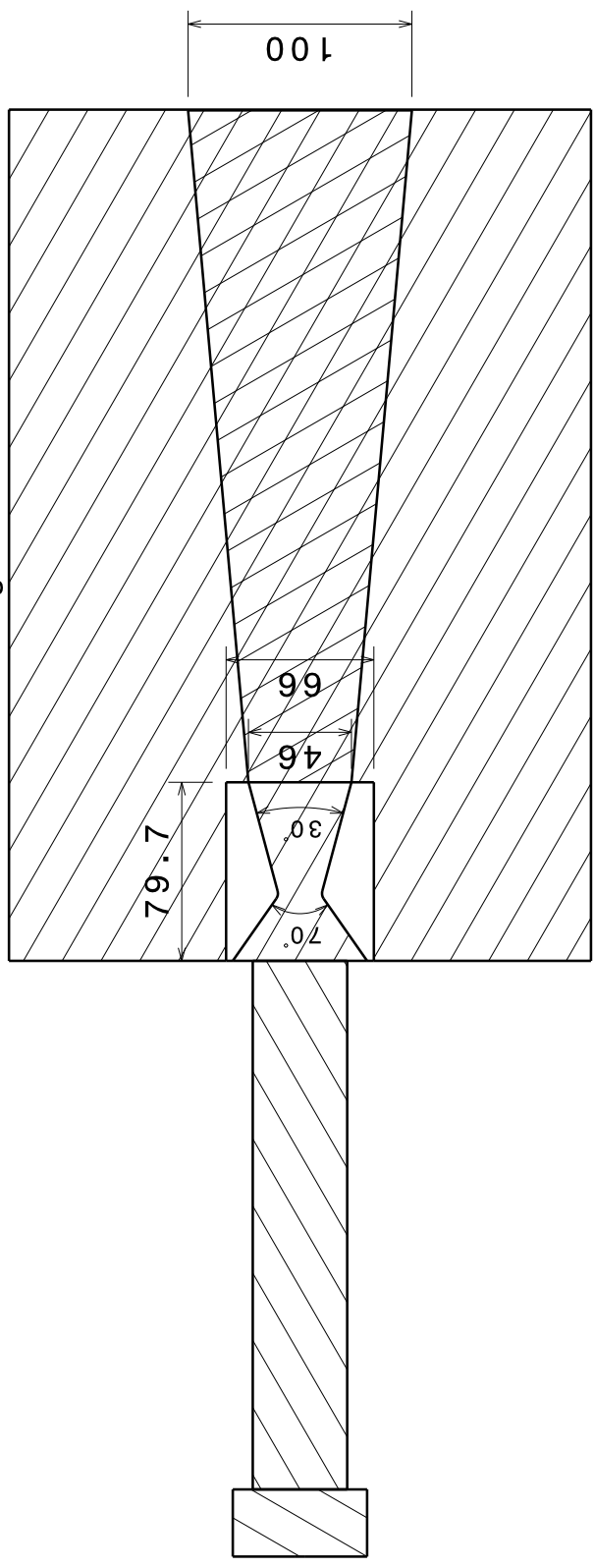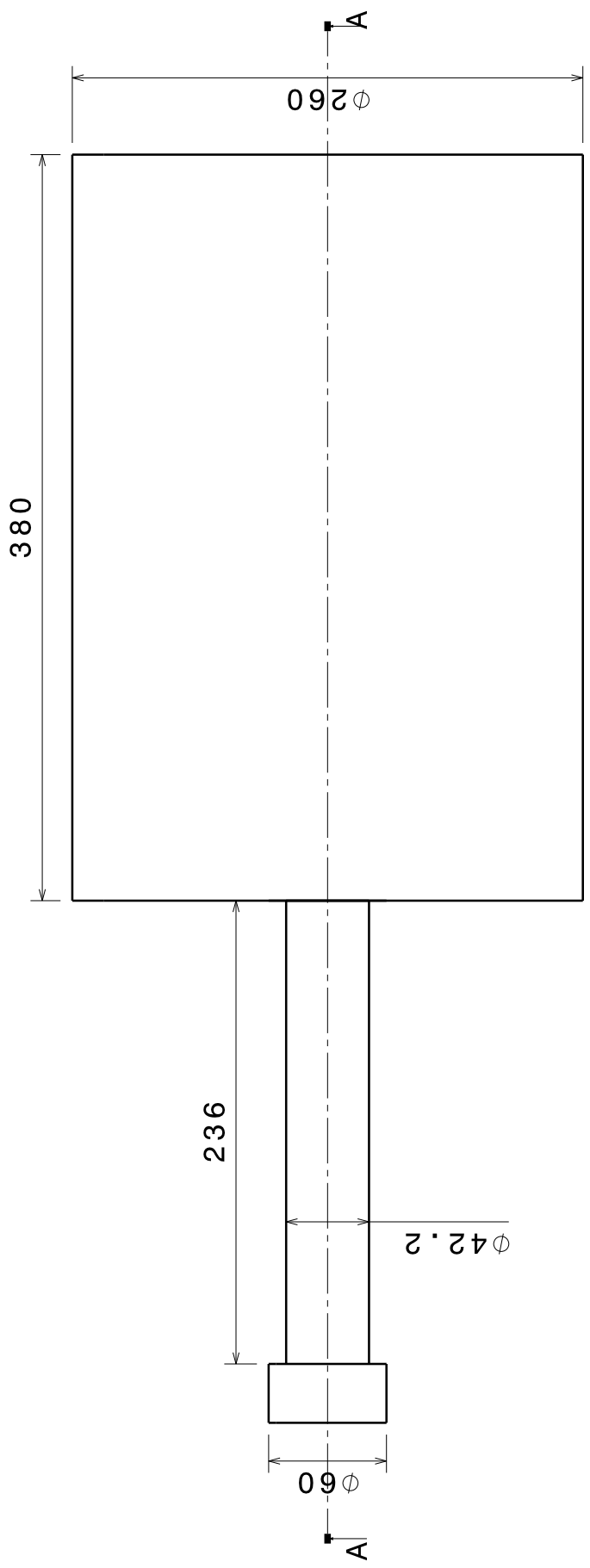
Right View

Section view A-A
Scale: 1:3

Ø260

380

236

Ø42.2

Ø60

A

A

100

66

46

79.7

30°

70°

Appendix B

Injection Configuration

Configuration - Test 5

The Test 5 version of the injector plate is made with 7 orifices of 4 mm diameter. One of them is in the center of the plate, the other six are equispaced on a circle of radius 6 mm. The external holes are inclined of 15º to swirl of the oxidizer flow.
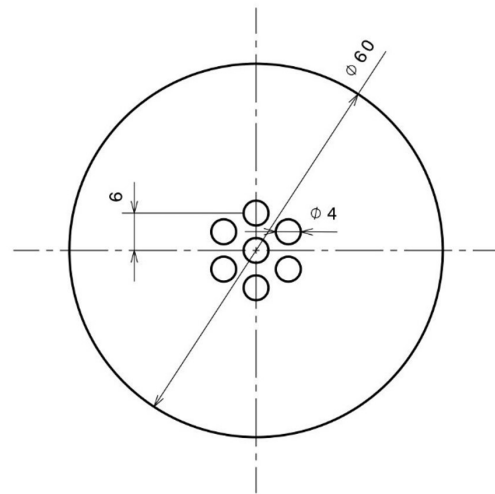
Figure B.1: Injector Configuration. (all dimensions are in [mm])

Appendix C

MATLAB CODE

```matlab
clear all
close all
clc

% Open the coordinates file
f = fopen('coordinates.lis','r');

%Creates the vectors for the coordinates
X = [];
Y = [];
Z = [];
NN = [];
cnt = 0;

%Read the coordiates file and write in the vectors
while ¬feof(f)
    try
        ST = fgetl(f);
        p = textscan(ST,'%d , %f , %f , %f ');
        if ¬any(cellfun('isempty',p))
            X = [X;p{2}];
            Y = [Y;p{3}];
            Z = [Z;p{4}];
            NN = [NN;double(p{1})];
        end
    catch
    end

    cnt = cnt + 1;
end

fclose(f);

% Size of should match num of nodes
Nodes = unique([X,Y,Z,NN],'rows');

% Sort by node number
[¬,H] = sort(Nodes(:,4));
```

```matlab
40
41  Nodes_Coords = Nodes(H,:);
42
43  fname = 'Trajectory.dat';
44
45  F = fopen(fname,'w');
46  M = Nodes_Coords;
47  Sz = size(M,1);
48
49  for ii = 1:Sz  % Number of Nodes.
50      for jj = 1:3 % dimensions
51          if ii==Sz && jj==3
52              fprintf(F,'%18.16f\n',M(ii,3+1));   % Write Node Numbers
53          else
54              fprintf(F,'%18.16f\t',M(ii,3+1));
55          end
56      end
57  end
58
59  for ii = 1:Sz  % Number of Nodes.
60      for jj = 1:3 % 3 dimensions
61          if ii==Sz && jj==3
62              fprintf(F,'%18.16f\n',M(ii,jj)); % Write starting locations.
63          else
64              fprintf(F,'%18.16f\t',M(ii,jj));
65          end
66      end
67  end
68
69  fclose(F);
70
71  %Create the motion
72  Mx = abs(X);
73  My = max(Y);
74  Dy = My - Y;
75
76  velocity = 0.00212; %[m/s]
77  time = 2; %[s]
78  distance = velocity*time;
79  normalize_distance = distance/max(Y);
80  passo = 0.05;
81  interlavos = time/passo;
82  intervalo = normalize_distance/interlavos;
83
84  C = (intervalo:intervalo:normalize_distance)+1;
85  len = length(C);
86
87  Trajx(:,1) = X(:,1);
```

```matlab
88   Trajy(:,1) = Y(:,1);
89   Trajz(:,1) = Z(:,1);
90
91   for i=2:len+1
92       Trajx(:,i) = C(i-1)*X(:,1);
93       Trajy(:,i) = C(i-1)*Y(:,1);
94       Trajz(:,i) = Z(:,1);
95   end
96
97   Trajectories = [];
98
99   hold on
100  for ii = 1:len
101      l(ii) = plot3(Trajx(:,ii),Trajy(:,ii),Trajz(:,ii),'*');
102      axis equal
103      pause(.4)
104  end
105
106  for ii = 2:size(Trajx,2)
107      tmp = reshape([Trajx(:,ii),Trajy(:,ii),Trajz(:,ii)]',1,[]);
108      Trajectories = [Trajectories;tmp];
109  end
110
111  %fname = 'Default_Node.dat';
112
113
114  F = fopen(fname,'a'); % Open file for writing, append.
115  [Sz,Sz2] = size(Trajectories);
116
117  for ii = 1:Sz  % Number of time steps
118      for jj = 1:Sz2 % dimensions
119          if jj==Sz2 && ii~=Sz
120              fprintf(F,'%18.16f\n',Trajectories(ii,jj));  % Write coords
121          else
122              fprintf(F,'%18.16f\t',Trajectories(ii,jj)); %No return on last
123          end
124      end
125
126  end
127
128  fclose(F);
```

Appendix D

UDF - Regression Rate.c

```c
/**********************************************************
 node motion based on simple beam deflection equation
 compiled UDF
 **********************************************************/
#include "udf.h"
DEFINE_GRID_MOTION(fuel,domain,dt,time,dtime)
{
Thread *tf = DT_THREAD(dt);
face_t f;
Node *v;
int n;

begin_f_loop(f,tf)
{
    f_node_loop(f,tf,n)
    {
        v = F_NODE(f,tf,n);
        if (NODE_POS_NEED_UPDATE(v))
            {
                v = F_NODE(f, tf, n);

                NODE_X(v) = NODE_X(v)*1.005;
                NODE_Y(v) = NODE_Y(v)*1.005;
                NODE_Z(v) = NODE_Z(v);
                NODE_POS_UPDATED(v);
            }
    }
end_f_loop(f,tf);
}
}
```

Appendix E

Boundary Conditions

Table E.1: HRE model boundary names/type

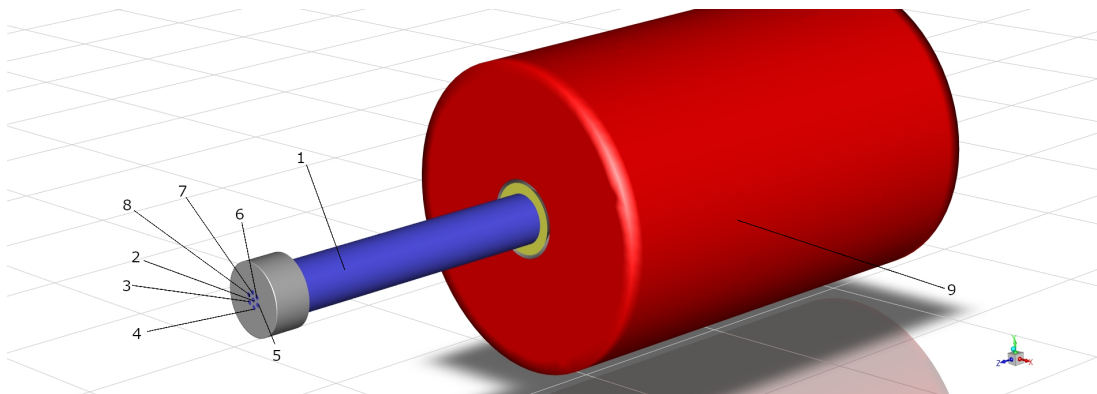| Boundary Condition Name	Correspondent figure	Boundary Type
fuel	1	mass-flow-inlet
injector_1	2	mass-flow-inlet
injector_2	3	mass-flow-inlet
injector_3	4	mass-flow-inlet
injector_4	5	mass-flow-inlet
injector_5	6	mass-flow-inlet
injector_6	7	mass-flow-inlet
injector_7	8	mass-flow-inlet
outlet	9	pressure-outlet

Figure E.1: Boundary Conditions. Each colour corresponds to a boundary type. Inlets - blue; Walls - grey; Outlets - red; and Interfaces - yellow.

Appendix F

Measurement of regression rate in hybrid rocket using combustion chamber pressure

$$\Gamma_c(\gamma_p) = \sqrt{\gamma_p} \left[\frac{2}{\gamma_p + 1} \right]^{(\gamma_p+1)/2(\gamma_p-1)} \quad \text{(F.1)}$$

$$C^* = \frac{1}{\Gamma_c(\gamma_p)} \sqrt{\frac{R_u T_c}{M_p}} \quad \text{(F.2)}$$

$$\dot{m}_f = \frac{P_c A_t}{C^*} - \dot{m}_{ox} \quad \text{(F.3)}$$

$$\dot{r} = \frac{\dot{m}_f}{\pi \rho_f d_p L_g} \quad \text{(F.4)}$$

$$d_{p(i+1)} = d_{p(i)} + 2\dot{r}\Delta t \quad \text{(F.5)}$$